Electronic properties of graphene and other carbon-based hybrid materials for flexible electronics

DISSERTATION

zur Erlangung des akademischen Grades doctor rerum naturalium
(Dr. rer. nat.) im Fach Physik

Mathematisch-Naturwissenschaftliche Fakultät
der Humboldt-Universität zu Berlin

von

Dipl. Phys. Vitalij Scenev

Dekan der Fakultät: Prof. Dr. Elmar Kulke

Präsident der Universität: Prof. Dr. Jan-Hendrik Olbertz

Gutachter/in: 1. Prof. Dr. Jürgen P. Rabe

2. PD Dr. Andrey Turchanin

3. Prof. Dr. Stefan Kowarik

Datum der Promotion: 17.11.2014

Dedicated to my entire family

Abstract

Carbon-based materials such as graphite, graphene and carbon nanotubes are promising materials for printable flexible electronics. Therefore, there is a need for an in-depth scientific understanding of the electronic properties of carbon-based materials as well as for prototypical technologically relevant electronic devices.

This work focusses on the electronic properties of graphene on the one hand, and on the application of graphenes and other carbon-based hybrid materials for transparent electrodes on the other hand. Accordingly, the first part of the work, which is the larger one, is of fundamental nature and focusses on the electronic interaction between graphene and mica as a substrate. The second, smaller part deals with the design of novel conductive inks based on graphene and other carbon-based hybrid materials for applications in printed electronics, in particular for the production of transparent electrodes.

Graphene on mica is a very well defined system, which provides atomically flat graphene extending over several square micrometers. Layer-dependent surface potential variations of single and few layered graphenes on mica were probed with Kelvin Probe Force Microscopy. This allowed to estimate the screening length of graphene on mica. Local variations of the surface electrostatic potential above single layer graphene, originating from confined fluid interfacial monolayers of water between the mica and the graphene, were monitored with Scanning Force Microscopy, Electrostatic Scanning Force Microscopy and Raman spectroscopy. This allowed to quantify the doping of graphene by the confined water layers. Exfoliation of graphene onto adsorbed nanostructures on mica allowed to control the strain of graphene at the nano-scale. Nanostructuring was achieved by first coating mica with submonolayers of dendronized polymers of different generations and subsequently depositing graphene. This approach provides new opportunities for the control of the electronic properties of graphene by strain.

Finally, novel conducting carbon-based inks were designed and transparent electrodes were fabricated therefrom. The formulations of the inks were optimized for printing on plastic substrates.

Zusammenfassung

Kohlenstoff-basierte Materialien wie Graphit, Graphen und Kohlenstoffnanoröhren haben ein hohes Potenzial für eine zukünftige druckbare flexible Elektronik. Daher gibt es sowohl Bedarf an tiefgründigem Verständnis der elektronischen Eigenschaften dieser Materialien als auch an prototypischen, technologisch relevanten elektronischen Bauelementen.

In dieser Arbeit wurden einerseits die elektronischen Eigenschaften von Graphenen und andererseits die Verwendung von Graphenen und Kohlenstoff-basierten Hybridmaterialien als transparente Elektroden untersucht. Entsprechend ist der erste, umfangreichere Teil der Arbeit Grundlagen-orientiert und fokussiert auf die elektrostatische Wechselwirkung zwischen Graphen und dem Substrat Glimmer. Der zweite, kleinere Teil befasst sich mit der Entwicklung leitfähiger Tinten auf der Basis von Graphenen und anderen Kohlenstoff-basierten Hybridmaterialien für Anwendungen in der druckbaren Elektronik, insbesondere für die Herstellung transparenter Elektroden.

Graphen auf Glimmer ist ein sehr wohldefiniertes System, in dem das Graphen über mehrere Quadratmikrometer atomar flach ist. Schichtdickenabhängige Variationen des Oberflächenpotentials von einzel- und mehrlagigen Graphenen auf Glimmer wurden mittels Kelvin Probe Rasterkraftmikroskopie untersucht. Damit konnte die elektrostatische Abschirmlänge von Graphen auf Glimmer bestimmt werden. Lokale Variationen des Oberflächenpotentials innerhalb einer Graphenlage, verursacht durch eingeschlossene Wasserschichten zwischen Graphen und Glimmer, wurden mit Rasterkraftmikroskopie, elektrostatischer Rasterkraftmikroskopie und der Raman-Spektroskopie untersucht. Dies ermöglichte es, die Dotierung von Graphen durch eingeschlossene Wasserschichten zu quantifizieren. Außerdem wurde gezeigt, dass Graphen auf molekular modifiziertem Glimmer lokal auf der Nano-Skala dehnbar ist. Dabei wurde der Glimmer durch das Aufbringen von dendronisierten Polymeren verschiedener Generationen auf Nanometer-Skala modifiziert. Dies eröffnet neue Möglichkeiten, die lokalen elektronischen Eigenschaften von Graphen durch Dehnung zu kontrollieren.

Schließlich wurden Kohlenstoff-basierte leitfähige Tinten hergestellt, daraus transparente Elektroden hergestellt, und die Formulierungen der Tinten für das Drucken auf Plastiksubstrate optimiert.

Contents

Abbreviations

CBM - Carbon-Based Materials

CNT - Carbon Nanotube

CT- Charge Transfer

DEG - Di-Ethylene Glycol

EFM - Electrostatic Force Microscopy

EG - Ethylene Glycol

EMI - Electromagnetic Interference

FWHM - Full Width at Half Maximum

FLG – Few Layer Graphene

GO – Graphene Oxide

HOMO - Highest Occupied Molecular Orbital

IC – Integrated Circuit

ITO - Indium Tin Oxide

KPFM - Kelvin Probe Force Microscopy

LUMO - Lowest Unoccupied Molecular Orbital

MWCNT - Multi Walled Carbon Nanotube

NaDDBs - Sodium dodecylbenzenesulfonate

NMP - N-Methyl-Pyrrolidone

OLED - Organic Light-Emitting Diode

PC – Polycarbonate

PEDOT:PSS - Poly(3,4-ethylenedioxythiophene) poly(styrenesulfonate)

PE - Polyethylene

PET- Polyethylene Terephthalate

PETG - Polyethylene Terephthalate Glycol-modified

QD - Quantum Dot

QLED - Quantum Dot Light-Emitting Diode

SDS - Sodium Dodecyl Sulfate

SFM - Scanning Force Microscopy

SLG – Single Layer Graphene

SP - Surface Potential

STM – Scanning Tunneling Microscopy

SWCNT - Single Walled Carbon Nanotube

TCF – Transparent Conductive Films

RH - Relative Humidity

VdW - Van der Waals

1. Introduction

1.1 Graphene/Substrate System

Graphene is monoatomically thick network of sp^2-hybridized carbon atoms, which are arranged in a honeycomb structure (Fig. 2.1). Its unique electronic properties make graphene a promising candidate to replace conventional silicon electronics or to serve as a complement to the latter. Due to its 2D electronic structure the electronic properties of graphene are sensitive to the presence of adsorbates and of the underlying substrate. Therefore, in order to incorporate graphene into electronic devices, there is a need for an optimal dielectric substrate that provides a substrate-supported geometry while retaining the quality achieved with a suspended sample [1]. Particularly, the performance and reliability of a graphene field effect transistor (FET) can be dominated by the graphene/substrate environment [2].

Charge carrier mobilities in graphene are, in turn, strongly dependent on the doping level of the graphene [3-5], wherein the doping of graphenes by molecular adsorbates, i.e. chemical doping, is considered as a promising route to control electron transport in graphenes. It has been demonstrated that molecules confined between graphene and the underlying substrate can be used to control doping of graphene [6]. Thus, a control of doping, in particular of unintentional doping [7], of graphene needs to be achieved with a reliable method that has to be identified.

Noteworthy, a morphological corrugation can strongly influence the transport properties of the supported graphene [8]. It was found that substrate induced corrugations can modify the electric conductivity of graphene [9].

The interfacial interaction between graphene and its substrate, which varies from strong chemical bonds for epitaxial graphene on a single-crystal substrate [10-14] to weak van der Waals forces for mechanically exfoliated graphene on an amorphous substrate (e.g., SiO_2) [15-17], plays a critical role in determining the morphology of supported graphene [8], which correlates with the electronic

properties of graphene. To achieve control of graphene topography at the nano-scale is therefore crucial for fabricating graphene-based electronic devices.

In the first part of this work the impact of bare and nanostructured mica substrates on electronic properties of graphene is investigated using Scanning Force Techniques and Raman Spectroscopy. In chapter 5.1 the surface potential variations of single and few layer graphenes (FLG) on mica are reported as probed with Kelvin Probe Force Microscopy (KPFM). This allowed to quantify the screening of graphene on mica. In chapter 5.2 Scanning Force Microscopy (SFM), Electrostatic Force Microscopy (EFM) and Raman Spectroscopy were used to investigate both the structure and the electronic properties of graphene conforming to molecular water layers on the mica surface. In chapter 5.3 dendronized polymers of different generations were deposited onto an atomically flat mica substrate and then covered with graphene. Subsequently the topography of the graphene covering the dendronized polymers on mica were imaged with the SFM.

1.2 Graphene and other carbon-based hybrid materials for flexible electronics

An emerging field of electronics is “printable flexible electronics”, which offers a completely new field of electronic applications, based on mass production, which is due to the possibility to print all the components of the electronic device by cheap printing methods, used nowadays in the printing industry. Flexible electronics requires flexible, highly conducting (with respect to the area of their application) electrodes, which cannot be realized by ITO, due to its mechanical fragility [18]. Moreover, the price for ITO grows and dominates in some cases the price of an electronic device. Therefore, industry experiences growing needs for cheap transparent and highly electrically conductive electrodes. Carbon based materials (CBM), such as graphenes, carbon nanotubes (CNT) and conducting polymers, in particular PEDOT:PSS, are considered to be promising candidates to replace ITO. Processing of CBMs into transparent and conducting electrodes, however, is difficult for a few reasons, which will be described below.

It is difficult to process films from CNTs. For example pure CNTs cannot be dissolved well in common solvents. In order to improve the solubility of CNTs in water one has to add amphiphilic molecules to the solvent [19]. However, amphiphilic molecules coat CNTs, thereby increasing their solubility on the one hand, but on the other hand the amphiphile coating prevents the formation of CNT percolation networks and therefore hampers the electrical conductivity of CNT films, reducing it by several orders of magnitude [20, 21]. Sonication of graphite flakes in some common organic solvents exfoliates the flakes and results in low concentration solutions of graphenes [22]. Films prepared from such solutions exhibit poor electrical conductivity [23] due to the relatively small size of graphenes in solution, which do not create a percolation network upon drying. If properly dispersed, CNTs can be easily deposited onto transparent plastic films to form a transparent conductive coating from a solution, using diverse printing techniques such as slot-die-coating [24], screen- and ink-jet-printing [25, 26], or roll-to-roll [27] transfer.

Therefore, the aim of the second part of the work is to provide novel ink formulations based on mixtures of CBMs. On the one hand the inks should provide an optimal percolation network to achieve the highest conductivity and on the other hand they are optimized for printing and can therefore be applied for printing of transparent electrodes on diverse substrates. The focus here is laid on homogenous ink dispersions and homogeneous film formation of printed films, accompanied with superior optical and electrical characteristics of the films. The results of this part of the work are presented in chapter 5.4.

2. Scientific background

The scientific background required for understanding of the results obtained in this work is presented in this section. Chapter 2.1 is dedicated to the first part of the thesis and is related to Chapters 5.1-5.3. Chapter 2.2 consequently contains the scientific background, which is essential for understanding the results presented in Chapter 5.4.

2.1 Graphene

This chapter is dedicated to the physical background of graphene. Informations about structural and optical properties, electronic structure and doping of graphene are provided. The mechanical exfoliation of graphene on mica accompanied with the optical detection of graphene is described.

2.1.1 Structure

Structurally, graphene is a one-atom-thick planar sheet of sp^2-bonded carbon atoms that are arranged in a honeycomb crystal lattice [28] as illustrated in figure 2.1. Each carbon atom in graphene is connected to its three nearest neighbours by strong planar σ bonds that involve three of its valence electrons occupying the sp^2-hybridized orbitals [29].

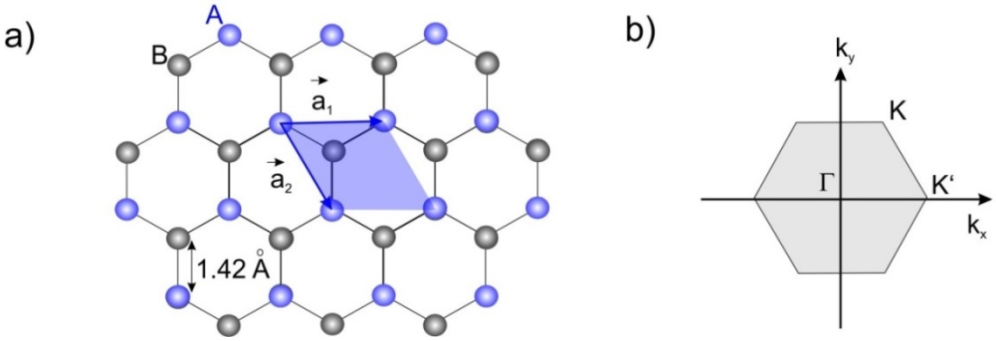

Fig. 2.1: Structure of graphene. Hexagonal lattice consisting of two atoms (A and B) per unit cell (a) which is spanned by two primitive translation vectors $\vec{a}_1$ and $\vec{a}_2$. Brillouin zone of graphene (b). K, K' and Γ are important symmetry points of the Brillouin zone of graphene.

These bonds are responsible for the planar structure of graphene and for its mechanical and thermal properties [29]. The fourth valence electron is located in the half-filled $2p_z$ orbital orthogonal to the graphene plane and forms a weak π bond by overlapping with other $2p_z$ orbitals [29]. These delocalized π-electrons are crucial for the electronic properties of graphene.

2.1.2 Electronic structure

The electronic structure of graphene computed within the tight-binding approximation, can be described with the following relation [30, 31]:

$$E = \pm\gamma\sqrt{1 + 4\cos^2\frac{ak_x}{2} + 4\cos\frac{ak_x}{2}\cos\frac{\sqrt{3}ak_y}{2}} \qquad (2.1)$$

The electronic dispersion of the π-bands in the graphene Brillouin zone is vizualized in figure 2.2. The electronic structure of graphene exhibits energy bands with linear dispersion crossing at K and K' points (Fig. 2.2b) and can be described as a linear dispersion with the equation $E(\boldsymbol{k}) = \hbar \boldsymbol{V_F k}$ [32].

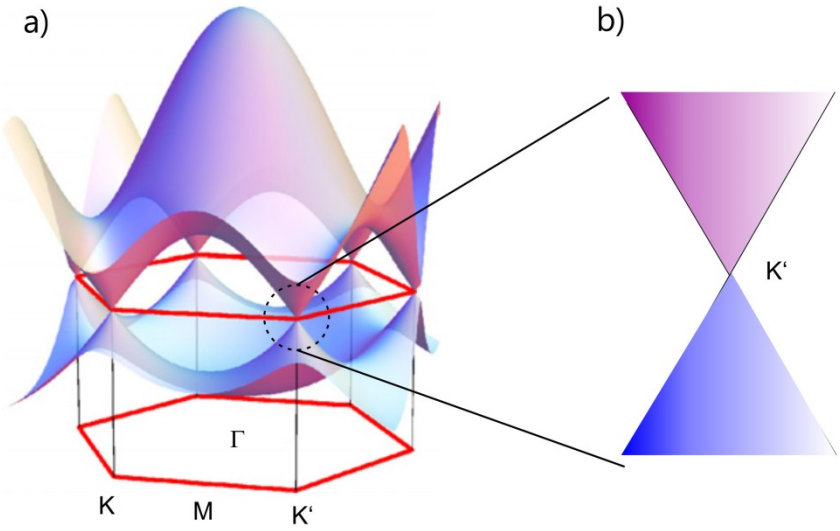

Fig. 2.2: (a) The electronic dispersion of the π-bands in the graphene Brillouin zone (Reprinted from [33]) (b).

This expression relates the electron wave vector **k** with the energy by a Fermi velocity v_F , which is found to be close to 10^6 m/s [34, 35]. The Fermi levels are located at the point of band crossing, which is called the Dirac point [36]. Due to the absence of the band gap at K and K'- points the graphene behaves as a zero-gap semiconductor, where the mass of carriers is regarded as zero (Dirac fermion) [37].

2.1.3 Optical properties

The optical properties of graphene are a direct consequence of its 2D structure and gapless electronic spectrum [29]. For photon energies in the range of 0.5-1.2 eV [38] the optical conductivity in the linear dispersion regime of graphene [33] is a universal constant, which is independent of frequency: $\sigma(\omega) = e^2/4\hbar$ (Fig. 2.3), where *e* is the electron charge and ħ the reduced Plank constant [29, 38, 39].

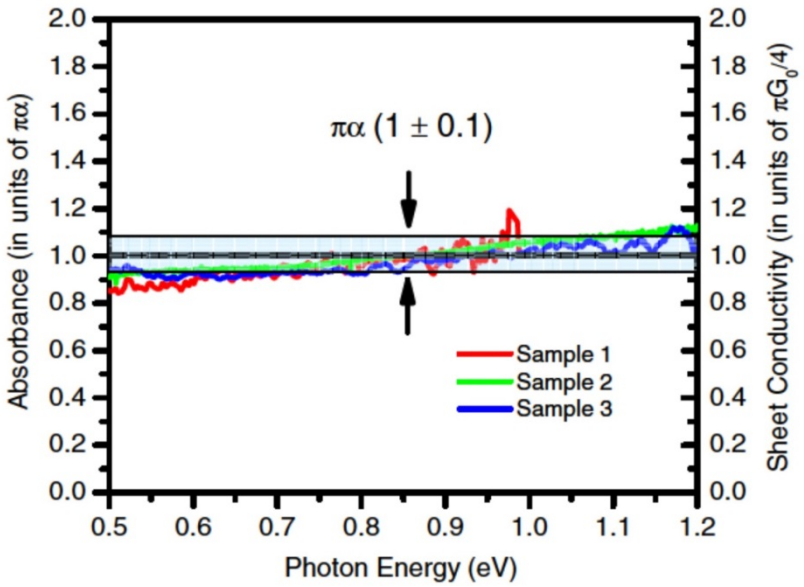

Fig. 2.3: Absorption spectra for three different graphene samples on SiO_2 (Reprinted from [40], Copyright (2014) by the American Physical Society). The black curve corresponds to the universal absorbance.

Consequently absorbance P ($\propto \sigma(\omega)$), transmittance T and reflectance R -are also universal constants, which are determined only by fundamental constants. Especially, the ratio of absorbed to incident light intensity for monolayer graphene is proportional to the fine structure constant $\alpha = e^2/\hbar c = 1/137$, $P = (1 - T) \approx \pi\alpha =$

2.3% [29], where *c* is the velocity of light. For a few layers of graphene stacked on top of each other the absorbance increases gradually for the first few layers [41].

2.1.4 Mechanical exfoliation of graphene on a substrate

Mechanical exfoliation provides graphenes of high quality. However they are usually small in size, typically 5-5000µm^2. This method allows to produce graphenes without defects and without of any annealing methods. Usually graphenes are exfoliated using a scotch tape but it has been demonstrated that this method contaminates graphenes [42]. A layer of contamination confined between graphene and the substrate is typically introduced if scotch tape is used. Therefore, the exfoliation method has been modified as described below.

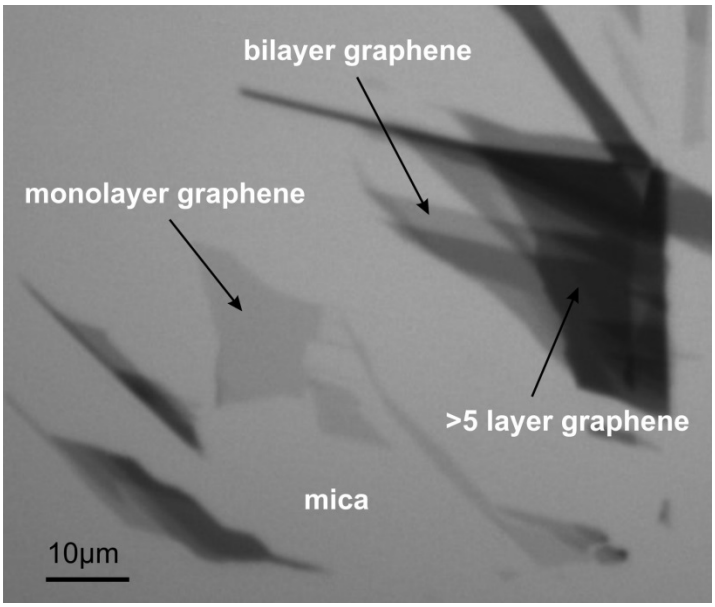

Fig. 2.4: Optical detection of graphenes on mica

Graphenes were mechanically exfoliated onto a freshly cleaved muscovite mica surface (Ratan mica Exports, V1 (optical quality)) in a glove box (LABmaster, M. Braun Inertgas-Systeme GmbH) with less than 5 ppm of each H_2O and O_2. For that, a thin graphite flake was peeled off freshly cleaved highly oriented pyrolytic graphite (HOPG, grade ZYB, Advanced Ceramics) and gently pressed onto and subsequently removed from the mica surface. This sample preparation has been demonstrated to

result in a substantially reduced amount of surface contamination [42]. The samples prepared in the glove box were then transferred to ambient with ambient relative humidities (RH) being below 30%. Single and double layer graphenes were localized optically , thicker graphenes were identified with scanning force microscopy (SFM) [41] and verified with Raman Spectroscopy. A typical optical image of graphenes on mica is presented in figure 2.4.

2.1.5 Doping of graphene

In semiconductor doping can be usually realized by incorporating foreign atoms into the bulk which introduce extra holes or electrons in the semiconducting material [43]. It is also possible to achieve doping through charge exchange with dopants situated at the surface [43, 44]. This kind of doping is labelled as “Surface Transfer Doping” [45, 46] and can be realized in graphene.

The scenario of doping in graphene is depicted in figure 2.5. For undoped or charge neutral graphene the Fermi-level is located at the Dirac-point. If extra electrons are transferred to graphene the Fermi-level shifts towards the conduction band (Fig. 2.5c). Consequently, if electrons are transferred from graphene the Fermi-level shifts towards the valence band (Fig. 2.5b).

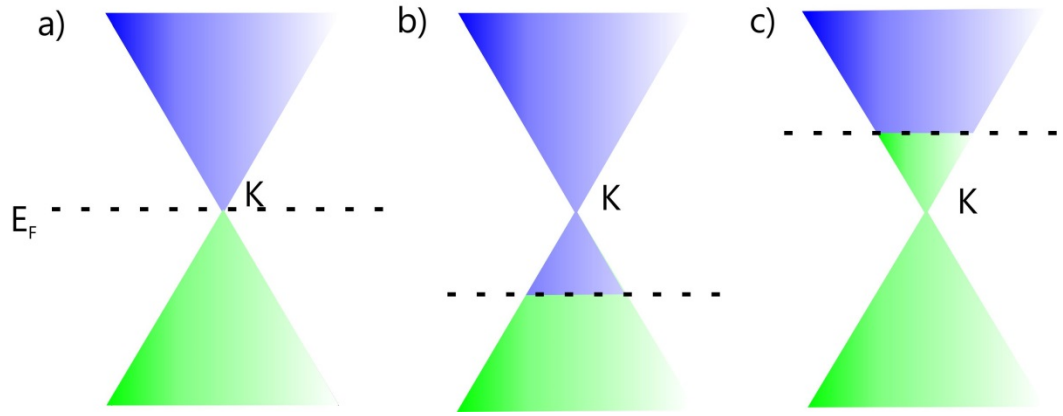

Fig. 2.5: Illustration of doping of graphene. The electronic structure of graphene with the linear energy dispersion at the K-point. Green cone below the Fermi-level (E_F) corresponds to the valence band and blue cone above the Fermi-level corresponds to the conduction band. For undoped graphene (a) the Fermi-level E_F, whose position is indicated with the dashed line, coincides with the Dirac-point K. The Fermi-level is shifted away from the Dirac-point for p- (b) and n-doping (c).

Interestingly, the doping of graphene can be probed with Raman-spectroscopy [6, 47-51] due to strong electron-phonon coupling in graphene [50]. If the Fermi energy of graphene is changed, there is a reduction in the interaction between phonons and interband electron-hole pairs, thus changing the effective force constant of the lattice vibrations [35]. Within the framework of time-dependent perturbation theory it is possible to evaluate the relationship between the Fermi-level shift and the shift of the G- and 2D-Raman modes [47]. The following equation relates the Fermi-level shift with the shift of the G-Raman mode [47]:

$$\hbar\omega_G - \hbar\omega_{G_0} = \lambda\left\{|E_F| + \frac{\hbar\omega_G}{4} ln\left|\frac{2E_F - \hbar\omega_G}{2E_F + \hbar\omega_G}\right|\right\} \tag{2.1}$$

where ω_{G_0} is the position of the G-mode ω_G at the Dirac-point, $\lambda = \frac{A_{uc}D^2}{2\pi\omega_G M V_F^2}$. A_{uc} is the area of the graphene unit cell, M is the carbon atom mass, D is the electron-phonon coupling strength and V_F is the Fermi velocity [47].

The most elegant derivation of the relation of the Fermi-level shift on the phonon dispersion of graphene is presented by Popov *et al.* [52].

2.2 Functional inks

Functional inks are essential parts of industry and they are of fundamental interest. Functional inks, as the name implies, contain functional materials (pigments) which provide desired functional property to the ink. In this work conductive pigments are investigated. Ink formulations were developed, made on the basis of conductive pigments, which were optimized for printing applications. Additionally, the films fabricated from these inks were characterized. The aim is a homogeneous film formation of dry films. The key challenge is thereby to prepare a conductive film from the ink without disturbing the intrinsic conductivity of the pigments.

This chapter provides an overview of the relevant physical background, which is necessary for understanding the results reported in Chapter 5. 4.

2.2.1 Surface tension

Surface (interfacial) tension γ is the energy required to create a unit surface of area A, which is defined as $\gamma = (\partial G/\partial A)_{T,P,n}$ [38] and has a dimension $\frac{N}{m}$. G is the Gibbs free energy of the total system, A the interfacial area, T the temperature, P the pressure, and n the total number of moles in the system. In terms of wetting of the substrate and film formation the surface tension of functional inks plays a crucial role and is an important parameter for the formulation of functional inks.

For liquids a surface tension or surface energy is determined from the forces between molecules and surfaces [53]. Wetting, surface tension and the contact angle are strongly connected with each other as it will be discussed in the following. As a drop of a liquid comes in contact with the flat surface of a solid substrate, a contact angle θ between the drop and the substrate is formed (Fig. 2.6). Moreover three phases, which are considered to be in equilibrium, are formed: solid-liquid (SL), liquid-

gas (LG) and solid-gas (SG) phase. These three phases can be quantified in terms of surface tensions [53]: γ_{LG}, γ_{SG}, γ_{SL}, which are related by the Young's equation: $0 = \gamma_{SG} - \gamma_{SL} - \gamma_{LG} \cdot \cos\theta$ [38].

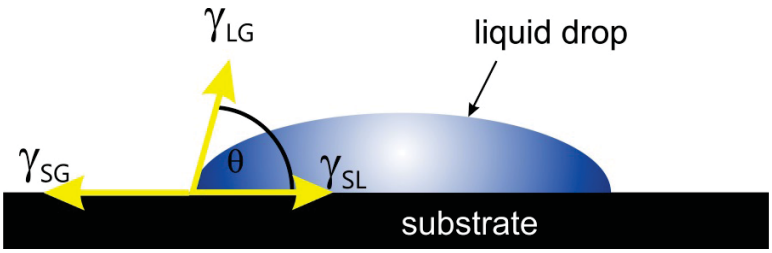

Fig. 2.6: Schematic representation of a liquid drop on flat substrate surface.

Based upon Young's equation one can classify the wetting of the surface by a liquid knowing the surface tension of the liquid and the substrate; thereby one can quantify what is good and bad wetting. In general, the liquid wets the substrate in if $0 < \theta \leq 90°$. If the liquid is water the surface which offers a contact angle smaller than 90° is called hydrophilic, if $\theta > 90°$ it is hydrophobic and if $\theta > 150°$ the surface is called superhydrophobic [54]. The contact angle of water can often be changed by chemically modifying surfaces by addition of certain solute molecules into the medium that adsorb onto the surfaces [53]. For instance surfactants like NaDDBs [55] or SDS [56] reduce the contact angle of aqueous CNT dispersion on glass largely leading to improved wetting of the substrate by the dispersion. Also the addition of alcohols to water reduces the surface tension of water [57]. Within the framework of this dissertation aqueous dispersions will be investigated.

2.2.2 Inter-particle forces

The interaction between the particles in a dispersion is an essential aspect for understanding the rheological properties of functional inks.

Tadros [58] describes four types of inter particle forces: hard sphere, soft (electrostatic), van der Waals, and steric. Hard-sphere interactions, which are repulsive, become significant only when particles approach each other at distances slightly less than twice the hard-sphere radius [59]. Colloidal interactions are described by the inter-particle potential [53, 60]. For non-charged, spherical particles of radii a, it is common to assume that the van der Waals interactions are non-retarded [53] and additive [60]. The resulting van der Waals potential between the particles, $V(r)$, where r is the inter-particle distance, is given by

$V(r) = -\frac{12 \cdot A_{eff} \cdot a}{r}$ for $r \ll a$ and $V(r) \propto \frac{A_{eff} \cdot a}{r^6}$ for $r \gg a$ [60, 61].

For all separations, r, the inter-particle potential is proportional to the particle size, a. The other proportionality constant is A_{eff}, the effective Hamaker constant which depends on the nature of the particles and the intervening liquid [53, 60, 62, 63].

2.2.3 Polymeric stabilization

Polymers can be used as stabilizers of colloidal particles in dispersions [64] against flocculation [65], i.e. with steric stabilization for uncharged or an electrostatic stabilization mechanism for charged polymers. Steric stabilization occurs due to the presence of physical barriers adsorbed on particles that prevent the particles from coming close enough to allow the van der Waals attractive forces between particles to dominate [63, 65, 66].

Polymers can be effective stabilizing agents only if the polymer – solvent interactions are more favourable than the polymer – polymer interactions [59]. These interactions determine the conformation of the polymer once it is adsorbed on a surface, and hence determine the minimum separation distance which can be achieved through the adsorbed layers [63]. The key to steric stabilization is to increase the closest distance of approach between particles in order to minimize van der Waals attractive forces [60, 62, 66].

When two particles with adsorbed polymers approach, the polymer molecules are crowded, the result being that the polymer configurational entropy is reduced [61]. This results in a repulsive force that keeps the particles apart [61]. The extent of the interaction is controlled by the radius of gyration [67, 68] and the state of the polymer in the solvent [61]. For stable suspension the radius of gyration must be larger than the extent of van der Waals forces [61, 69].

3. Materials

This section provides an overview of the materials used within this work besides graphene, which is separately presented in Chapter 2.1. Mica has been used as a dielectric substrate, on which graphenes were mechanically exfoliated. The results, where mica was used, are presented in Chapters 5.1 – 5.4.

Other Materials such as PEDOT:PSS, CNT's and GO have been used to prepare conducting inks for electrodes. These results are presented in Chapter 5. 5. Note, that the dendronized polymers are explicitly described in Chapter 5.3.

3.1 Mica

Micas belong to the group of phyllosilicate minerals exhibiting a two-dimensional sheet structure [70]. There are several kinds of mica minearals. In this work muscovite mica is used. Muscovite is a 2 : 1 layered dioctahedral aluminosilicate with the formula $KAl_2(Si_3,Al)O_{10}(OH)_2$ [71]. Structurally, each irreducible muscovite layer consists of one layer of octahedrally coordinated Al_3^+ ions, which is sandwiched between two tetrahedral silicate layers with vertices pointing toward the octahedral layer [70]. Within tetrahedral units aluminum is randomly substituted for silicon with a ratio of 1 : 3 to compensate the negative charge of adjacent mica layers, and potassium counterions are present in 12-fold oxygen coordination [70, 71].

After the cleavage, half of the potassium ions are assumed to be left to preserve electroneutrality of the surface as a whole [70, 71]. However, the positions of the ions

and their distribution over the surface are not well defined from the experimental point of view [6, 70]. Since the interaction between potassium and the surface is of ionic nature, the binding is strong enough to prevent diffusion of potassium ions across the surface at room temperatures [71].

Graphene on mica exhibits an atomically flat structure [72] without any detectable defects at the nanometer scale [73].

Muscovite mica is birefringent and, in the visible range, transparent, where the transparency scales with the thickness of the mica substrate. The latter can be adjusted by simple mechanical cleavage of mica using either blade or scotch tape. It has been elegantly demonstrated by Dorn *et al*. [41], that the optical contrast of graphenes on mica can be enhanced if using special optical set-up[1] for the graphene detection.

3.2 Carbon Nanotubes - CNT

Carbon nanotubes (CNT) are allotropes of carbon having a cylindrical shape [74]. They are categorized into Single-Walled (SW) and Multi-Walled (MW) – CNTs, where the SWCNT's can be structurally described as graphene rolled up into a cylinder with a diameter in the range of 1-2 nm. The length of a SWCNT is typically 10-50µm but can be as large as several mm [75]. Similarly, multi-walled carbon nanotubes consist of coaxially arranged, nested cylinders of graphene [75] (or carbon shells), with an adjacent shell separation of 0.36 nm [74, 76] and with diameters of several tens of nanometers (Fig. 3.1).

[1] Illuminating from the back, i.e. through the mica, and using crossed polarizers, the component of the light reflected from the last interface between mica and air is filrered out. This is due to the birefringent nature of mica and the fabry-perot-effect arising from the layered structure of mica

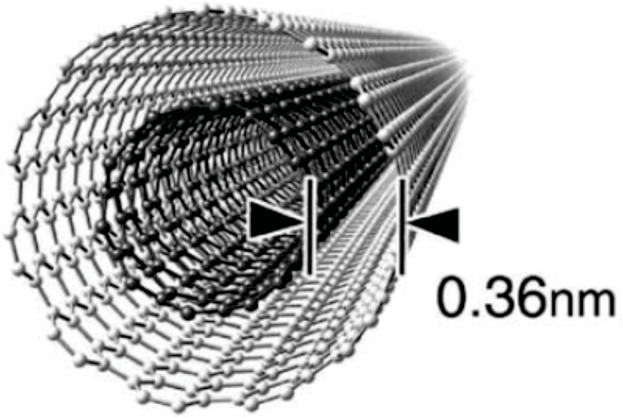

Fig. 3.1: Image of a MWCNT consisting of two walls (Reprinted from [76] Copyright (2014), with permission from Elsevier).

Nowadays, MWNTs and SWNTs are produced mainly by three techniques: arc-discharge, laser-ablation, and catalytic growth [74].

CNT's are considered as promising candidates for transparent electrodes [56] due to their high electrical conductivity combined with high optical transparency.

3.3 Graphene Oxide

Graphene oxide (GO) or graphite oxide [77] can be obtained by chemical oxidation of graphite [78] combined with ultrasonication. Structurally it is a graphene sheet derivatized by carboxylic acid groups at the edges and by phenol hydroxyl and epoxide groups mainly on the basal plane [77, 79-82] (Fig. 3.2). GO is known to disperse, in particular in water due to the –COOH groups on its edges [77].

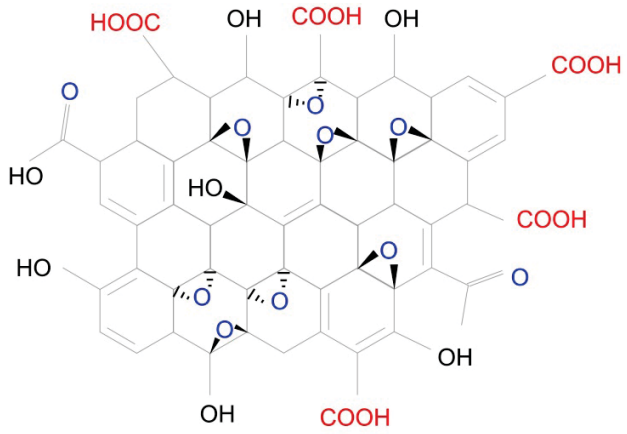

Fig. 3.2: Chemical structure of GO.

Interestingly, the basal plane of GO is hydrophobic, due to a network of hydrophobic polyaromatic islands of unoxidized benzene rings [77, 79, 83]. That implies that GO can be viewed as an amphiphile. Concerning the electronic properties GO is an insulator [84] but through reduction, where a significant fraction of the contained oxygen is removed, the conductivity of GO can be largely improved [84-86]. Within this work it has been shown that GO can be used as film forming agent in conductive ink formulations to improve film formation and eliminate the coffee ring effect as it is demonstrated in chapter 6.5. GO used in this work was prepared with Hummers' method [78].

3.4 PEDOT:PSS

PEDOT:PSS (Fig. 3.3) belongs to the class of intrinsically conducting polymers (ICPs) which are commonly used as electrodes or hole injection layers in organic light-emitting devices. PEDOT:PSS exhibits relatively high work function values of 4.8 to 5.7 eV, depending on the formulation and the preparation parameters [87, 88], which makes it highly suitable as hole-injection layer in devices [89].

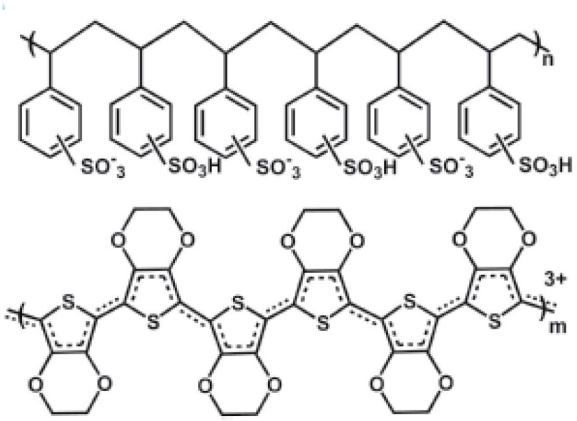

Fig. 3.3: Chemical structure of PEDOT:PSS.

PEDOT:PSS exhibits different electrical conductivities depending on the quality and preparation. Within this work, commercially available dry re-dispersible palettes of PEDOT:PSS (AGFA company) were used. This form of the polymer allows to create own ink formulations containing PEDOT:PSS, which are the subject of chapter 5.5.

4. Experimental methods

This section provides an overview of the experimental techniques which have been employed in this work. In particular, Electrostatic and Kelvin Probe Force Microscopy as well as Raman spectroscopy were used, and the theoretical background will be provide in the following. The experimental setups, which were used for the experiments will be illustrated in the next chapter.

4.1 Scanning Force Microscopy

The basic concept of the scanning force microscope (SFM) is to probe the force between the sample surface and a sharp SFM-tip on a flexible cantilever by measuring the deflection of the cantilever while scanning it line-wise across the surface (Fig. 4.1.a). From this the morphology of the surface is deduced. The bending of the cantilever is measured optically with a laser beam reflected from the cantilever into a position-sensitive photodiode [90, 91]. There are different methods of the SFM operating principle to obtain informations about sample topography.

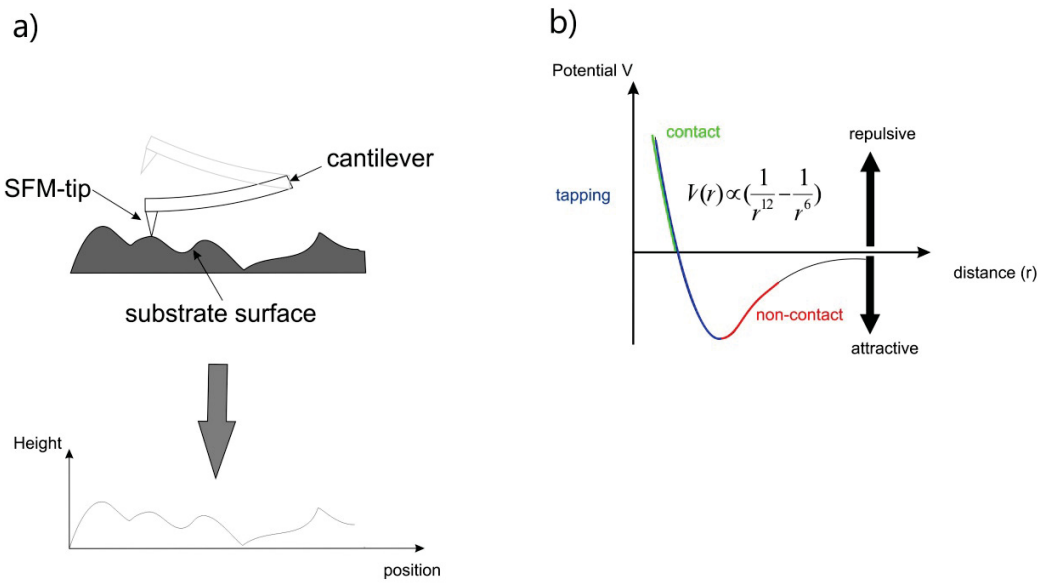

Fig. 4.1: Schematic view of the basic principle of the tapping mode SFM (a), where the cantilever oscillates at its resonance frequency and scans the substrate surface. The Lennard-Jones-Potential with corresponding SFM-regimes (b).

The images presented in this work were acquired using the "tapping mode" [92, 93]. In this mode the change of the free oscillation amplitude of the cantilever due to the "tapping" of the surface with the tip is measured with a feedback-loop. Driven by piezo crystals, the cantilever laterally scans the sample and the sample morphology on the scan path leads to varying tip-sample interactions, which modify the oscillation amplitude of the cantilever away from a given set-point [87]. This variation is used to vertically adjust the tip-sample distance to regain the set-point value of the amplitude via the feedback system, which finally generates a topographic image of the sample [87]. The interaction between the atom on tip apex and the surface is simplified to be of van der Waals nature (Fig. 4.1b).

4.2 Electrostatic Force Microscopy - EFM

EFM is a scanning force technique to probe electronic properties of surfaces. It is a non-destructive technique, which allows to probe the work function of metallic samples [94, 95] as well as the surface potential of a dipole layer [96, 97]. EFM has been shown to be applicable to graphene [49, 96, 98] and to probe graphene-substrate electronic interactions [49, 94, 97].

The EFM-Method is a dual-pass technique, where the EFM-Phase signal detection is usually acquired in a two-pass (lift) mode (Fig. 4.2). In the first pass (Fig. 4.2a), the SFM tip traces the sample topography in tapping mode. In the second (interleave) pass (Fig. 4.2b) along the same scan line, the tip is biased with a DC voltage V_T and retraces the topography acquired in the first pass, at a fixed lift height of 30 nm above the surface.

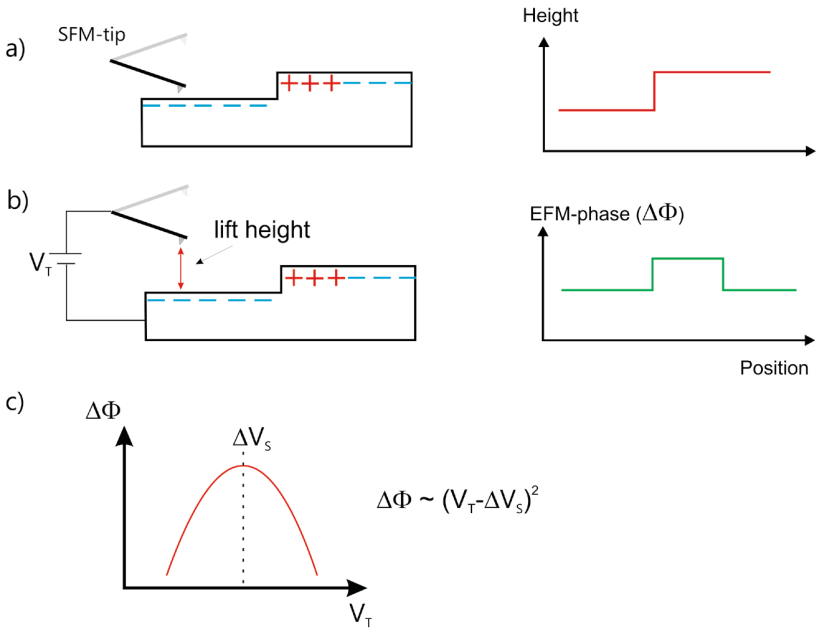

Fig. 4.2: Schematic representation of EFM. The first pass is recorded in tapping mode (a) and the second pass in lift mode (b), where the tip traces the topography acquired in the first pass and while a DC bias V_T is applied between the tip and sample. The phase shift between the driving force and bias modulated oscillation of the cantilever due to the electrostatic force is measured (green curve in (b) right image).

The cantilever is mechanically driven at its resonance frequency, and the phase shift of the cantilever oscillation is imaged as a function of tip position. The phase shift $\Delta\Phi$ due to tip-sample capacitive coupling is expressed as [99, 100]:

$$\Delta\Phi = \sim(V_T - \Delta V_s(x,y))^2 \quad (4.1)$$

where V_T is the bias applied between the back electrode and the tip and $V_s(x,y)$ is the local electrostatic potential. This method gives information about the surface potential differences on the sample surface. The EFM measurements in this work were performed with a scanning force microscope (Digital Instruments – Nanoscope IV) using conductive, Pt-coated SiN cantilevers. The cantilevers had a typical resonance frequency of 70 kHz and a spring constant of 2 N/m with a typical tip apex radius of 20 nm, as specified by the manufacturer (Olympus Corporation).

4.3 Kelvin Probe Force Microscopy - KPFM

Similar as EFM, the KPFM is also a scanning force technique to study electronic properties of samples, in particular the surface potential. KPFM has been applied for the investigation of the work function of graphene [94, 95]. The detailed description of the method is reflected in the text below.

The KPFM measurements were performed with the Scanning force microscope (Digital Instruments – Nanoscope IV) using conductive, Pt-coated SiN cantilevers. The cantilevers had typical resonance frequency of 70 kHz and spring constant of 2 N/m with a typical tip apex radius of 20 nm, as specified by the manufacturer (Olympus Corporation). The surface potential (SP) signal detection was acquired in a two-pass (lift) mode. In the first pass, the AFM tip traces the sample topography in tapping mode. In the second (interleave) pass along the same scan line, the tip is biased simultaneously with a DC- (V_{DC}) and an oscillating AC-voltage (V_{AC}) at the cantilever resonance frequency (ω_{AC}) and retraces the topography acquired in the first pass, at a fixed lift heights of 30 nm above the surface. Considering the system tip-sample as a

parallel plate capacitor (Fig. 4.3), the force acting between the plates of a capacitor separated by a distance z can be expressed as the first derivative of the energy E within the capacitor:

$$F = -\frac{\partial E(z)}{\partial z} = -\frac{1}{2}\frac{\partial C(z)}{\partial z}V^2 \tag{4.2}$$

where C is the capacitance and V is the voltage. The voltage between tip and sample has three components, namely the work function difference including the surface potential of a dipole layer on top of a sample ΔV_S, the V_{DC} and the oscillating V_{AC}, both applied by a feedback loop of the instrument.

Thus it follows:

$$V = \Delta V_S + V_{DC} + V_{AC} \cdot \sin(\omega_{AC} \cdot t) \tag{4.3}$$

Inserting the expression for V into equation (4.2) one obtains the expression for the force acting between the plates of the capacitor, which has three components:

$$F(z) = F_{DC} + F_{\omega} + F_{2\omega} \tag{4.4}$$

Where the spectral component of the electrostatic force between the sample and the tip at the ω can be expressed as [101]:

$$F_{\omega} = -\left(\frac{dC}{dz}\right) \cdot (\Delta V_S - V_{DC}) \cdot V_{AC} \cdot \sin(\omega_{AC} \cdot t) \tag{4.5}$$

ΔV_S is the surface potential of the sample. By inspection of this equation one can notice that by monitoring the electrostatic force at ω_{AC} with a lock-in amplifier, V_{DC} can be adjusted by a feedback circuit to minimize the force on the cantilever to the null condition ($V_{DC} = \Delta V_S$) [101].

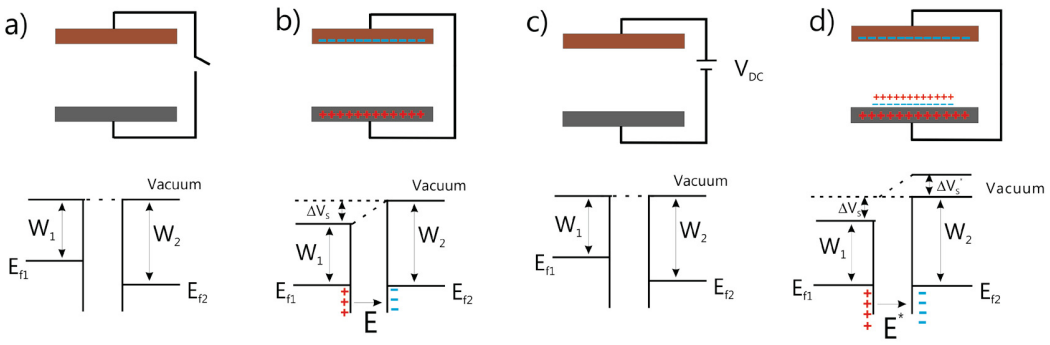

Fig. 4.3: Scheme of a build-in potential difference ΔV_S or contact potential difference due to different work functions (a-c), and due to the addition of a dipole layer ΔV_S* (d). Electrically not wired metals with different work functions (a) and electrically wired metals (b) with common Fermi level and build-in electric field E between the plates arising from the Fermi-level alignment and associated contact potential difference ΔV_S . A voltage V_{DC}= ΔV_S applied between the plates (c) compensates the contact potential difference ΔV_S and therefore the electric field between the plates vanishes. An additional dipole layer on top of a metal plate (d) produces an electrostatic (surface) potential ΔV_S* additional to ΔV_S, and therefore the electric field between the plates associated with the potential of a dipole layer is E*.

The value of the surface potential measured with KPFM is more accurate than measured with EFM; however, the lateral resolution of KPFM is 120±10 nm, whereas the EFM provides a lateral resolution of approximately 60±10 nm (Fig. 4.5). Therefore, the combination of these two methods could provide more accurate quantitative information about the surface potential.

4.3.1 Work function and surface potential

The work function of a solid is the energy, which is required to bring the electron from the chemical potential of the solid into the vacuum. The total work function of a metal depends on the bulk chemical potential and the electrostatic potential across the metal surface [102]. The work function is experimentally known to be different for different faces of a crystal by amounts ranging from one-tenth to half a volt [103]. The origin of the latter is attributed to the Smoluchowski-effect [103].

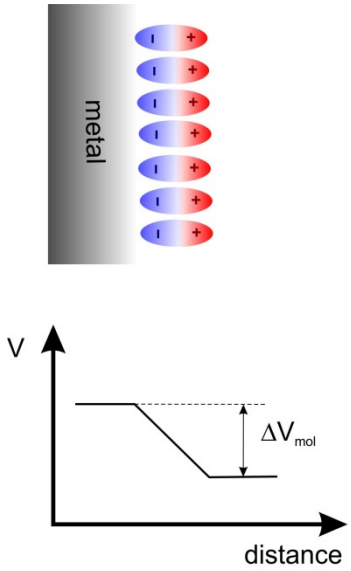

Fig. 4.4: Adsorption of a molecular layer on a metal (top) and a corresponding energy diagram that shows the change of the electrostatic potential V on the metal surface produced by the dipole layer ΔV_{mol} .

Another phenomenon is the adsorption of atomic or molecular species on a metal surface. This will also induce changes of the work function [104] as it will be described in following. In particular upon adsorption of a molecular layer, the work function change can be computed with the Helmholtz equation [101], which relates the surface potential produced by a molecular layer with its dipole moment. This scenario is depicted in figure 4.4.

Using the equation:

$$\Delta W_f = W_{f_0} + \Delta V_{mol} e = W_{f_0} + \frac{\vec{\mu}}{A\varepsilon\varepsilon_0} \tag{4.6}$$

the change of the work function upon the adsorption of the molecular layer can be estimated. W_{f_0} is the work function of a metal before the adsorption of molecular layer, ΔV_{mol} is the electrostatic potential difference produced by a molecular layer and e is the elementary charge.

4.4 Spatial resolution of EFM and KPFM

The spatial resolution of KPFM and EFM was estimated as it is depicted in figure. 4.5.

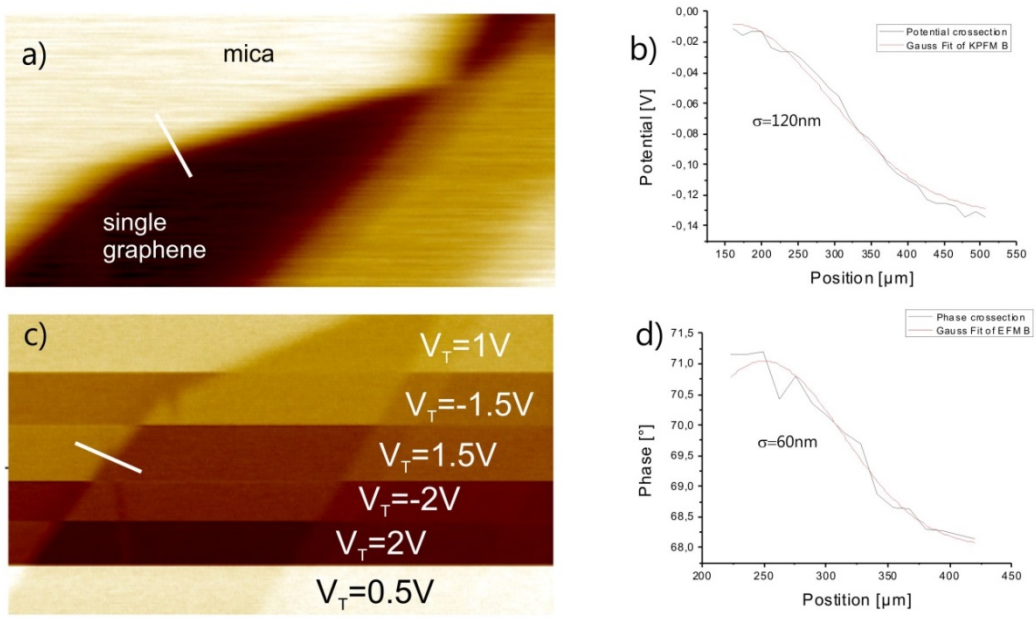

Fig. 4.5: Estimate of the spatial resolution of KPFM and EFM. KPFM-potential (a) and EFM-phase-image for different tip-voltages (c) of single graphene on mica. Potential (b) and EFM-Phase-profile for V_T=1.5V (d) taken along white line in (a) and (c) for KPFM- and EFM-images with corresponding Gaussian fits respectively. The spatial resolution of each method was estimated from the standard deviation σ of the Gaussian fit.

4.5 Raman Spectroscopy

4.5.1 Theory

Raman spectroscopy is a commonly used optical and non-invasive experimental method, for probing phonons. Raman spectroscopy is based on the inelastic scattering of monochromatic light within the studied sample, accompanied by the generation or annihilation of different elementary excitations, in particular phonon vibrations [105].

In general Raman spectroscopy is associated with the polarizability α of the atoms or molecules to be probed. The polarizability is a tensor which acts a proportionality constant between induced dipole moment and the strength of the electric field of the incident light [106]. An electric field induces polarization (dipole moment) in an atom or molecule, which can be described by the following equation.

$$\vec{p} = \alpha\vec{E} \tag{4.7}$$

The Gross selection rule [107] states that the polarizability of a molecule should change during vibration. That implies $\frac{\partial\alpha}{\partial q} \neq 0$, where q is the normal coordinate of the vibration. In case of an oscillating electric field, as it is the case in Raman-experiments, the electric field can be expressed as:

$$E = E_0 \sin(\omega_i t) \tag{4.8}$$

As a consequence the polarizability of the atoms is then modulated by the lattice vibrations with the frequency ω_q [106], which is coupled to the optical field, as follows [106, 107]:

$$\alpha = \alpha_0 + \alpha_1 \sin(\omega_q t) \tag{4.9}$$

Thus the polarization induced by the electric field becomes:

$$\begin{aligned} \vec{p} = E_0\big(\alpha_0 + \alpha_1 \sin\big(\omega_q t\big)\big) \sin(\omega_i t) = \\ = E_0 \left[\alpha_0 \ \sin(\omega_i t) + \frac{1}{2}\alpha_1 \cos\big(\omega_i - \omega_q\big)t - \frac{1}{2}\alpha_1 \cos\big(\omega_i + \omega_q\big)t\right] \end{aligned} \tag{4.10}$$

From this equation one can see that scattered light consists of three components, namely one elastic and two inelastic.

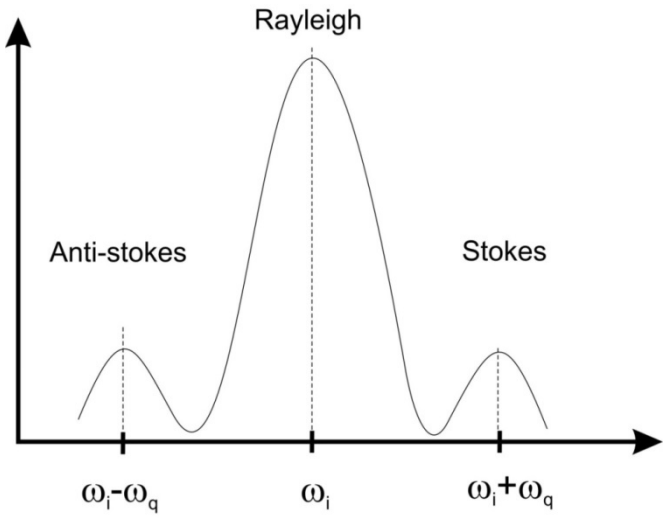

Fig. 4.6: Schematic representation of the spectrum arising from light scattering experiments which contains the Raman- and Rayleigh-peaks. Note, that usually the incident light corresponding to Rayleigh-peak has to be filtered out since its intensity exceeds the intensity of Raman- signal by several orders of magnitude. The peak of incident light, which is elastically scattered (Rayleigh) is localized at the frequency ω_i and the stokes- and anti-stokes lines are localized at frequencies $\omega_i+\omega_q$ and $\omega_i-\omega_q$ respectively. Note that the Raman line shape is Lorentzian[2] [106].

At frequency ω_i (first term in equation 4.10) the light is scattered elastically (Rayleigh scattering). The second and third term in equation 4.10 represent inelastically scattered light (Raman scattering), wherein the frequency of incident light is downshifted (stokes) or upshifted (anti-stokes) by the vibration frequency of atom ω_q (Fig. 4.6).

[2] This is a consequence of the fact that the photon excitation can be modelled as damped harmonic , damped by the interaction with other excitations in the system.

4.5.2 Raman Spectrum of graphene

Raman spectroscopy is a non-invasive method to probe phonons in graphene [101, 105]. It can be used to identify the number of graphene layers [101], estimate the amount of doping and the presence of disorder [95, 102, 103], study graphene's edges [36, 104, 108], and quantify anharmonic processes and thermal conductivity [30, 32].

The typical features in a Raman spectrum of graphene are the G- (~1580 cm^{-1}) and the 2D- mode (~2700 cm^{-1}) [94]. To interpret the Raman spectra in graphene it is essentially to understand the phonon dispersion of graphene [31], which is very elegantly described in [31].

The unit cell of graphene contains two atoms and thus there are six phonon bands [31]. Therefore, there are three optical and three acoustic phonon dispersion branches. Since within the framework of this dissertation only G- and 2D-modes are important, i focus only on them. The G-mode corresponds to a first order Raman scattering process [28] and it is due to the in-plane stretching of the carbon-carbon bonds [29] (Fig. 4.7). Noteworthy, two optical branches at the Γ-point[3], iLO and iTO (Fig. 4.7) correspond to the same frequency, i. e. this Γ-point phonon is doubly degenerated [41]. Therefore, two phonon branches corresponding to the G-mode are depicted in figure 4.7 (inset above the G-mode).

[3] A symmetry point in phonon dispersion of graphene at the center of the graphene's brillouin zone

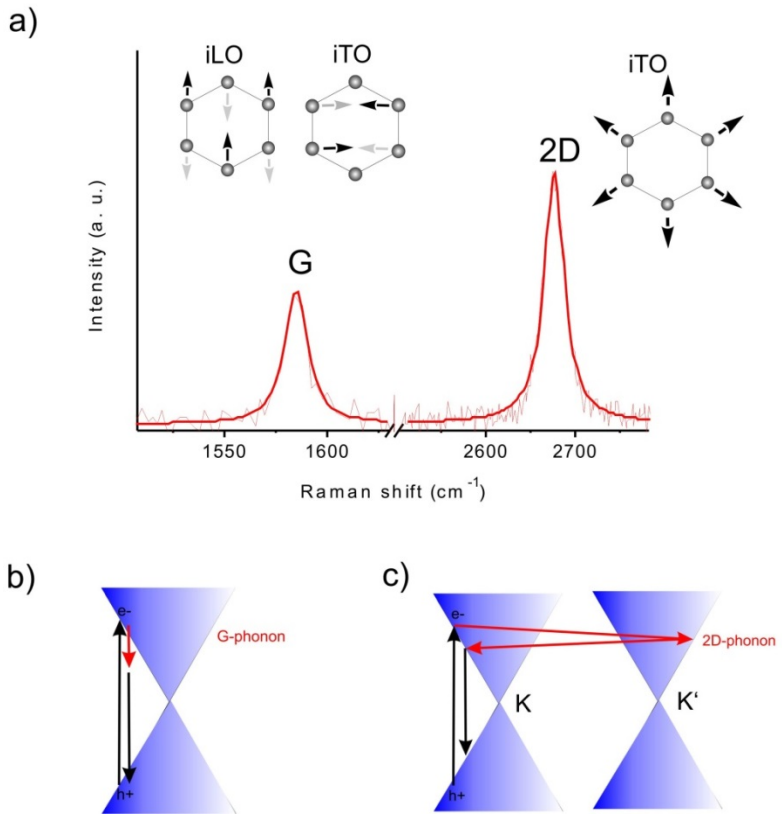

Fig. 4.7: Raman spectrum of graphene with pronounced G- and 2D- modes with Lorentzian fits (a). The insets represent different phonon vibrations corresponding to each Raman peak. iLO and iTO stands for in-plane longitudinal optical and in-plane transversal optical branch, respectively. Schematic representation of a single- (b) and double-resonance process (c) corresponding to G- and 2D-modes respectively. The blue cones in (b, c) indicate the linear dispersion of the electronic structure of graphene at the K- (left) and K'-point (right) (c).

The vibrations associated with the 2D mode are depicted in figure 4.7 near to the 2D-peak. In contrast to the G-modes, the 2D-mode arises from a second order resonance process [29], to which two phonons with opposite wave vectors participate [42]. In this second order resonance process an incident phonon excites an electron-hole pair, then the electron and hole experience scattering on TO phonons and the process is finished by the recombination of the electron-hole pair with the emission of a photon [41].

4.6 Humidity controlled Raman Spectroscopy

The experimental set-up used in this work for Raman Spectroscopy within a RH-Control chamber is depicted in Fig. 4.8. This set-up allows to probe samples, in particular graphenes, at different RH.

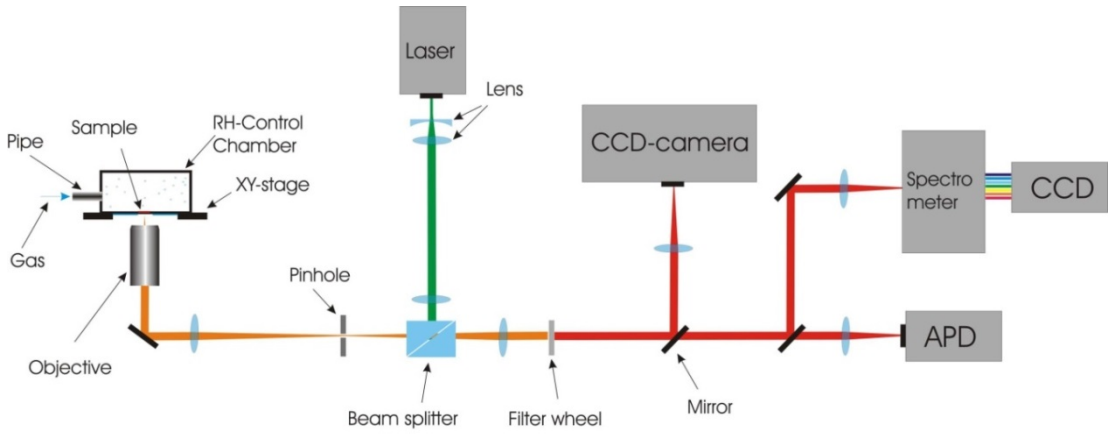

Fig. 4.8: Schematic representation of the experimental set-up for humidity dependent Raman Spectroscopy.

A diffraction limited laser spot (532 nm, 1.4 mW) with a spot size of approximately 1µm was used as the excitation source for the Raman measurements. The spectrometer SP-150, Acton Research Corporation, equipped with a LN/CCD-1340/100-EB/1, Roper Scientific was used. The accuracy to detect peak-shifts was better than 2 cm^{-1}. A CCD-camera was used to identify the graphenes. An avalanche photodiode (APD) was used to record reflection images upon scanning of the sample. This allowed to place the laser spot onto a position of interest. For the humidity variation the samples were placed inside the RH-control chamber (Fig. 4.8), purged either directly with dry nitrogen or with dry nitrogen bubbled through Milli-Q water to reduce and increase the RH, respectively. RH and temperature were measured with a sensor **(**testo 635 of Testo GmbH) located in close proximity of the SFM head.

4.7 Humidity controlled SFM-, KPFM and EFM-Experiments

This section provides a brief description of the set-up for humidity controlled SFM-, KPFM- and EFM-Experiments. The instrument, which was used for the SFM-, EFM- and KPFM-Experiments, was a Scanning force microscope (Digital Instruments – Nanoscope IV).

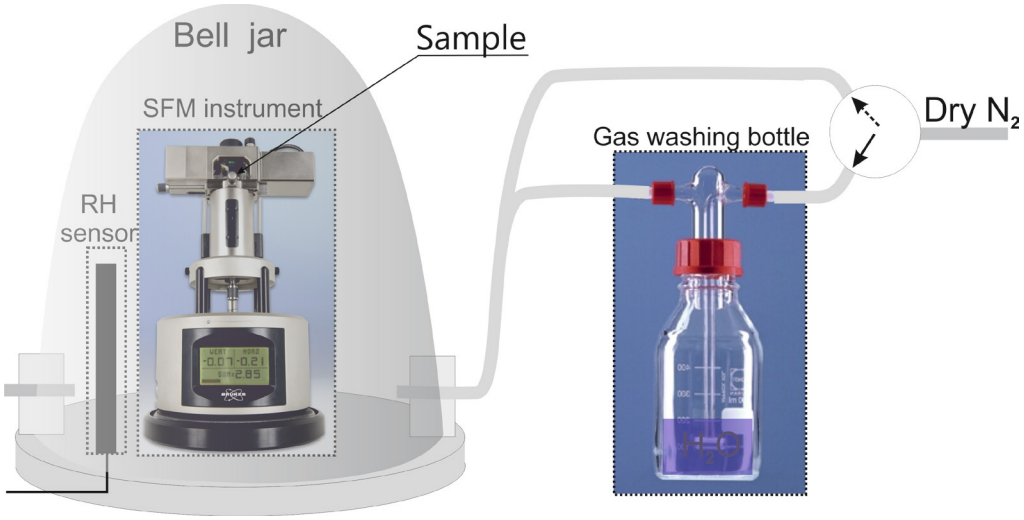

Fig. 4.9: Experimental set up for humidity controlled SFM, EFM and KPFM-Experiments.

The instrument was placed inside a chamber (Fig. 4.9) and purged either with dry nitrogen or with with dry nitrogen bubbled through Milli-Q water to decrease or increase the RH, respectively.

4.8 UV-VIS

UV-VIS spectroscopy has been employed to characterize the optical transmission of the films presented in section 5.4. The UV-VIS-Spectra of the dried films on various plastic substrates were taken using the Absorption-Spectrometer SHIMADZU UV2101 (revision 2.2). Measurements were performed against a reference sample, such that the signal difference is caused only by the dry film itself.

4.9 TEM-imaging

To characterize the dispersions presented in section 5.4 transmission electron microscopy (TEM) has been employed. TEM was performed with a JEOL JEM2100 transmission electron microscope at a beam energy of 200 keV (LaB6 illumination).

4.10 Sheet resistance

For the sheet resistance measurements, two contacts were drawn by a silver colloid solution, separated by a square area of a transparent electrode, and then the resistance was measured by a zero-calibrated multimeter. The average resistance was obtained from five measurements. To ensure the correctness of the sheet resistance measurements, the sheet resistance measured with a home-built four-point probe was compared and no noticeable differences were detected.

5. Results and Discussion

5.1 Layer dependent Surface potential variations of few layer graphenes (FLG) on mica

5.1.1 Introduction

The Electronic properties of graphene are strongly sensitive to the underlying substrate [1, 48, 109]. The quantitative understanding of charge transfer at interfaces and the spatial distribution of the resulting charge carriers is a critical input to electronic device design [2]. Particularly, the performance and reliability of a graphene field effect transistor (FET) can be dominated by the graphene/substrate environment [2, 110-112].

Kelvin Probe Force Microscopy (KPFM) is a versatile tool for quantitative and qualitative investigations of electronic properties of surfaces at the nanoscale. It has been applied to monitor the formation of dipoles at the graphene/substrate interface as well as the distribution of charge carriers in different graphene layers [48].

Mica is atomically flat dielectric substrate and therefore graphene on mica is of high-quality, since mica provides atomically flat support over large areas [72]. Therefore, graphene on mica is of high technological interest.

The surface potential variations of single and few-layer graphene sheets on mica were investigated by means of Scanning Force Microscopy (SFM), Kelvin Probe Force microscopy (KPFM). It will be demonstrated that the surface potential variation of graphene on mica decreases exponentially with the graphene thickness. From this dependency the electrostatic screening length is estimated to 1.3 nm (≈4 layers), which is in excellent agreement with the screening length in graphite estimated experimentally. [92]. Moreover It will be shown that the Thomas-Fermi approach, which predicts a power-law dependence of the surface potential decrease and describes the screening of graphene on SiO_2 [96], does not fit for graphene on mica.

5.1.2 Experimental

Graphenes were mechanically exfoliated onto a freshly cleaved muscovite mica surface and verified following the procedure described in section 2.1.4. KPFM measurements were performed according to section 4.3. Mica sheets were glued onto metal discs with silver colloidal solution. The discs were used as back electrode for KPFM measurements. Thicknesses of mica sheets were in the range 50-100 □m. The typical time between sample preparation and SFM imaging was half an hour.

5.1.3 Results

Figure 5.1a displays SFM height-images of the graphene topography on mica with different number of graphene layers. From the KPFM image (Fig. 5.1b), surface potentials of single-, bi-, and triple-layer graphenes were determined relative to the bulk graphite (see below), using the histogram (Fig. 5.1c) to -108mV, -45mV, and -18mV, respectively. The distribution of the surface potential within the graphene layers was amazingly homogeneous with a scattering of only 1.7±0.1 mV (Fig. 5.1d), which, within the error, is equal for single-, bi- and triple- layer graphene.

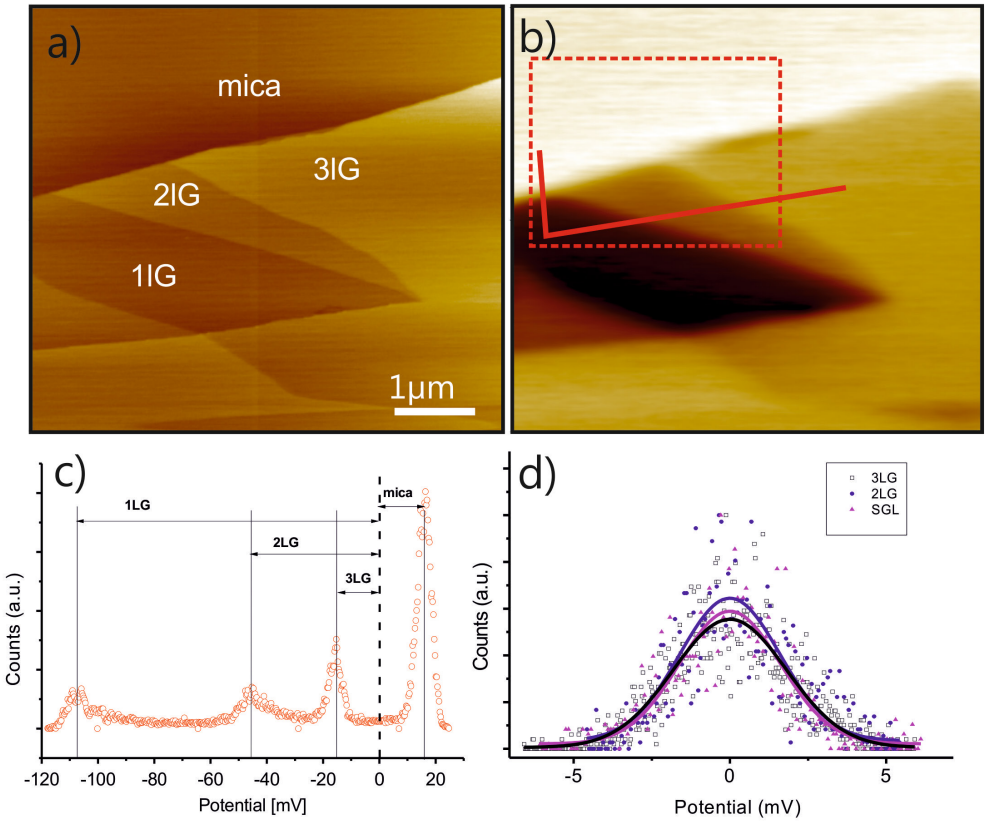

Fig. 5.1: SFM-height image (a) and the corresponding surface potential map (b) of single and few-layer graphenes on mica. (c) Histogram of the surface potential distribution (relative to bulk graphite) acquired from the dashed red region in (b) containing mica, single, bi and triple-layer graphene. (d) Normalized histograms of the surface potentials taken from single, bi- and triple layer graphene regions in (b). The histograms were fitted with Gaussians with standard deviations of 1.7±0.1 mV.

The cross-section of the surface potential (SP) taken across a region going through mica, single, bi-, triple- and four-layer graphene is depicted in Fig. 5.2a. Remarkably, the SP of mica is larger than of single graphene. The SP-difference of FLG relative to bulk graphite is depicted in Fig. 5.2b. Noticeably, the surface potential of FLG increases with increasing graphene thickness, approaching a limit for graphenes containing five and more layers (Fig. 5.2b). A SP of 11-layer graphene (-120 mV) was considered as bulk since the SP variations starting from 5 layer graphene did not change any more.

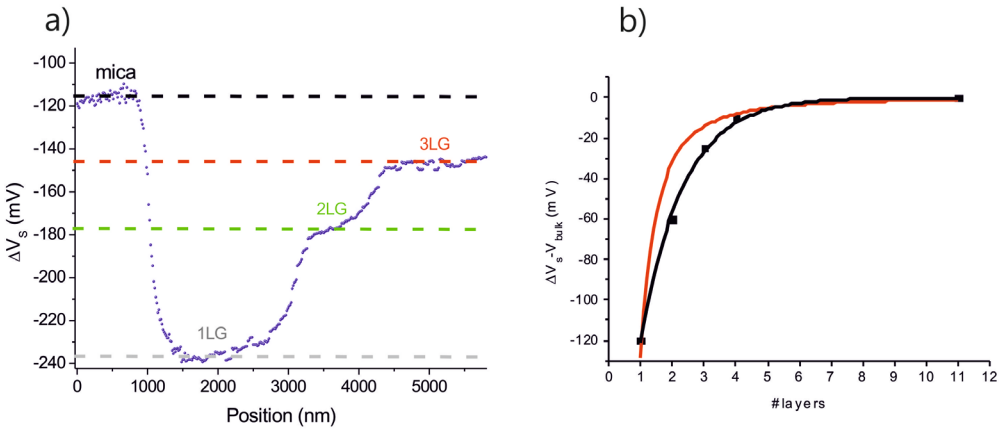

Fig. 5.2: Surface potential cross section taken from the red line in Fig. 5.1b across mica, single, bi- and triple-layer graphene (a). Dependence of the surface potential of graphene versus graphene layer thickness relative to bulk graphite (b) with corresponding fits. The red curve corresponds to the surface potential dependence derived from the Thomas-Fermi model [96] and the black curve is an exponential fit.

Each point in Fig. 5.2b is an average from three different samples. The screening length estimated from the exponential fit (Fig. 5.2b) is (1.3±0.1) nm, which is equal to four graphene layers.

5.1.4 Discussion

The increasing surface potential of graphene with increasing graphene thickness implies p-doping of graphene [48, 49, 96, 113]. The small scattering of the data arising mainly from the KPFM resolution of the surface potential indicates that no large contaminations or charged domains are present at the graphene mica interface. In contrast, in previous studies of graphene on SiO_2, strong surface potential fluctuations within one graphene layer were induced by partial screening of charged impurities at the graphene SiO_2 interface [48, 114]. The findings here confirm the high quality of graphenes on mica which are not only atomically flat [72] but also exhibit very small surface potential fluctuations.

While the surface potential variations within each graphene layer are vanishingly small, there are surface potential differences between adjacent graphene layers. Remarkably, the surface potential scales exponentially with the graphene layer thickness,

approaching saturation at about five graphene layers. In previous studies [49, 96, 97, 115] the dependence of the surface potential of graphene on the number of layers was successfully described with Thomas-Fermi theory. This predicts that the charge-transfer between graphene and the substrate drives the surface potential contrast of a single layer, while the free mobile charges in the subsequent graphene layers effectively screen the surface potential, which is then completely screened off after approaching a bulk limit of five layers [96].

Thus a few layer graphene with a number of layers > 5 layers exhibits characteristics of a bulk metal with an equipotential surface, where the influence from the underlying substrate is completely gone. The final result of the Thomas-Fermi approach is that the surface potential of graphene scales with ~$1/D^2$, where D is the graphene layer thickness [96]. It has been also intended here to use Thomas-Fermi theory to explain the results (Fig. 5.2a, red curve), but it was not consistent with the experimental data (Fig. 5.2b).

This can be attributed to the different interaction between graphene and the mica substrate compared to graphene and SiO_2. Noteworthy, it was already demonstrated that doping of graphene and thereby the direction of the dipoles at the graphene/substrate interface is crucially dependent on the preparation methods of graphenes and it is strongly influenced by the underlying substrate [42, 97, 109, 116, 117]. The last has been attributed to p-doping [41, 97, 109, 115] or to an effective blocking of the charge transfer between graphene and the substrate [97]. These results imply that the screening properties of graphenes are sensitive to the preparation method.

The exponential increase of the surface potential with the graphene layer thickness might be attributed to the screening by massive charge carriers [96]. Indeed it has been demonstrated that the interlayer screening in graphene can be exponential [118], which is a consequence of graphene interlayer coupling. The interaction between graphene layers as well as the interaction between graphene and the substrate can affect the character of the π wave function in graphene as it has been experimentally demonstrated using Angle-Resolved-Photoemission Spectroscopy ARPES [118]. The latter can result in π-band splitting and lead to an electronic transition from two dimensional in single layer graphene to three dimensional in the multilayer graphene [118].

In conclusion, the electrostatic screening of single and few-layer graphenes on mica has been experimentally demonstrated. The surface potential generated by interfacial dipoles at the graphene/mica interface and its dependence on the number of graphene layers has been probed by KPFM. The surface potential decreases exponentially with the number of graphene layers with a screening length of 4 graphene layers.

5.2 Dependence of charge transfer between water and graphene on the thickness of the water film

5.2.1 Introduction

Charge transfer (CT) at interfaces of solids and molecular adsorbates is of fundamental and practical importance in the fields like organic light emitting diodes (OLEDs), photo-catalyzes, photo-voltaic processes and electronics [119, 120]. Doping of graphenes by molecular adsorbates, i.e. chemical doping, is considered as a promising route to control electron transport in graphenes. Formation of water adlayers is ubiquitous at ambient, therefore charge transfer between water molecules and graphene is of a practical importance. In particular magnitude and direction of CT between water molecules and graphene onto which they adsorb has been predicted to vary depending on the structure of the water layers [117, 121, 122].

There is discrepancy in the recent literature reports on charge transfer between water molecules and graphene. It has been reported that single water molecule adsorption dopes graphenes with holes [123]. Layers of water molecules confined between graphene and solid support have been reported to dope graphene positively with doping growing with the water layer thickness [117] but also to block charge transfer between graphene and mica substrate [116]. The later implies no graphene doping by the interfacial water molecules. It has ben also argued recently that water layers confined between graphene and mica can be substantially impacted by contaminations due to sample preparation [42] . Therefore, I investigated graphene samples exfoliated on mica in a particular clean way. I will demonstrate in the following that my graphene samples on mica are substantially different from the previous report [116]. Mica does not dope graphene in my hands, while water layers dope graphene positively with doping increasing for water layer thickness.

5.2.2 Experimental

Graphenes were mechanically exfoliated onto a freshly cleaved muscovite mica surface and verified following the procedure described in section 2.1.4.

Mica sheets were glued onto metal discs with silver colloidal solution, the discs were used as back electrode for EFM measurements. Thicknesses of mica sheets were in the range of 50÷100 μm verified with mechanical profilometer. The typical time between sample preparation and SFM imaging was half an hour. The heads of the employed SFM instruments were operated inside a bell-jar chamber, purged either directly with dry nitrogen to reduce, or with dry nitrogen bubbled through Milli-Q water to increase RH. RH and temperature were measured with a sensor **(**testo 635 of Testo GmbH) located in close proximity of the SFM head. The calibration fidelity of the sensor is ±2.5% RH in the addressed RH range, as provided by the manufacturing company. RH values indicated in the text are the displayed values. Scanning force microscope (Digital Instruments – Nanoscope IV) was operated in tapping mode with a J-scanner at a typical scan rate of 6 minutes per image with SiN cantilevers with typical resonance frequencies of 300 kHz and the spring constants of 42N/m.

The EFM measurements were performed according to the procedure described in section 4.2.

A diffraction limited laser spot (532 nm, 1.4 mW) was used as the excitation source for the Raman measurements. The spectrometer (SP-150, Acton Research Corporation, equipped with a LN/CCD-1340/100-EB/1, Roper Scientific). The heads of the employed SFM instruments were operated inside a home-built environmental control system, bell-jar chamber, purged directly either with dry nitrogen or with dry nitrogen bubbled through Milli-Q water to decrease or increase humidity respectively. Relative humidity (RH) and temperature were measured with a sensor (testo 635 of Testo GmbH) located in close proximity of the SFM head. I investigated three different samples and acquired more than 70 Raman-spectra. The G and 2D modes in spectra were fitted with Lorentzian functions to determine the peak positions.

5.2.3 Results

Figure 5.3 displays SFM height images of a single layer graphene attached to a double layer graphene, acquired under variable RHs. At the initial 26% ambient RH graphene exhibits 2.8±0.5 Å depressions (Fig. 5.3a). Increase of humidity eliminates the depressions, such that at 50% RH graphene becomes flat. Raising of the humidity up to 90% causes growth of flat and compact protrusions in the graphene topography with a height of 5.0±0.5 Å with the error being standard deviation. Protrusions grow more readily within thinner graphenes (Fig. 5.4). Subsequent drying with dry nitrogen flow caused shrinkage of most protrusions and their eventual vanishing. In a few cases it was observed that protrusions that were exceeding few micrometers in diameter still did not completely vanish after 60 minutes of drying.

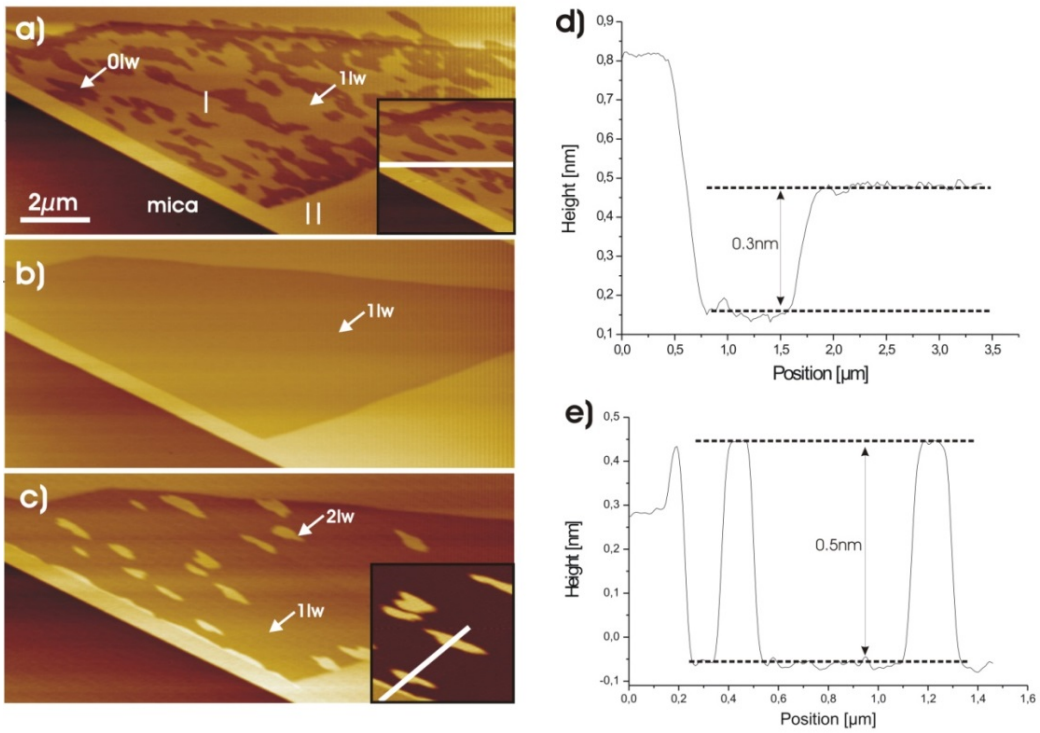

Fig. 5.3: SFM height images of single layer graphene (highlighted with dashed line) next to double layer graphene, taken under variable RHs. a) ambient 26%, b) 50% and c) 90% RHs. d) and e) are cross sections taken along the solid lines on the inserts in a) and b) respectively.

Dependence of graphene topography on relative humidity has been attributed previously to a fluid layer of water molecules wetting the slit pore between graphene and

mica surface [4] with graphene replicating topography of the layer.

At ambient humidities below 30% RH the depressions were attributed to the layer not yet completely wetting the pore. The depressions are attributed to graphene lying directly on mica substrate. Furthermore, protrusions growing in graphene topography are attributed to the variable thickness of the water layer confined in the pore and replicated by the graphene topography (Fig. 5.3). This is supported by the dependence of EFM contrast on the thickness of graphene (see below). The flatness of graphene supported by a monolayer of water molecules at intermediate humidities indicates homogeneity of the water layer and consequently absence of any substantial defects or contaminations confined between graphene and mica substrate (Fig. 5.3b) [42]. The height of protrusions at high RHs substantially exceeds the depth of the depressions at low RHs. Therefore, protrusions cannot be explained with the growth of the second layer of water molecules on top of the first one with the structure identical to the first layer; rather structure of water film within protrusions must be different from that of a monolayer. Different structures of the water film confined under graphene could give rise to different doping levels of graphene. Thus I proceed with EFM to map electrostatic potential and Raman to quantify graphene doping. It will be designate in the following graphene in direct contact with mica as 0lw, on monolayer of water molecules as 1lw and on top of protrusions as 2lw.

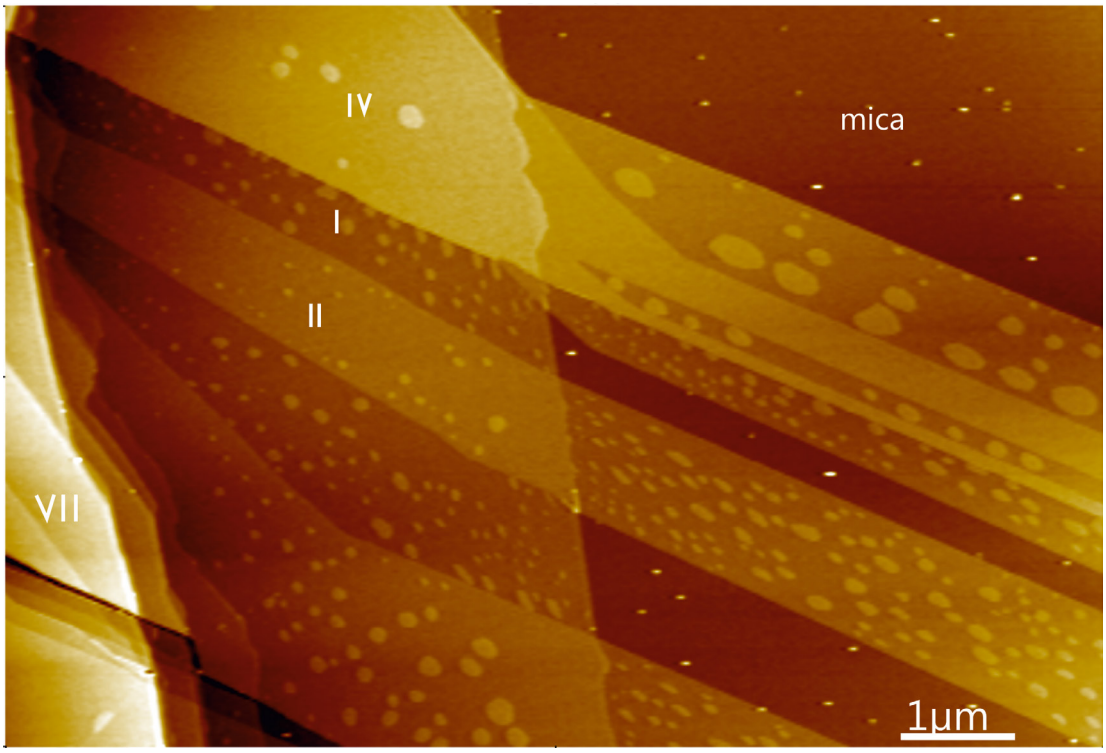

Fig. 5.4: SFM image of graphene flake containing on mica at 95% RH containing graphenes from one to thicker ones around 8 layers. Graphene layer number is labeled with roman numbers.

Figure 5.5 displays SFM height and corresponding EFM phase images acquired on single layer graphenes under variable humidities. Both depressions in graphene topography under low RH and protrusions under high RH can be well recognized. The phase shift dependences on V_{tip} over the 0wl, 1wl and 2wl areas can be well fitted with polynomial of the second order. From the valley point of the parabola (Fig. 5.5 g, h) I estimated the surface potential differences to be +100±20 mV and +100±25 mV between 0wl and 1wl; and between 1lw and 2lw respectively with the errors being the standard deviations. The EFM phase contrast between 0wl-1wl and 1wl-2wl declined with graphene thickness (Fig. 5.6), which is attributed to screening of electrostatic potential by thicker graphenes eventually leading for thicker graphenes to equipotential surface typical for bulk metals [96].

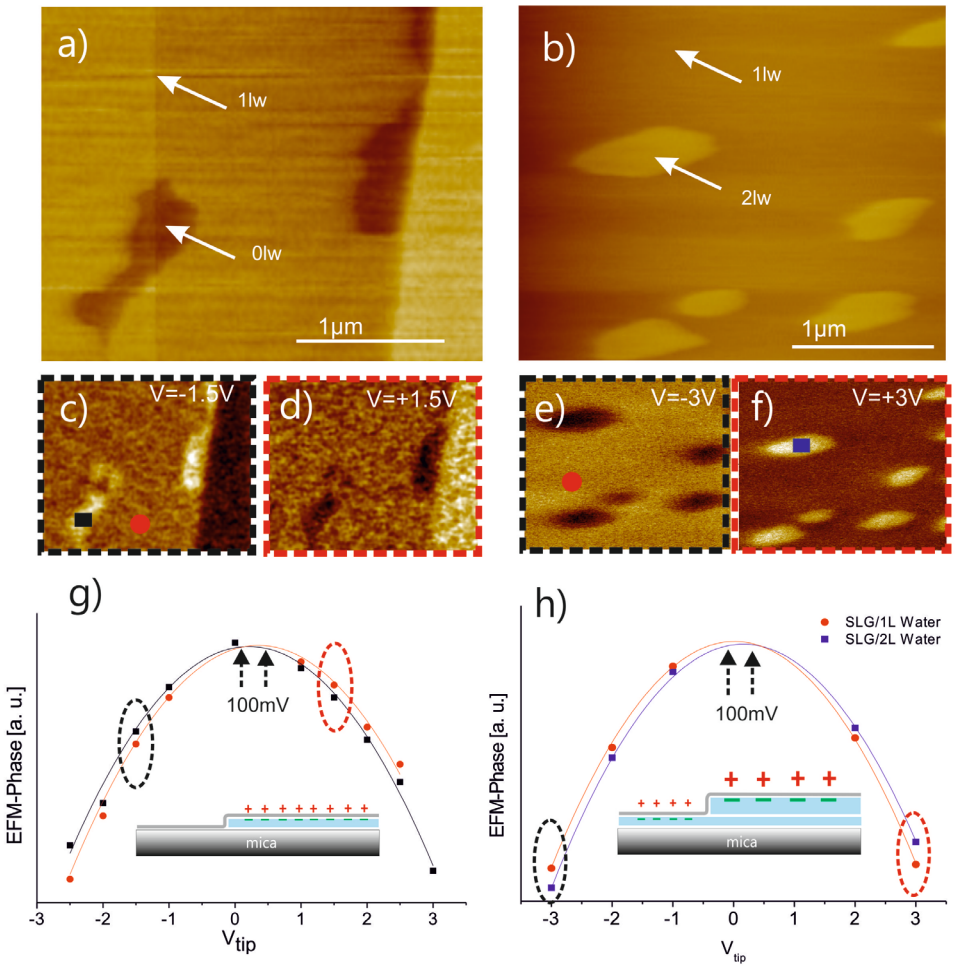

Fig. 5.5: (a) and (b) SFM-height and (c)-(f) corresponding EFM phase images at different tip-bias acquired on a single layer graphenes at different RHs. Electrostatic force spectroscopy (EFS) micrographs taken on 0lw and 1lw (g) and on 1lw and 2lw (h) respectively. Surface potential difference of 100mV is estimated from the valley points of the parabolas.

EFM phase shift is sensitive to local electrostatic potential. Uncompensated charges are unreasonable for samples at ambient, this assumption is also supported by the independence of electrostatic potential on the tip-surface distance (not shown). Decrease of the EFM contrasts with the number of graphene layers implies that the layer of molecules inducing the electrostatic potential differences must be confined between graphene and mica.

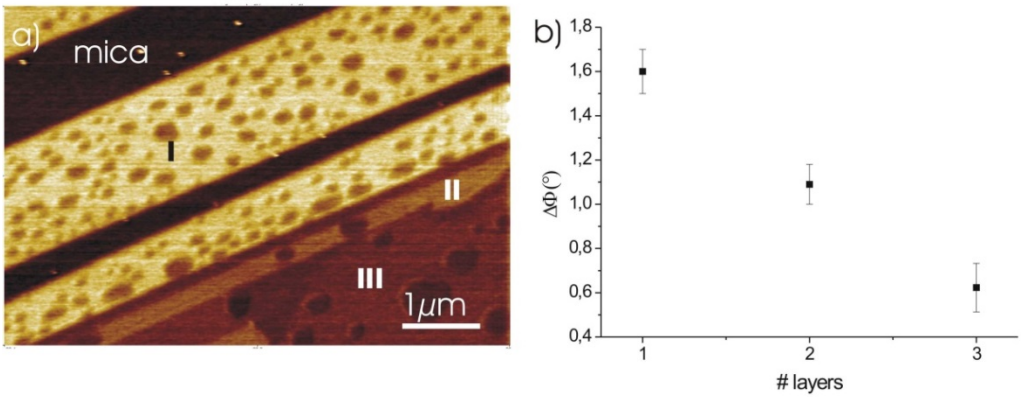

Fig. 5.6: EFM-phase image of few-layer graphene on mica (a). EFM-phase of the 2lw versus graphene thickness.

Thus correlation of electrostatic potential with graphene topography can be attributed to a dipole layer of either ordered water molecules replicated by graphene or of CT between the molecules and graphene or combination thereof. 2D and G Raman peaks of graphene are known to be highly sensitive to graphene doping [49, 113]. Thus, the humidity dependent Raman spectroscopy of single layer graphenes has been performed to quantify their doping levels.

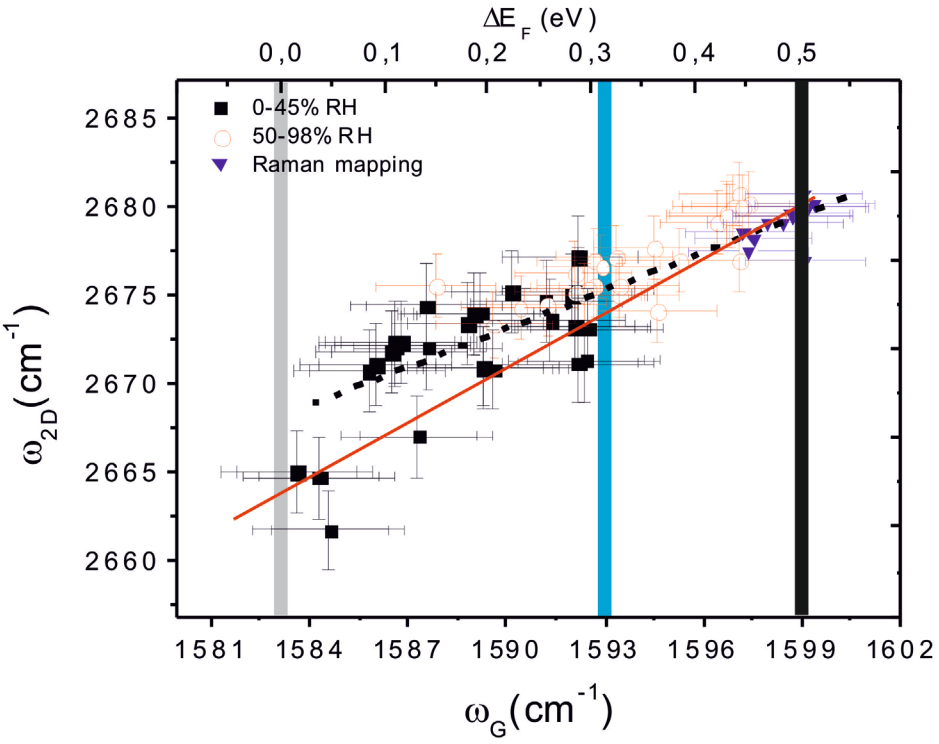

Fig. 5.7: (a) 2D (Y-axis) plotted versus G (X-bottom axis) Raman-modes recorded on single layer graphenes under variable humidities; at 0-45% RH (black squares), 50-98% RH (red hollow circles) and Raman-mapping data from Fig. 5.8, blue triangles. The colored lines in the graphs indicate the positions of the G-modes for undoped graphene (grey), 1lw (blue) and 2lw (black). Line fitting of all data points (red line) gives slope of 0.73±0.05 expected for p-doping of graphene [47]. X-top axis is the Fermi level shift calculated from the position of the G-mode according to [47, 124].

Thus correlation of electrostatic potential with graphene topography can be attributed to a dipole layer of either ordered water molecules replicated by graphene or of CT between the molecules and graphene or combination thereof. 2D and G Raman peaks of graphene are known to be highly sensitive to graphene doping [49, 113]. Thus, I performed humidity dependent Raman spectroscopy of single layer graphenes to quantify their doping levels.

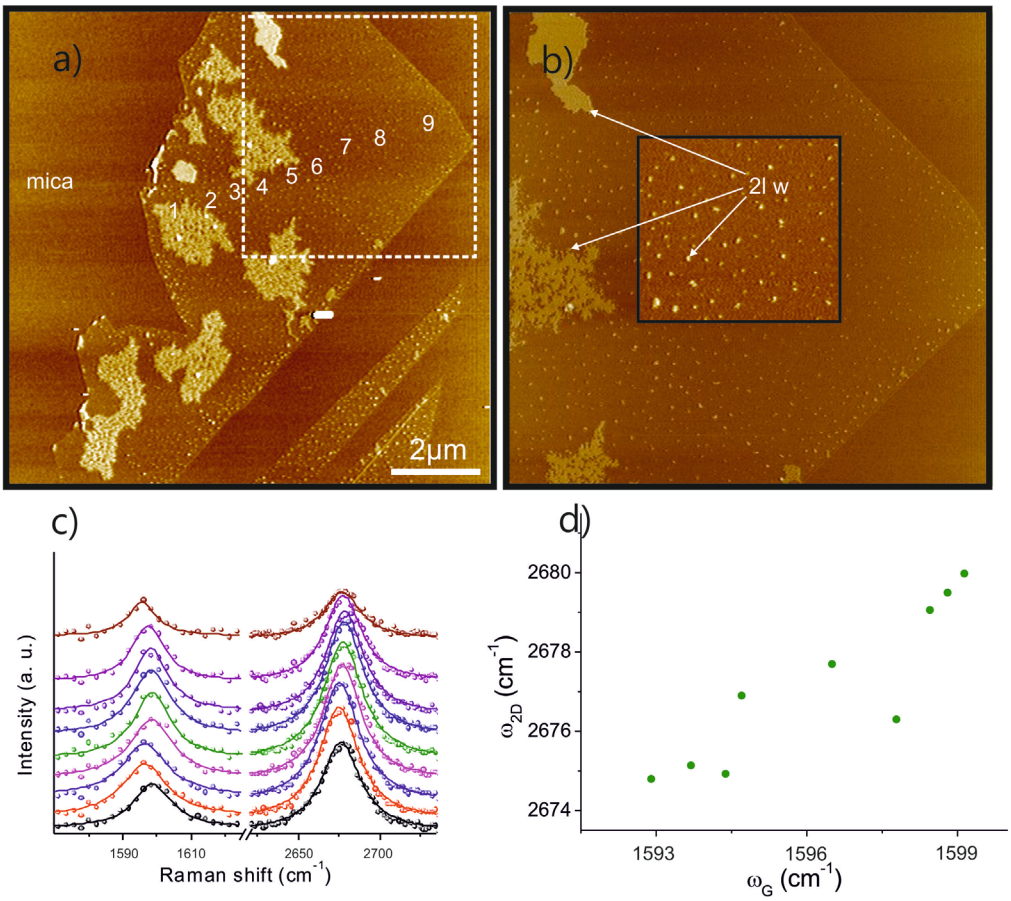

Fig. 5.8: SFM images of graphene flake with the presence of 2lw (bright spots, indicated with white arrows in (b)) and 1lw (surrounding of bright spots) region (a). (b) is the zoom of framed white dashed region in (a). Raman-spectra taken at 45% RH on the sample (a) (starting from bottom to top), mapped along the numbered line, where each Raman-Spectrum in (c) corresponds to the number in (a). The size of the number labels approximately the size of the laser spot. The region of highest G-peak value (red) in (c) correlates with the big 2l w region in (a) (bright features) and smaller G-peak values correlate with 1lw region (surrounding of bright features in (a, b)). (d) represents the position of G- versus 2D-raman mode.

I followed dependences of G and 2D Raman modes on RH for five independent samples. I increased the RH in steps of ten percent and for each RH, I took three to five Raman spectra from different areas within single layer graphenes. Both G and 2D-modes upshift with the increasing of humidity (Fig. 5.7) from 0% to 50% RH, where I found erasing of depressions, and from 50% to 98% RH, where i found growth of protrusions in graphene topography. The upshift of the G-mode is accompanied with the narrowing of its width (Fig. 5.9). Line fitting of 2D on G dependence gives slope of 0.73±0.05 (Fig. 5.7).

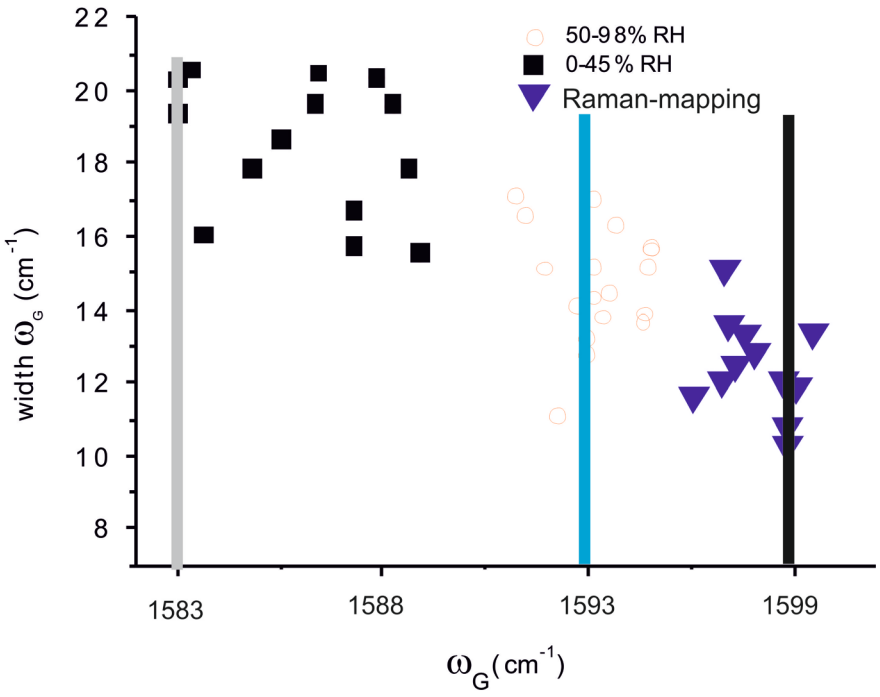

Fig. 5.9: FWHM (width ω_G) versus the position of the G-mode recorded on single layer graphenes under variable humidities; at 0-45% RH (black squares), 50-98% RH (red hollow circles) and Raman-mapping data from Fig. 5.8, blue triangles. The colored lines in the graphs indicate the positions of the G-modes for undoped graphene (grey), 1lw (blue) and 2lw (black).

The experimental setup used in this work does not allow performing *in-situ* SFM imaging and Raman spectroscopy to directly correlate Raman peaks with graphene topography. Yet, Raman mapping combined with subsequent SFM imaging allowed to correlate topography and Raman spectra. That is, SFM imaging of three samples at ambient 8-10% RH, within 24 hours after their exposure to 98% RH revealed large area protrusions in graphene topography (Fig. 5.8). I attributed them to protrusions grown previously at high RHs and still persisting at ambient. The highest surface coverage with islands within the excitation area (laser spot) was nearly 100%, assuming laser spot to be 1 µm in diameter. The Raman spectra taken previously within protrusions show indeed the largest upshifts of G and 2D modes (Fig. 5.8).

5.2.4 Discussion

Upshift of G and 2D Raman modes and the slope of the upshift (Fig. 5.7) implies graphene to be p-doped with doping increasing from 0lw through 1lw to 2lw [125]. Yet scattering of a few data points could be attributed to strains in graphene [125] arising from graphene deformations on wetting and dewetting patterns. The samples we investigated at low RHs exhibited always mixtures of 0lw and 1lw (Fig. 5.3). Therefore, the absolute position of G mode on samples with large 0lw areas implies graphene to be mostly un-doped in direct contact with mica. This conclusion is supported by the observation of substantial broadening of the G-mode (Fig. 5.9) [47]. The shift of the G-mode was recalculated to the Fermi level shift (Fig. 5.7) [47, 124] and graphene charge carrier densities correspondingly. The charge carrier densities for 1lw and 2lw are are (2.9-9) $\cdot 10^{12}$ cm^{-2} and (1.2-2.4) $\cdot 10^{13}$ cm^{-2} respectively estimated following [48, 116], with the bounds estimated from the error margins of G-peak positions.

Muscovite mica is a natural crystal composed of aluminosilicate layers electrostatically bound together by positively charged potassium cations (K+) compensating the negative charge of the layer surfaces [116]. Cleavage of mica propagates along the ionic layers with the potassium ions remaining on either side. Thus the two freshly cleaved mica surfaces must be electrostatically neutral on average. Doping of graphenes exfoliated on mica surface has been predicted to depend on local density of potassium ions and corresponding surface electrostatic charge with zero doping for electrostatically neutral mica surface [70]. The localization of doping has been experimentally demonstrated [4]. EFM phase maps of 0wl areas reveal uniform surface potential within the lateral resolution of the EFM of 60 nm in my case (Fig. 4.5). This, together with the reproducibility from sample to sample of electrostatic potential difference between 0wl and 1wl can be explained with graphene being un-doped in the direct contact with mica. This conclusion is supported by the Raman measurements. Contradiction with the previous reports [4, 116] of graphene to be doped in direct contact with mica can be attributed to high quality of mica in my case with low density of, e.g. ionic impurities. Furthermore, mica cleavage and graphene exfoliation under glove box

conditions in my case could prevent reaction of surface potassium ions with ambient carbon oxides [70].

Positive electrostatic potential shifts from 0lw to 1lw and from 1lw to 2lw can be explained with dipole layers within 1lw and 2lw areas with dipoles pointing upwards, i.e. positive charges being closer to the SFM tip (Fig 5.5 g, h). Raman measurements reveal graphene to be positively doped within the 1lw and 2lw areas, respectively, with doping level within 2lw areas larger to compare with 1lw areas. Electrostatic potential shifts ΔV_z can be estimated from the charge densities σ_q, derived from the Raman measurements, assuming plane capacitor geometry with the charge separation *d*: $\Delta V_z = \sigma_q d/\varepsilon_0$, with ε_0 being the vacuum permittivity. Assuming *d* to be 0.3 nm, i.e. the distance between graphene and neighboring layer of water molecules, ΔV_z can be estimated to be (200-350) meV and (635-1200) meV for the shifts between 0-1lw and 1-2lw respectively. Smaller EFM experimental ΔV_z values could be due to partial screening by single layer graphene [49, 96] or due to depolarization effects.

Increase of graphene hole doping with the thickness of the interfacial layer has been previously demonstrated for graphene on sapphire [117]. It is difficult to discuss exact mechanism of that, still I will discuss one possible explanation in the following. Larger p-doping of graphene within 2lw to compare with 1lw can be due to different structure of the layers and in particular orientation of water molecules within the layers [121, 122, 126, 127]. The 2.8 Å height of 1lw can be explained with a fluid mono-layer of water molecules [73]. The heights of the 2lw areas substantially exceeds the one would expect for the insertion of an additional layer of water molecules with the structure similar to that of the first layer. Thus to explain 2lw height I have to assume insertion of a bilayer of water molecules on top of the 1lw water monolayer. Strains in graphene generated by the additional height of the layer must be overcompensated by the energy gain of the water bilayer structure. Dependence of 2lw area density on graphene thickness indicates the substantial contribution of the strain. This implies water molecules within 2lw to be structurally ordered. The height of the 2lw layer of 5.0±0.5 Å substantially exceeds 3.7 Å, one would expect for an insertion of bilayer of I_h ice [128]. It is tempting to ascribe my case to the bilayer ice predicted to form between two hydrophobic surfaces and experimentally observed to form on graphene at low temperatures [124]. The first layer of

water molecules on hydrophilic and in particular ionic surfaces has been demonstrated to be hydrophobic indeed [124] .

In conclusion, it has been demonstrated that variation of ambient humidity allows modifying local structure of water molecular film confined between graphene and mica. At humidities lower than 30% RH the film de-wets, bringing graphene in direct contact with mica; at humidities higher than 70% RH, i observed growth of 5.0±0.5 Å high islands. I attribute the islands to bi-layers of water molecules growing on top of the first mono-molecular layer. EFM imaging combined with Raman spectroscopy demonstrates that graphene is not doped in direct contact with mica, becomes positively doped on top of a monolayer of water molecules and substantially more positively doped on top of the bi-layer. This demonstrates dependence of graphene doping on the structure of water layer.

5.3 Graphene replicating dendronized polymers

5.3.1 Introduction

Graphene has been demonstrated to be highly bendable and stretchable to follow the topography of a solid surface with the precision down to single macromolecules (N. Severin *et al.* [129]). The question remains, in how far the locally strained graphene may have an impact on the conformation of the replicated macromolecules.

Dendronized polymers (denpols) consist of a linear backbone surrounded by a dense cladding of structurally regular dendritic branches (dendrons), anchored to each repeat unit. The diameter of denpols can be systematically tuned by varying the dendron generation (Fig. 5.10).

SFM height measurements of denpols on muscovite mica were reported previously [130, 131]. Mica, a naturally occurring layered crystal exhibits macroscopically large atomically flat hydrophilic cleavage planes. For this reason it is often used for deposition and SFM imaging of nano-sized objects as they can be most easily recognized on an atomically smooth surface. At ambient conditions, mica is covered with a layer of water molecules whose thickness depends on the ambient humidity [73, 132]. The water layer can form a meniscus between SFM tip and mica surface, when the tip comes in contact with the surface [133, 134], thereby influencing SFM imaging. The denpols investigated here are hydrophobic, i.e. they are soluble in chloroform but not in water. Therefore, one can expect different interactions of the SFM tip with the hydrophilic mica surface and the hydrophobic denpols, with the interaction also being dependent on the ambient humidity

[133-135]. Furthermore, soft objects like denpols can deform and even get damaged by the SFM tip hammering on the surface when operating in tapping-mode. The apparent height of the molecules on SFM height images, for the reasons described above, can be expected to be sensitive to the SFM scan parameters.

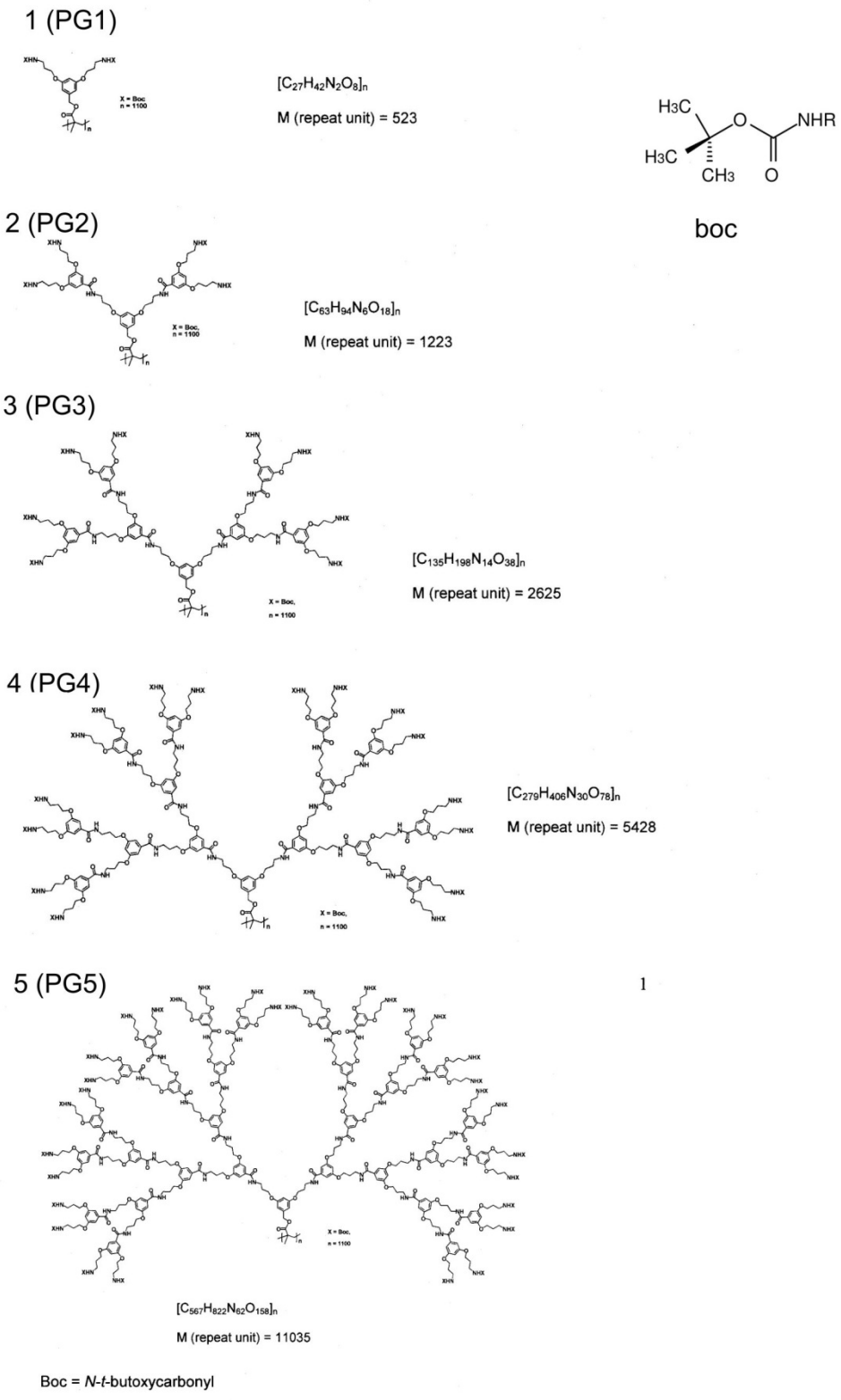

Fig. 5.10: Repeat units of 1-5th generation dendronized polymers with the structural formula of (N-t-butoxycarbonyl) Boc.

In order to follow the topography of the molecules, graphene must become deformed locally and consequently the molecules may be expected to be compressed by the restoring force. In this case, this force [136] and thereby the compression of the molecules may be expected to be proportional to graphene thickness.

Furthermore, even when graphene provides substantial mechanical protection of the covered molecules [129], the pressure developed by the SFM tip can still deform graphene covered molecules. I investigated, whether SFM measured heights of graphene replicas of molecules provide more reliable information on the height of the molecules as compared to measurements of uncovered molecules.

5.3.2 Experimental

The denpols (Fig. 5.10) were deposited onto muscovite mica by spin coating a chloroform solution (1÷10 mg/l) onto a freshly cleaved mica surface at 10-30 rps. Subsequently graphenes were mechanically exfoliated from graphite (Advanced Ceramics, grade ZYB) onto the surface at ambient conditions, as described previously (4). The ambient relative humidities during the preparation were 28÷50% RH. SFM images were recorded with commercial scanning force microscope (SFM, Multimode IV Bruker Corporation) operated in tapping mode using Si cantilevers (Olympus Corp.) with a typical resonance frequency of 300 kHz and a spring constant of 42 N/m. The nominal tip apex radius was 7nm with an upper limit of 10nm as specified by the manufacturer. SFM images were acquired under ~0-60% RH and ambient temperatures. The humidity was lowered by purging the SFM chamber with dry nitrogen and it was raised by purging the SFM chamber with nitrogen bubbling though a gas washing bottle filled with Milli-Q water. First-order line subtraction and plane corrections were applied to SFM images to compensate for thermal drifts and sample inclination.

5.3.3 Results

The topography of graphenes deposited onto mica, which had been pre-covered with denpols replicates well the topography of the molecules. Figure 5.11 displays examples of height and phase images of generation 3 denpols (PG3) on mica covered partially by a few layers of graphene. The surfaces of the graphenes on mica between the denpols are rather smooth (Fig. 5.12), i.e. their height histograms can be well fitted with Gaussian functions with a half width, which can be attributed to instrumental noise (Fig. 5.12b).

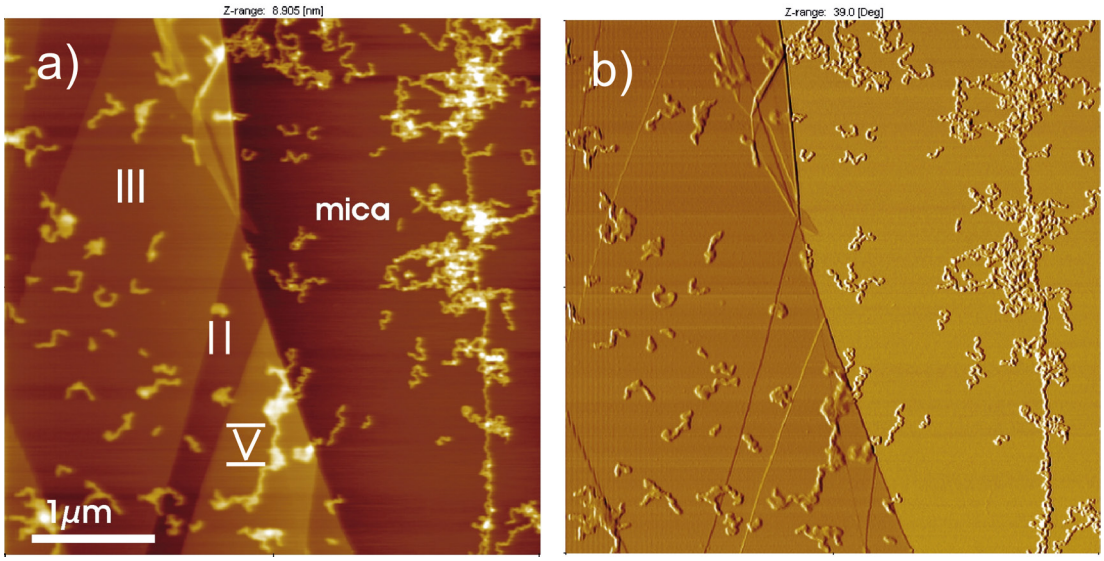

Fig. 5.11: SFM a) height and b) phase image, taken simultaneously of PG3 denpols on mica covered partially by a few layer graphene. Graphene covered areas can be well recognized on the phase image b) by the darker contrast. The area identified optically to be covered with three layers graphene (III) is indicated directly on the image.

The step edges can be attributed to the steps between graphenes of different thickness. The tapping-mode phase of areas covered with graphenes is homogeneous, implying that there is no surface contamination of the graphenes.

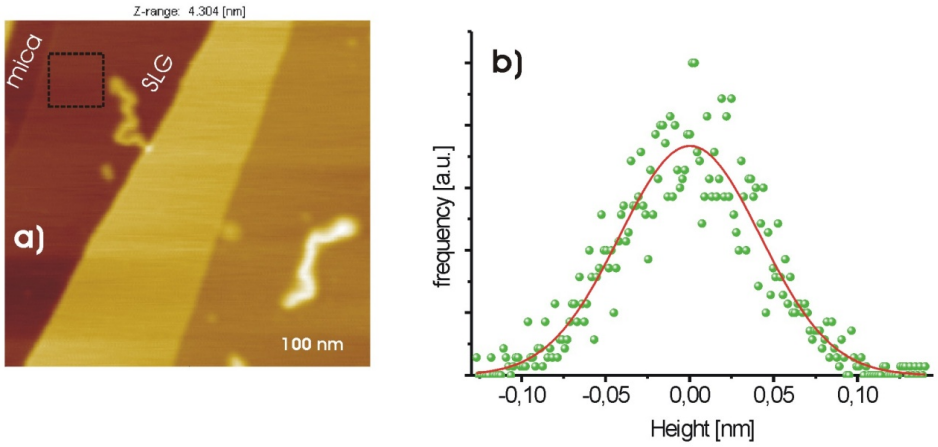

Fig. 5.12: (a) SFM height image of a few layer graphene deposited on a mica surface covered with denpols. Single layer graphene (SLG) is indicated directly on the image for convenience. (b) Histogram from the area indicated in (a) with solid rectangle can be well fitted with a Gaussian function (red line) with standard deviation 42 pm.

Figure 5.13 displays cross sections of denpol graphene replicas and of the uncovered molecules for various SFM cantilever amplitude damping ratios (DR) ($DR \equiv \left(1 - \frac{A_m}{A_r}\right) * 100$, where A_m and A_r are the cantilever amplitudes during measurement and retracted, respectively). Larger damping ratios imply higher pressures from the tip onto the surface during imaging.

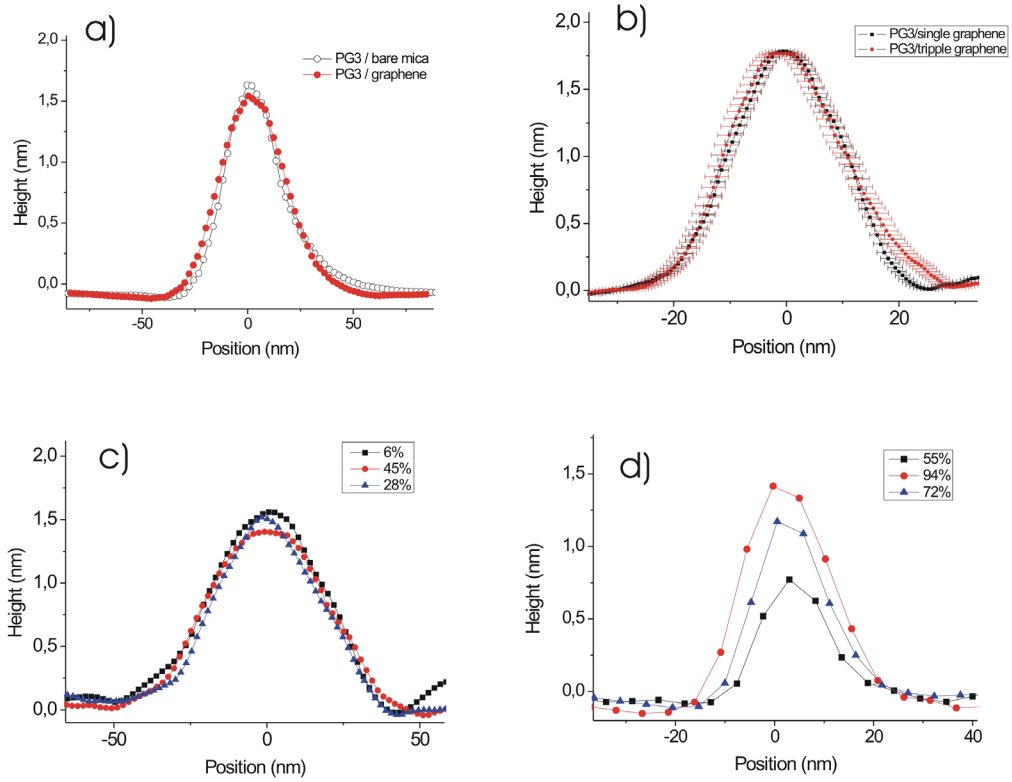

Fig. 5.13: (a) Averaged cross sections of PG3 denpols (averaged on 12 denpols, where six are on bare mica and six PG3 replica. Six cross sections from each denpol) uncovered (black opened circles) and covered with triple layer graphene (red filled circles) estimated from height images taken with 6% DR. (b) Averaged cross sections (averages on two PG3 denpols, one on single and the other on triple graphene replica with 20 cross sections each) of PG3 replicas of graphenes of different thickness indicated directly on the graph for convenience. (c) Averaged cross sections of graphene replicas of PG3 denpols (averages on one denpol, with 11 cross sections) imaged with variable DPs indicated directly on the graph for convenience. (d) Averaged cross sections of uncovered PG3 denpols imaged with variable DPs as indicated directly on the graph for convenience.

Apparent height as well as the full width at half maximum (FWHM) (Fig. 5.13) of the uncovered molecules depend on the scan parameters. The apparent height of uncovered molecules becomes smaller for larger DRs, which can be attributed to either SFM tip compressing or laterally displacing the molecules (Fig. 5.15). Note that uncovered molecules can be also damaged for larger DR as demonstrated in figure. 5.14.

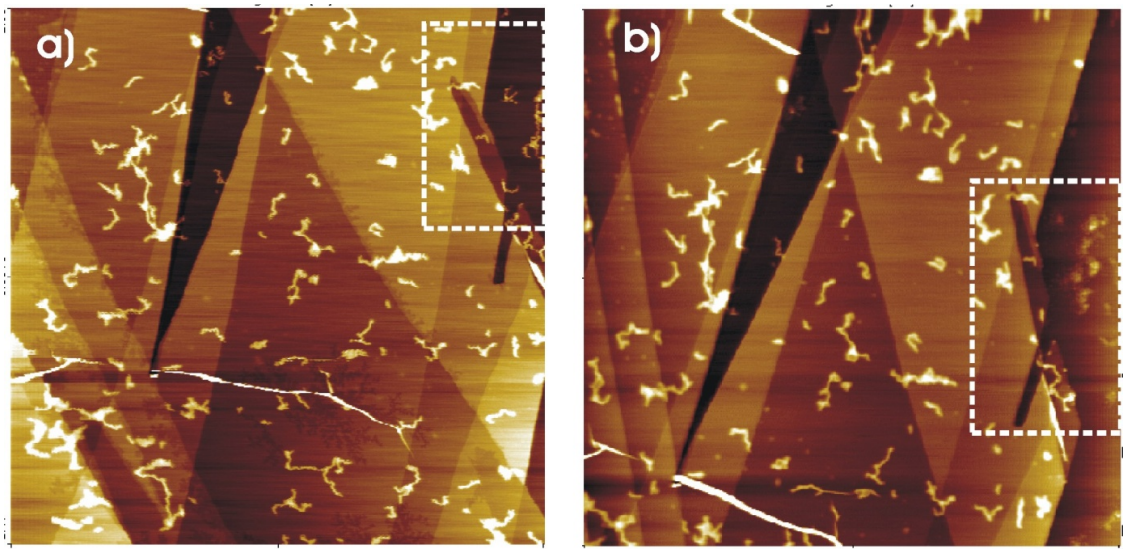

Fig. 5.14: SFM height images of PG3 polymers acquired with a) soft (damping 80%) and b) hard (damping 30%) imaging in tapping mode. Dashed rectangles are guides to the eye and underline areas being not covered with graphene. In soft tapping (a) the denpols are visible and their shapes appear to be similar to that under graphene, while in hard tapping they appear to be partially scratched away (b). Below graphene the denpols are unperturbed irrespective of the SFM damping.

The height of the graphene molecular replicas does neither depend, within the tested range and experimental error, on DR of cantilever amplitude (Fig. 5.13c) nor on the thickness of the graphenes (Fig. 5.13b).

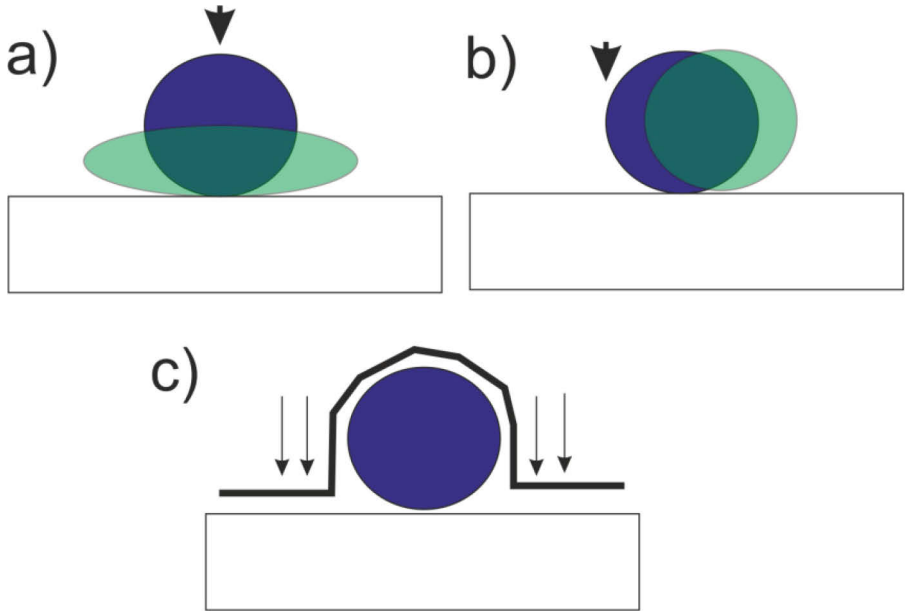

Fig. 5.15: (a) and (b) display schematically two possible denpol deformations due to interaction with the SFM tip. a) SFM tip (arrow) pushes the molecule (blue circle) and deforms it (green ellipse), thereby decreasing its apparent height. (b) SFM Tip punching the molecule displaces it laterally (from the initial blue conformation to displaced green one). This should increase apparent FWHM of the molecule. Reduction of the apparent height is not straightforward, still it is believed it can be justified for the case that the displaced portion of the molecule tends to relax back (i.e. from green to blue) due to the restoration force of the denpol backbone. (c) Graphene conforms to molecules, i.e. adhesion to surface indicated with the arrows is strong enough to deform the graphene shape to the shape of the molecules. This immobilizes the molecules [129], i.e. it reduces lateral displacements occuring in (b). Similarly, it can prohibit deformation of the molecules as in a) in case the molecules are shape persistent in three dimensions.

Thus, taking into account that I proved the apparent height of graphene replica of the molecules to be insensitive to the scan parameters, I carried on with the height measurements of graphene molecular replicas for denpols of generations 1 to 5 (Fig. 5.16).

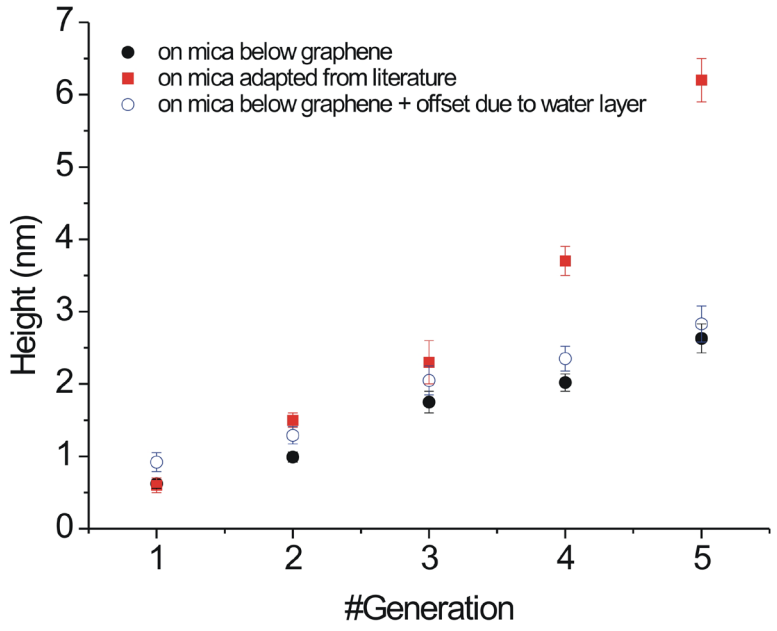

Fig. 5.16: Height of denpol graphene replicas plotted versus denpol generation (black circles). The error bars are the standard deviations. The statistics is baes on 10 different samples, where 30 to 46 single denpols were analysed. For comparison, the literature values [131] of denpol heights on mica (red squares) and heights of denpol graphene replicas offset by the height of the water monolayer (3±0.5 Å, open blue circles, see discussion below) are added.

In order to compare cross sections of uncovered denpols with their graphene replicas, I remind that in the absence of denpols graphene does not lie directly on the mica surface, rather it rests on a monolayer of water molecules, coming from the ambient [73]. To check, whether in the samples investigated here also a monolayer of water exists, I imaged graphene covered denpols at variable humidities and observed the growth of fractal like depressions in graphene planes between denpols with a depth of 3±0.5 Å (Fig. 5.17a), similarly to the case of graphene exfoliated directly on mica [73]. The molecular graphene replicas were not affected upon varying the humidity, except for the case when growing fractal depressions touched or grew “through” the molecules. In this case, the height of graphene replicas of the molecules increased locally on the depth of the fractal depressions (Fig. 5.17d). Increase of the humidity to 50% eliminated the depressions [73]. I considered this as the proof of the existence of the monolayer of water molecules confined between graphene and mica also in this case. The increase of the apparent height of the denpols locally upon receding of the water monolayer implies that the

denpols are embedded in the water layer (Fig. 5.17d). Therefore, the thickness of the water layer (3±0.5 Å) to the measured heights of the denpol graphene replicas was added to estimate the real height of the molecules under graphenes (Fig. 5.16).

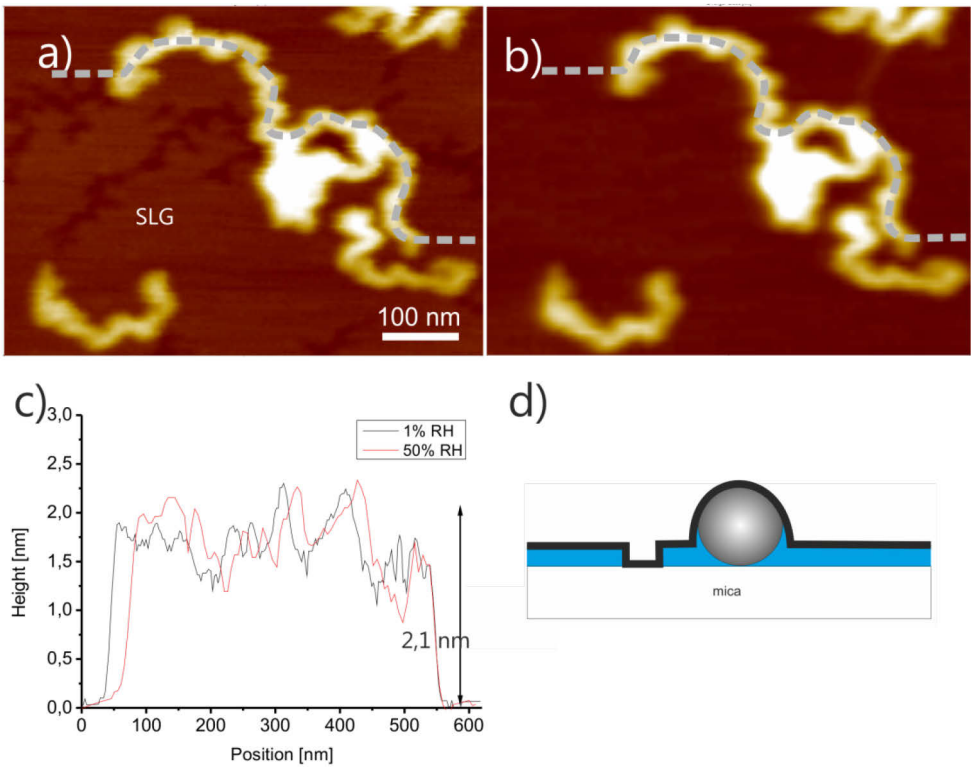

Fig. 5.17: SFM height images of single layer graphene replicas of PG3 denpols on mica recorded at a) 1 % RH, b) the same area as in a) after humidity was raised to 50 % RH c) cross sections along the grey lines indicated in a) and b). d) model: denpols are embedded in a monomolecular layer of water molecules; therefore dewetting of the layer as in a) locally increases the height of the denpols.

5.3.4 Discussion

The results for the heights of denpols covered with graphenes (Fig. 5.16) are somewhat surprising as it will be discuss in the following. One can argue that graphene must become locally deformed to adopt the shape of a denpol and the restoring force of the graphene then tends to flatten the denpols. Young's modulus of a few layers of graphene does not vary largely with the sample thickness and is close to Young's modulus of bulk graphite [137].

The bending elasticity of graphenes grows with the number of graphene layers. Therefore, for a given denpol generation, the graphene restoring forces must grow with the number of graphene layers. Thus one can expect smaller heights of denpols under thicker graphenes, which is however not the case. Furthermore similar heights of covered and uncovered molecules for first through the third denpol generation suggest that the molecules under graphenes do not become flattened by graphene. I find that an average cross section of PG4 denpols on mica on images made with small DPs is the same within the error as the published one. Therefore it is concluded that PG4 denpols become indeed flattened under graphenes, which is attribute to the stiffness of graphene.

Knowing the bending elasticity of graphene and its ability to cover macromolecules with a high level of precision, the results lend themselves to a method to control strain in graphene by means of a nano-structured substrate, which can be realized through nano-structuring of mica with denpols. Since the deformation of graphene scales almost linearly with the diameter of the denpols the deformation of graphene covering the substrate can be tuned through the size of denpols.

In conclusion, SFM measurements of graphene covered dendronized polymers on mica for generations: PG1- PG5 has been performed. The heights of graphene covered denpols on mica are found to be insensitive to the SFM scanning parameters. I find that the heights of graphene covered denpols increase with denpol generation, which is in agreement to the literature. While the height of generations PG1-PG3 denpols covered by graphene are in a good agreement with the heights of uncovered molecules, wherein the height of PG4 and PG5 denpols covered by graphene is substantially smaller. That implies that graphene replicates denpols of generation PG1-PG3 with high precision, while measurements on denpols of generations PG4, PG5 reveal a tendency toward higher generation denpols to become flattened by graphenes, which implies that the bending elasticity of graphenes grows with the number of graphene layers.

These results provide a method to locally control the deformation in graphene and thereby design strain engineered electronic devices [8, 9] .

5.4 Conductive carbon-based inks

This chapter deals with design of conductive carbon-based inks, wherein the inks are produced from mixtures of different carbon-based materials such as graphite, graphene, GO, SWCNT, MWCNT and conductive polymer, PEDOT:PSS.

5.4.1 Scope

The aim of the work presented in this chapter was to design inks for: i) transparent electrodes with the sheet resistance on the order of <100 Ω/square at a transmittance of >75% and ii) conducting non-transparent flexible electrodes with a sheet resistance less than 20 Ohm/square[4]. A common requirement on the inks i) and ii) was to ensure homogeneous and stable dispersion combined with superior film formation resulting in homogeneous dried conductive films without film rupture and coffee ring effects without of using either surfactants or insulating polymeric binders. Additionally the rheology of the inks was optimized for industrial printing methods such as: slot-die coating, dip coating and screen-printing.

In section, 5.4.3 special combination of solvents without usage of surfactants or other additives for fabrication of homogeneous conductive films with functionalized CNTs is presented. This combination is called “Fugitive wettability enhancer” and patented in a patent application (AKZ 102013223569.0). In section 5.4.4 Graphene-CNT-Ink is presented. Transparent electrodes made using the ink are fabricated, using dip coating and characterized electrically and optically. Section 5.4.5 presents SWCNT - PEDOT:PSS – ink, which is used for fabrication of highly conductive and transparent electrodes. Finally, in section 5.4.6 GO-based ink for fabrication of transparent or non-transparent electrodes is presented and the film properties of the ink are discussed.

[4] We also achieved the resistance of less than 1 Ohm/square. In the patent application (AKZ 102013225908.5) highly flexible non-transparent electrodes using conductive binder are described, which can be used as printed IC-interconnects. Their resistance is less than 1 Ohm.

5.4.2 Experimental

Graphene/CNT-Ink

Uncoated and unmodified multiwalled CNTs (Nanostructured and Amorphous Materials Inc.) were dispersed in several different dispersions containing ultrasonically exfoliated graphenes from graphite (Quing Dao Black Dragon Graphite Co., Ltd). Dissolution works both, if i add CNT to a solution of graphenes or if i sonicate a solid mixture of CNT and graphite flakes. Example 1: sonication of graphite flakes and CNTs solid mixture in ethanol, iso-propanol as well as the mixtures of the solvents and water. Example 2: a disperison of graphenes in ethanol has been prepared by sonication of graphite flakes for 20 hours. CNTs were dissolved in the graphene-ethanol solution. Uncoated CNTs are not soluble in ethanol. The dispersion was used for thin film fabrication one day after the sonication was finished. This step is necessary to let undispersed agglomerates settle down at the ground of the bottle.

SWCNT/PEDOT:PSS-Ink

Unmodified SWCNTs (Plasmachem) at concentration 0.5g/L were sonicated in Ethanol and for three minutes. PEDOT:PSS pallettes (AGFA Inc.) were dispersed in deionized water at concentration 8g/L. 20% Ethylene Glycol (EG) and 10% Ethanol was added to the PEDOT:PSS dispersion in deionized water so that the resulting concentration of the ink was: 70% Water, 20% EG and 10% Ethanol. The resulting ink was prepared by adding the PEDOT:PSS dispersion into the SWCNT dispersion in Ethanol so that the concentration of PEDOT:PSS became 3 g/L with 0.2 g/L SWCNT.

GO-based-Ink

A dispersion of graphite (1g/L) (Quing Dao Black Dragon Graphite Co., Ltd) and unmodified MWCNTs (2g/L) (Nanostructured and Amorphous Materials Inc.) in deionized water (50%) and 1-propanol (50%) is ultrasonicated for two hours. A graphene oxide solution in water with concentration of 7g/l was prepared using hummers method [78] and added to graphite/MWCNT dispersion resulting in GO concentration of 4 g/L. Subsequently a solution of PEDOT: PSS as prepared in SWCNT/PEDOT:PSS-Ink was added

at concentration of 2 g/L. The mixture is applied onto a surface of PET by drop casting or dip coating [138, 139].

5.4.3 Fugitive wettability enhancer

The motivation of this part of the work was to avoid thin film rupture of printed ink made from COOH-functionalized CNTs deposited by dip-coating [138] on plastic substrate without any surfactants, binders or other film forming additives of insulating nature. As result a solvent with improved wettability has been developed and successfully applied to other non COOH-functionalized CNT - based inks.

CNTs can be easily deposited onto transparent plastic films to form a transparent conductive coating from solution using diverse printing techniques such as slot-die-coating [24], screen- and ink-jet-printing [25, 26] or roll-to-roll [27] transfer.

The most suitable method to disperse CNTs in water is to functionalize them with COOH-groups [140], which allows to produce homogeneous and stable dispersions. In order to produce conductive ink for deposition on plastic substrates, the following problems need to be solved: i) homogeneous dispersion of CNTs in the ink to provide a good percolation network on the substrate, ii) sufficiently good rheological properties to allow proper wetting of the required substrate, iii) low annealing temperatures (<100°C) (i.e. no amphiphilic molecules) to avoid the degradation of the plastic substrates.

Up to date, there are numerous water based CNT ink formulations. However, their problem is that water has a quite large surface tension (70mN/m), which results in an insufficient wetting of the ink and thereby leads to problems with the deposition of the ink on the substrate. Therefore the substrates may be chemically treated in order to improve the wetting ability of the ink [141]. Chemical treatment however produces functional groups on the substrate and therefore has disadvantages: i) functionalized groups on the substrate produce defects, which can largely reduce the sheet conductivity and ii) it makes the production process more complicated and expensive. Alternatively organic solvents with lower surface tension can be added, which improves the wetting of

the substrate. However commonly used organic co-solvents such as Isopropanol, Ethanol and other alcohols have much lower boiling points that water and therefore the following problems arise: After the substrate is wetted by the dispersion one usually observes phase separation between water and co-solvent as well as inhomogeneous evaporation of the resting solvent causing de-wetting effects. This, in turn, results in inhomogeneous layers with defects and reduced sheet conductivity [56, 142].

A way was found to avoid the problem of phase separation and thereby to produce homogeneous wetting of the substrate with CNT ink without adding any binders and without any high boiling point solvents.

COOH-functionalized MWCNTs (Plasmachem) were used to prepare the ink formulation. Ink has been made of following components: CNT: Water, 1-Propanol. The CNTs were dispersed in deionized water at concentration of 2 g/L with subsequent ultrasonication for 30 minutes. 50% of 1-Propanol was added into the aqueous CNT dispersion. The resulting dispersion was ultrasonicated for 15 minutes. The H_20/1-propanol mixture is remarkable in the following two aspects: Since 1-propanol has a low surface tension (21.22 mN/m at 20°C), it highly increases the wetting ability of CNT-ink compared to the case of pure water. The boiling point of 1-propanol is 97°C (at normal pressure), which is similar to that of water (100°C). Therefore both solvents evaporate with approximately the same rate homogeneously from the substrate without leading to inhomogeneities on the substrate. A transparent conductive electrode is made through deposition of the ink via Dip- and mask-assisted bar-Coating-techniques[5] on PE-foil. For the mask assisted technique a mask was made of 50µm thick PE-foil. Noteworthy, that after each coating step the coated substrate was immediately placed into the oven at 110°C for one minute for curing. Highly clean film preparation conditions are crucial for the quality of resulting films.

Optical image of the CNT-dispersion containing fugitive wettability enhancer is displayed in figure 5.18. The dispersion is homogeneous and stable for several months.

[5] This method is described in Patent application AKZ 102013223569.0

Transparent conducting films made of functionalized CNTs are presented (Fig. 5.18b-d). The films were prepared using mask-assisted bar-coating-techniques, which is a promising tool for fabrication of large area films. To study the film formation I used as reference ink-formulation (Ink-ref) where I replaced 1-propanol by Iso-propanol (boiling point 82°C). The other components of the Ink were the same. The films prepared using ink-ref exhibit poor film forming properties as it is displayed in figure 5.18b (left film) and c). While the films prepared using the ink containing 1-propanol shows homogeneous film (Fig. 5.18b right film and d).

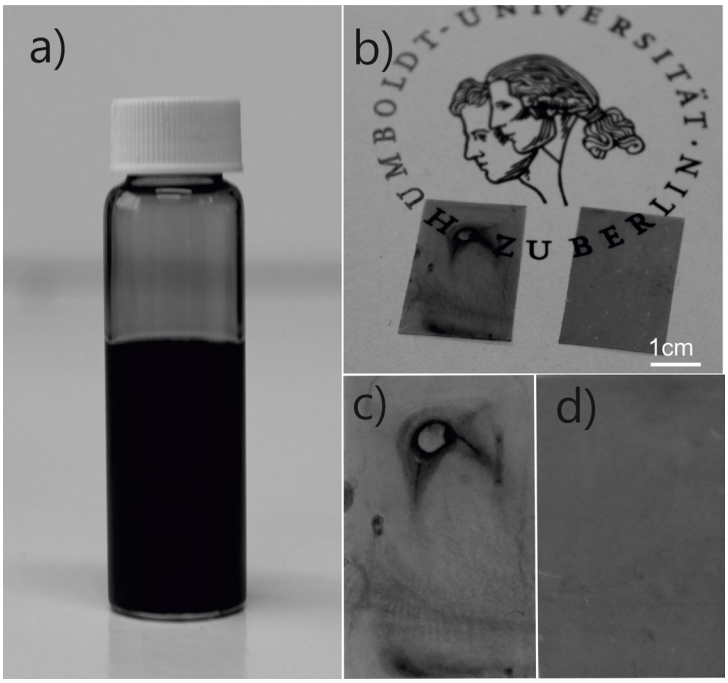

Fig. 5.18: Optical image of the dispersion (a) containing only COOH-functionalized MWCNTs, H_20 and 1-Propanol. Optical images of transparent films on PE with inhomogeneous (c) and homogeneous (d) film formation prepared from ink-ref and the ink containing 1-propanol.

I followed film formation process starting from wet (immediately after coating) to dry film as it is demonstrated in figure 5.19. After coating the wet films are relatively homogeneous for both inks (Fig. 5.19a, d) although some inhomogeneities arising from non-perfect wet film distribution over the substrate are visible. But this phenomenon is of minor nature and doesn't affect the quality of dried film if using the fugitive wettability enhancer as I will show it in the following.

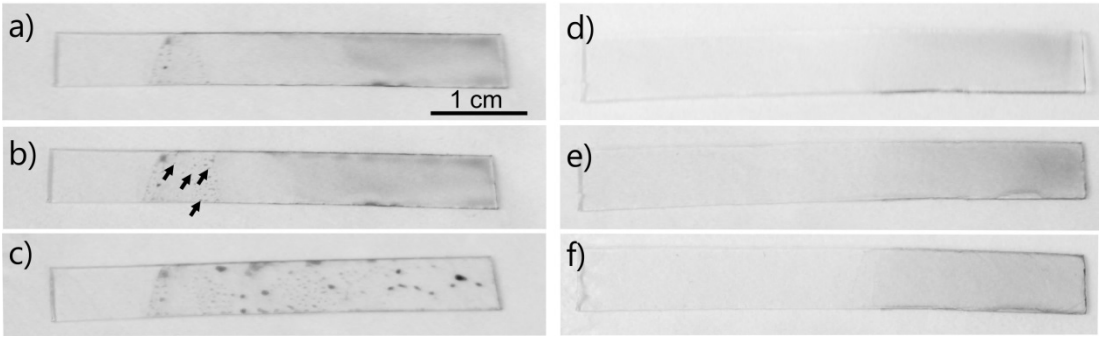

Fig. 5.19: Film formation from wet to dry film for the ink-ref and ink containing 1- propanol. Films of Ink-ref (a-c) and of the ink containing 1-propanol (d-f). Wet films immediately after coating (a, d), after ten seconds (b, e) after five minutes.

Ten seconds after coating the film starts to dry and first inhomogeneities become visible in case of ink-ref as indicated with black arrows in figure 5.19b. While film prepared using Ink containing 1-propanol remains homogeneous. Five minutes after coating the films are dry in both cases and film made using ink-ref is highly inhomogeneous (Fig. 5.19c) containing dark spots and ruptures (dewetts) while film prepared using 1-propanol containing ink is highly homogeneous (Fig. 5.19f).

The physics behind the formation of thin films is quite complex. It was reported that so called marangoni-flows[6] are responsible for the rupture of the thin CNT-films [56]. The authors claimed that the film rupture could be avoided if the dewetting velocity is low enough to allow the liquid film to dry before dewetting causes any defects. In other words, dewetting is avoided when the film drying time is much shorter than the dewetting time [56]. Thus, they attempted to slow down the dewetting by enhancing the viscosity of the coating fluid. To realize it they used special combination of surfactants in combination with SWCNT dispersion in water. However the drawback of using surfactants in fabrication of transparent conducting films is obvious and therefore i looked for alternatives.

To ensure sufficient wetting of the CNT-dispersion on the one hand, which was already shown to be the case upon addition of alcohols to aqueous CNT-dispersion, and minimize the film rupture on the other hand, I used an alcohol that has a boiling point close to that of water. Thus this two-component solvent consisting of water and 1-

[6] Surface tension gradient driven flows within the thin film

propanol eliminates the problem of phase separation and film rupture. The dewetting caused by different evaporation rates of the solvents is eliminated due to approximately the same boiling point of both solvents. An interplay between marangoni-forces and evaporation of the solvent is elegantly described in [143].

These findings provide an experimental support of the proposed phenomenon. Up to today it was a great challenge to produce thin transparent conductive electrodes from solution without of using of surfactants. I introduce a term “fugitive wettability modifier” and provide an alternative method for fabricating thin functional films from solution which is of clear importance for printed electronics.

5.4.4 Graphene – CNT – ink

The aim of this section was to find a way to prepare a homogeneous dispersion with unmodified MWCNTs and without addition of surfactants or any insulating polymers. It was found that addition of graphenes into the MWCNT dispersion helps to homogeneously disperse the CNTs. As result a conductive ink was obtained and transparent electrodes were fabricated using this ink and characterized.

Figure 5.20 a displays the optical image of MWCNTs in Ethanol. One can clearly notice the pure MWCNTs are not soluble in Ethanol since the MWCNTs sediment at the bottom part of the bottle immediately after putting them in Ethanol. Optical image of the dispersion containing graphene and MWCNTs is presented in Fig. 5.20b.

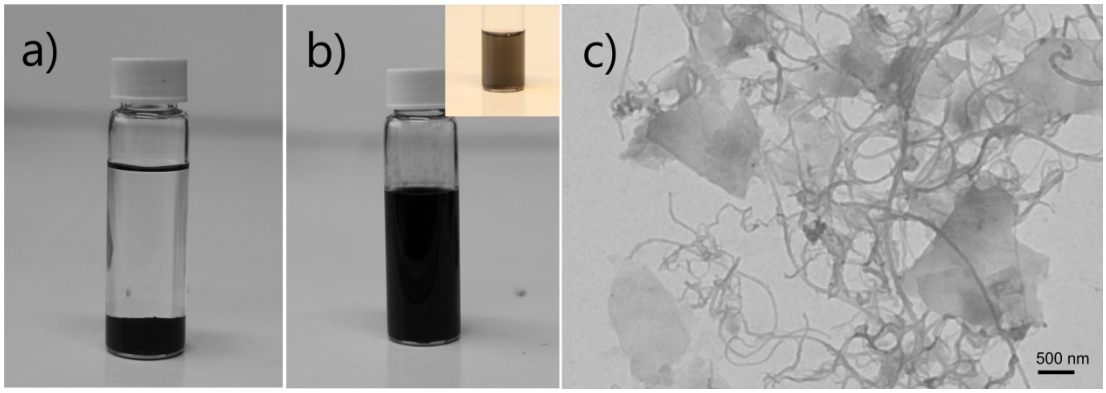

Fig. 5.20: Optical images of MWCNT without graphenes in ethanol (a) and with graphenes after 20 hours sonication (b), five times diluted (inset). TEM-image of MWCNT/graphene - dispersion.

The image implies that together with graphenes the MWCNTs are very well disprsed in Ethanol. The inset in Fig. 5.20b suggests that the dispersion is highly homogeneous without a presence of any agglomerates. TEM-imaging (Fig. 5.20C) suggests that the dispersion indeed contains both components graphenes and MWCNTs.

Films prepared by Dip-Coating [138] of CNT/graphene dispersions are visually very homogeneous, transparent and they are also conductive. The optical images of the transparent films with their optical spectra are presented in figure 5.21a and b. The transmittance versus sheet resistance is depicted in figure 5.21c.

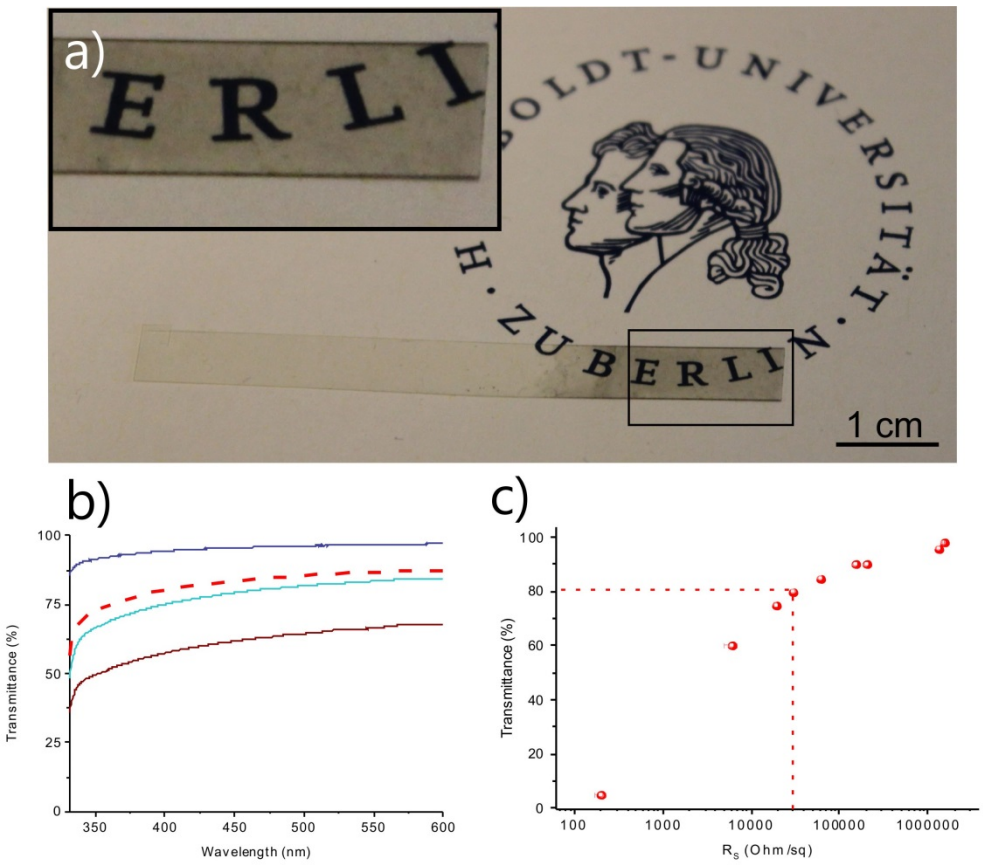

Fig. 5.21: Optical image of MWCNT/graphene film on PET (a) at 80% transmittance (550nm). UV-spectra of the MWCNT/graphene-films (b) taken at different transmittance on PET, where the dashed red curve represents the film in (a). Transmittance versus sheet resistance of the MWCNT/graphene-films on PET (c), the point highlighted with red dashed lines characterizes the film in (a).

A method to prepare solutions of CNTs and graphenes in common solvents is invented. Such solutions can be used, e.g., as low cost ink for printing of highly transparent and highly conducting electrodes, which is of clear technological importance.

The advantage of this method is usage of low cost graphite flakes, CNTs and common solvents including the solvents with low boiling point what makes the solutions suitable for printing on flexible plastic substrates and overcomes thermal annealing at higher temperatures. The most closely related inks patented contain amphiphile molecules to dissolve CNTs [23]. As I discussed above amphiphile molecules worsen electrical conductivity of the resulting films, which this methods overcomes. Graphenes should furthermore stabilize the structure of a graphene-CNT film [144].

It can be envisioned that graphene-CNT solutions invented in this work can be used for preparation of carbon based bulk composite materials. GO – CNT composite materials are considered to be promising for commercialization [145, 146]. Replacement of GO onto graphene can potentially improve tensile strength of the composites due to substantially higher structure integrity of graphenes to compare with GOs; and it should also improve electric conductivity of the composites due to high electric conductivity of graphenes. Furthermore, the inks I invented are fully compatible with the recently published production method of CNT fibrils [147]. Flexible graphene flakes can potentially improve tensile strength of the fibrils.

Moreover such CNT-graphene dispersions can be used to produce surface coatings by, e.g., spray coating [148], which can be envisioned as antistatic, electromagnetic fields shielding and anticorrosive coatings.

5.4.5 SWCNT/PEDOT:PSS-Ink

Single Walled Carbon Nanotubes (SWCNT) and conducting polymer PEDOT:PSS are the most promising materials among all to fabricate printable transparent and highly conductive electrodes to compete with ITO on plastic not least due to the fact that they are mostly composed of carbon – one of the most abundant and environmentally friendly elements.

PEDOT:PSS - and SWCNT-coatings can be highly conductive at the transparency >75% comparable to that of ITO on Polyethylene-therephthalate (PET). But there are still problems of thermal and UV-stability of PEDOT:PSS and the dispersing of SWCNT in a suitable solvent.

It is difficult to process films from pure SWCNTs. PEDOT:PSS is highly hydrophilic and can be dissolved in common solvents which in turn determine conductivity of films produced thereof. It is known that the addition of high boiling point solvents such as Ethylene Glycol (EG) or Dimethylsulfoxide (DMSO) boosts the conductivity of PEDOT:PSS films up to several orders of magnitude [149]. Therefore a suitable mixture of the solvents has to be found to ensure: i) the highest conductivity of the film and ii) the best rheological properties to produce a homogeneous wetting of the substrate.

Unmodified SWCNTs become well dispersed in solutions of PEDOT:PSS as it is evidenced by optical imaging of the SWCNT/PEDOT:PSS-dispersion (Fig. 5.22). The dispersion is stable for at least three month without any noticeable appearance of agglomerates even after three month. TEM-imaging (Fig. 5.22b-d) of the SWCNT/PEDOT:PSS-dispersion reveals a large content of SWCNTs, in particular bundles of SWCNTs, in the dispersion as it can be concluded through the presence of rigid rod-like tubular structures with uniform and sharp diameter, which are typically for the CNTs.

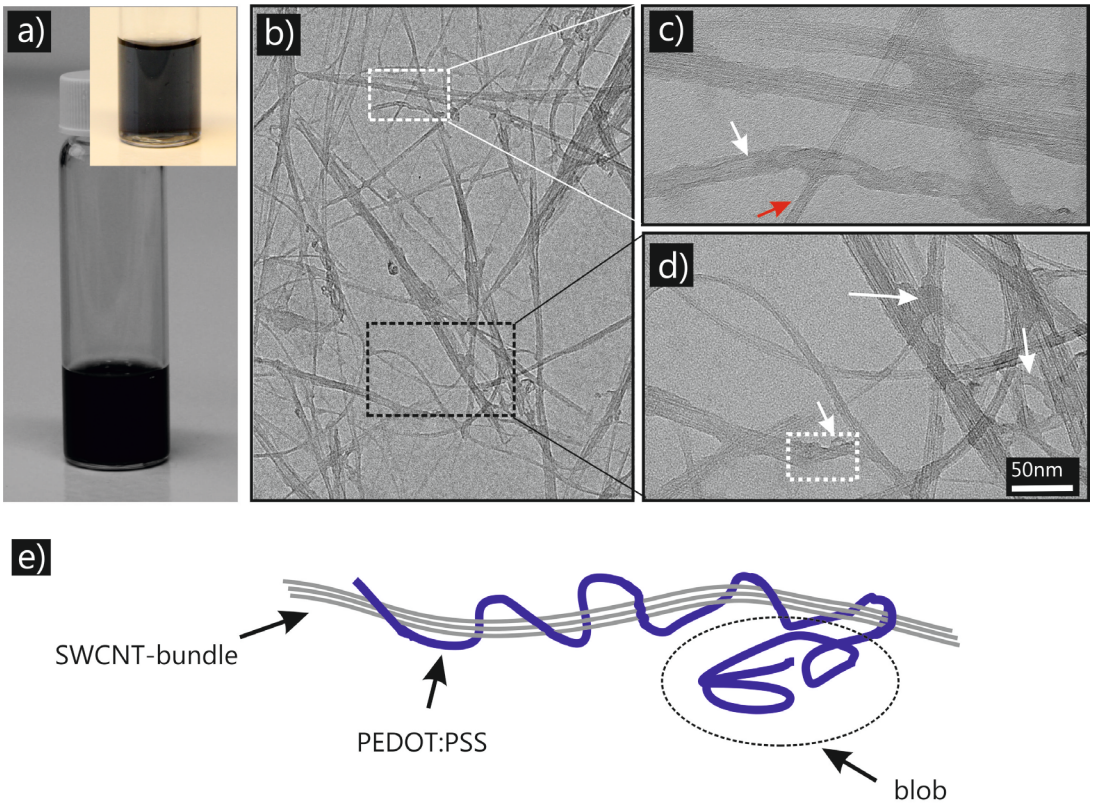

Fig. 5.22: Optical image of dispersion as prepared (a) and diluted five times (inset). TEM – images of SWCNT/PEDOT:PSS films (b-d). Dashed frames in (b) highlight the zoom-in areas presented in (c) (black dashed frame) and (d) (white dashed frame in (a)). White arrows emphasize the regions of SWCNTs which are enwrapped by PEDOT:PSS, red arrow highlights the SWCNT, which has uniform diameter and is therefore not enwrapped. White dashed frame in (d) highlights the region of the SWCNT bundle which is wrapped by PEDOT:PSS as it is demonstrated in (e).

One can also conclude that PEDOT:PSS is also present in the dispersion by analyzing the surrounding area of the SWCNT-bundles. There are regions of SWCNT-bundles, which are amorphous and exhibit variable diameter (Fig. 5.22c, white arrow and Fig. 5.22d, white arrows and white dashed rectangle). This is attributed to wrapping of SWCNT-bundles by PEDOT:PSS. The structure of unwrapped SWCNT-bundles with uniform diameter is highlighted in figure 5.22c with red arrow. The latter implies that PEDOT:PSS wraps the SWCNT-bundles leading to amorphous features around the SWCNT-bundles and modifies the sharp tubular structure of the SWCNT-bundles. At some place one can identify blobs around the SWCNT-bundles (Fig. 5.22d, white dashed rectangle). The model of enwrapping-phenomenon [150] of SWCNT-bundles by PEDOT:PSS is depicted in figure 5.22e.

The resulting thin films from SWCNT/PEDOT:PSS-ink are highly homogeneous, transparent an smooth as it is displayed in figure 5.23. The SFM-imaging reveals that the films are smooth (Fig. 5.23b,c). The films are stable at ambient – I could not detect any variation of resistance, homogeneity and optical transparency during at least 3 months. Also bending of the film on PE, PET and PETG substrates down to the bending radius of 5mm didn't cause any noticeable change of their sheet resistance.

The films are thermally stable: annealing up to 400°C did not have any noticeable effect on the resistance, and optical properties. Annealing of PEDOT:PSS thick films at 400°C makes the films insulating, while the mixed films remain highly conductive (no noticeable change in sheet resistance) even after thermal annealing at 400°C for 5minutes. For thin films at 80% transmittance the sheet resistance increased 3 times after annealing at 400 °C for 5 minutes.

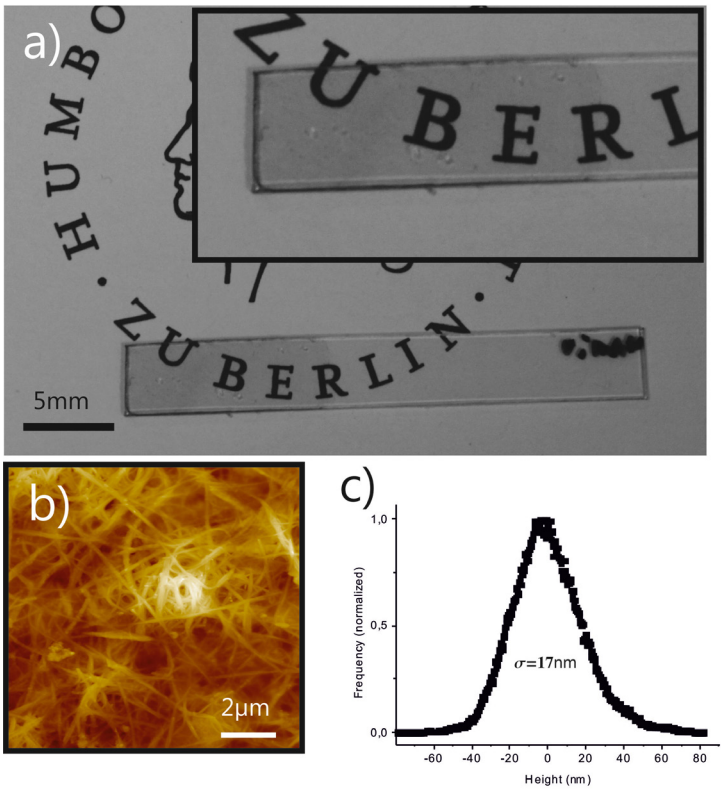

Fig. 5.23: Optical image of SWCNT/PEDOT:PSS – film on Polyethylene terephthalate glycol-modified (PET-G) (a) at transmittance of 95% and sheet resistance of 600 Ohm/Sq. SFM-image of SWCNT/PEDOT:PSS - films (c) on PET-G. Corresponding height with the standard deviations (σ) taken from the Gaussian fits of the histogram. The roughness of the film was estimated from the standard deviation of the fit.

The films are highly electrically conductive at high transparencies (for example: sheet resistance less than 600 Ω/square at 94% and less than 200 Ω/square at 80% transparency) (Fig. 5.24).

The sheet resistance R_s and transmittance T(λ), measured at a wavelength of 550 nm in TCFs, were related by:

$$T(\lambda) = (1 + \frac{188.5}{R_S}\frac{\sigma_{op}}{\sigma_{DC}})^{-2} \quad (5.1)$$

with characteristic σ_{DC} and optical σ_{op} conductivity of the film. The properties of TCFs with different R_s and T values could be compared using the ratio σ_{op} / σ_{DC} as the figure-of-merit [55, 151], which are typically used to qualify transparent and conducting films.

The σ_{op} / σ_{DC} value could be obtained from the slope of $T^{\frac{1}{2}}/(1-T^{\frac{1}{2}})$ versus the R_s plot, as derived from Eq. 5.1. The higher this value the better is the performance of the films. I obtained the value of σ_{op} / σ_{DC} to 28±1, which is comparable to that reported in [57]. However films prepared in that paper were treated with gold-ions and prepared in more complicated way than the films presented in this work.

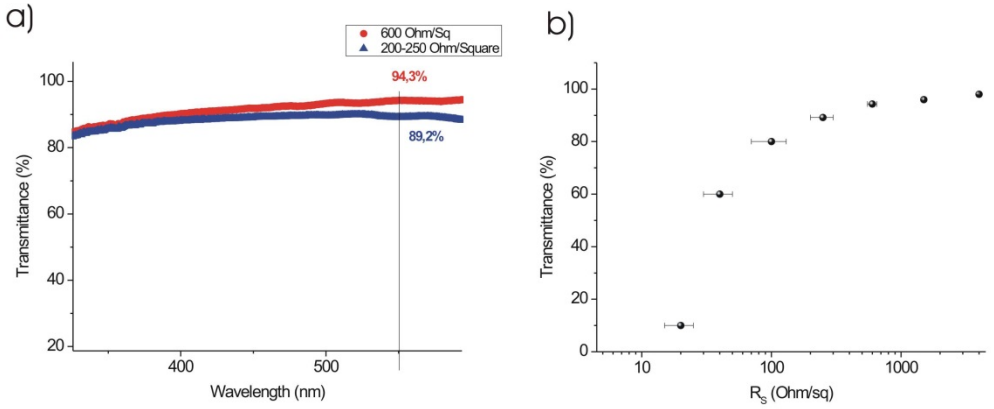

Fig. 5.24: UV-spectra of the SWCNT-PEDOT:PSS-films (a) at different transmittance on PETG. Transmittance versus sheet resistance of the SWCNT/PEDOT:PSS-films (b).

The method described in this section allows using common solvents including the solvents with low boiling points. Thus, no annealing at high temperatures is required to remove the solvent from the film. This makes the solutions described in this work suitable for printing on common flexible plastic substrates, since common plastic substrates have

the glass transition temperature in the range of 100-120°C and thus cannot be annealed. The most closely related inks use modified SWCNT [152, 153]. Films produced thereof either must be additionally processed, resulting in an increased costs accompanied with increasing complexity of the fabrication process, or the process of modification itself requires aggressive acids. As it has been discussed above amphiphile molecules and polymeric binders worsen electrical conductivity of the resulting films, which the method presented in this section overcomes.

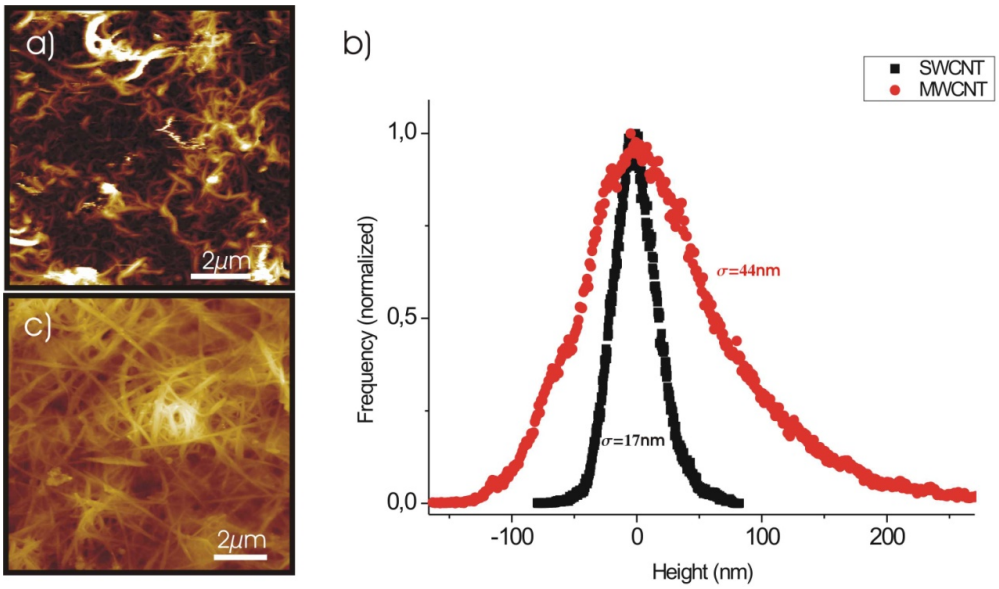

Fig. 5.25: SFM-images of MWCNT- (a) and SWCNT/PEDOT:PSS - films (c) on PETG. Corresponding height histograms (b) for SWCNT (black squares) and MWCNT (red circles) with the standard deviations (sigma) taken from the Gaussian fits of the histograms. The roughness of the films was estimated from the standard deviations of the fits.

Furthermore, it can be envisioned that PEDOT:PSS should stabilize the structure of a PEDOT:PSS-SWCNT film, i.e. the film is more homogeneous and stable. Higher homogeneity of the film can be attributed to enwrapping [150] of SWCNTs by PEDOT:PSS. This is supported by TEM imaging (Fig. 5.22). An essential advantage of my conducting transparent SWCNT-films is that they are much smoother (Fig. 5.25) than the films made from MWCNT. The latter point is crucial for fabricating light-emitting devices. Also the combination PEDOT:PSS with SWCNTs introduces a new component in printed electronics – “conductive binder”, which has superior electrical and mechanical properties and can potentially replace conventional binders consisting of insulating polymers. The role of

conducting binder has been demonstrated in the patent application (AKZ 102013225908.5). It has been demonstrated that combination of SWCNT and PEDOT:PSS in combination with silver- flakes and nanoparticles is very promising for fabrication of highly conductive and flexible films with a sheet resistance of <1Ohm without thermal annealing at temperatures above 100° C. These films can be applied also in flexible electronics where very low resistances are required, for instance for printing of electronic IC-boards.

5.4.6 GO-based inks

Conductive inks which can be used to produce coatings on different substrates is of high technological interest in the industry in applications like antistatic coatings, thermally dissipative coatings, electromagnetic shielding [154], fabrication of sensors [155]. Fabrication of field effect transistors has been demonstrated [156].

Currently there are different types of conductive inks available which are mostly either silver based or carbon based. Although the silver based inks can be used to produce films exhibiting superior conductivity to compare with other types of inks, they are more expensive to produce due to the price of the silver. They have a limited shelf life, (due to sedimentation of silver particles). Films made from silver containing inks require typically annealing at high temperatures and sintering. Moreover the films made of those inks are fragile. This makes them to be not well suitable for flexible electronic applications. Mechanical flexibilities of films produced with commercial silver based inks depend on the ratio of the binder and silver particles, wherein the binder content serves as film-forming agent and needs to be removed to make the films conductive. Usually ratio of silver particles to binder is high in order to maintain good conductivity of ink which in turn reduces flexibility introduced by binder.

Carbon based inks are cheaper and films made thereof are more robust than their silver analogues. Typically, carbon black is used as the filler in such inks. However the conductivities of carbon black based films are at least two orders of magnitude lower than of silver films and the films must be annealed at temperatures >150° as well if a polymeric binder is used.

The use of conductive polymers like PEDOT:PSS as a binder has been demonstrated [157, 158]. The films show good conductivity as well as good film forming properties. However the amount of PEDOT:PSS used in these films was large which is not cost-efficient. Polymeric binders are usually used to ensure sufficient film forming properties, i. e. to produce homogeneous films and make them less fragile. The polymeric binders such as PVP, Ethyl Cellulose are insulators, thus adding them to graphene dispersions

results in good film forming properties but also reduction of conductivity of the films by several orders of magnitude.

Graphenes, CNTs and graphene oxide (GO) have recently become the objects of increased interest for variable technological applications. Graphene have high: electrical conductivity, thermal conductivity, barrier properties and mechanical strength, also high thermal conductivity which then introduces new applications such as efficient heat sinks [159]. It has been shown also that graphite flakes can be exfoliated to graphenes and dispersed in variable solvents. But graphene solutions processed this way are low concentrated and therefore not suitable for printing on substrates due to insufficient film forming properties. The films produced from graphene solutions exhibit low conductivity comparable to Chemical Vapor Deposited (CVD) graphenes.

Films produced from CNTs can be highly conductive. However it is difficult to process films from CNTs without using surfactants or chemically treating them in highly aggressive acids. Recently it was shown that pure CNTs can be dissolved in solutions containing graphene oxides [160]. However, due to the insulating nature of GO these films show pure conductivity. There is a need of new conductive inks addressing the drawbacks listed above.

Drop-casted inks of two different dispersions on glass (ultrasonicated in Ethanol for 10 minutes) are presented in figure 5.26a, with a drop of GO-based-ink (Fig. 5.26a left) and PEDOT:PSS-dispersion (Fig. 5.26a right). Visual inspection suggests that the contact angle of the drop corresponding to the GO-based-ink is substantially smaller than that of the drop of PEDOT:PSS-dispersion.

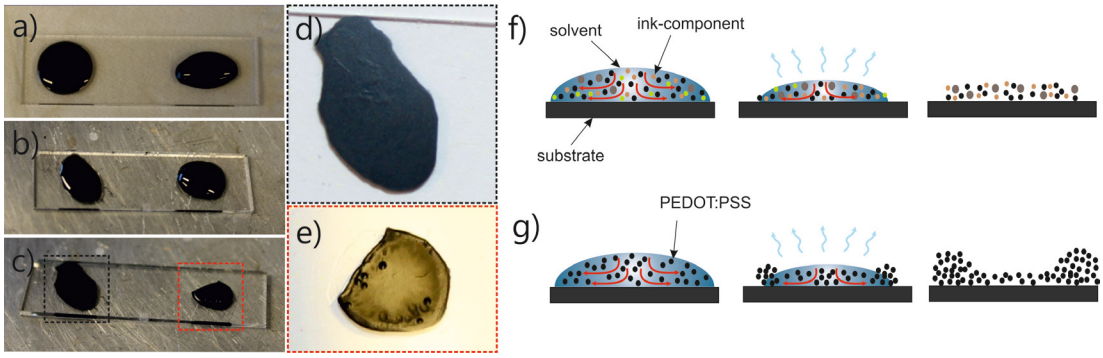

Fig. 5.26: Optical images of drop-casted wet films of GO-based-ink and PEDOT:PSS-dispersion on glass (a). Optical image of the films after 30 seconds drying on a heating plate at 90° C (b) and the image dry films (c). Zoom-in areas of the regions in (c) framed with black and red dashed square (d) highlighting the dry films of GO-based-ink and PEDOT:PSS-dispersion respectively. Model representing drying process without (f) and with coffee-stain-effect (g). The drying time in (f) and (g) scales from left to right.

This observation implies better wetting of the glass substrate by GO-based-ink. Upon drying at 90°C on the heating plate the lateral shape of the drops changes and the drop becomes smaller implying that the evaporation of the volatile solvents occurs. This observation is displayed in figure 5.26b, after 30 seconds drying. 10 minutes after drying the volatile solvents are evaporated completely and only the solid particles that are pinned to the glass substrate remain (Fig. 5.26c). Noticeable is that the shape of dried films differs completely from the shape of initial drops. Also the shape of dried film of GO-based-ink and of PEDOT:PSS-dispersion are different. The dry film of PEDOT:PSS-dispersion (Fig. 5.26e) exhibits a pronounced “coffee-stain-effect” [110], which is schematically depicted in figure 5.26g.

During drying, drop edges become pinned to the substrate, and capillary flow outward from the center of the drop brings suspended particles in the dispersion to the edge as evaporation proceeds. After evaporation, suspended particles are left highly concentrated along the original drop edge [110]. The dry films of GO-based-ink were highly conductive and exhibited a resistance of 20±2 Ω/Sq, which didn’t change after annealing of the films at 400°C for ten minutes. The dry PEDOT:PSS films exhibited the same resistance but thermal annealing at 400° C even for five minutes made the films insulating. To test mechanical flexibility, the films of GO-based inks on PET were bent down to the bending radius of 5mm. The resistivity of the films didn’t noticeably changed even after bending which suggests high mechanical flexibility of the films.

The shape of the dry film of the GO-based-ink is almost uniform, in particular at the edges. Interestingly, that no coffee-stain-effect is observed with the dry film of GO-based-ink and this film is more uniform. This finding implies that the suspended particles are pinned to the substrate more uniformly and the capillary flow from the center of the drop doesn't so strongly as in case of PEDOT:PSS-dispersion. This effect could be explained through the stronger interactions between the particles within the drop of the ink as well as the anisotropic shape of the particles, which produces strong capillary interactions between the particles [110, 161-164]. Note that this capillary interaction has been characterized in prior experiments as long-ranged and very strong [110, 163, 165-167]. It is also possible the GO facilitates the pinning of the contact line and freezes all the particles so that they in turn cannot be transported to the edges of the drop by the capillary flow, which leads to the elimination of the coffee-stain-effect. It has been reported that films containing GO can suppress the coffee-ring-effect [168]. Noteworthy is that such homogeneous film formation of the GO-based-ink as depicted in figure 5.25d was observed only if all of the components (MWCNT, PEDOT:PSS, Graphite and GO) were included in the ink.

In conclusion the ink formulation based on GO was fabricated. Dry film produced from the ink were homogeneous and didn't exhibit a coffee-stain-effect as the films made from PEDOT:PSS. The films exhibited a sheet resistance of 20±2 Ω/Sq and were thermally stable up to 400°C without any noticeable change in sheet resistance. High mechanical flexibility make makes the film to promising candidate for flexible electronic applications.

6. Summary and Outlook

The aim of this work was to investigate the electronic properties of graphenes with the focus on graphene-substrate electronic interaction in the first part and fabricate carbon-based transparent and electrodes for flexible electronics applications in the second part.

The electronic properties of graphene were investigated providing new insights into electrostatic screening properties of graphene on mica and revealing exponential dependence of surface potential of graphene on graphene layer number. Doping of graphene by confined water layers was investigated, providing experimental evidences for p-doping of graphene by confined water layers, with the magnitude of doping depending on the thickness of water layers. This demonstrates dependence of graphene doping on the thickness of water layers.

It was shown that covering of dendronized polymers, of different generations, on mica by graphene is a method to locally control the deformation of graphene and thereby design strain engineered electronic devices.

Novel type of conducting printable inks was developed and the transparent electrodes made thereof were fabricated and characterized. Transparent electrodes based on graphene and MWCNT were fabricated. Chemically exfoliated graphenes has been shown to disperse the MWCNTs acting as dispersing agent.

Transparent electrodes based on SWCNT exhibited superior properties than the state of the art. Moreover these inks were optimized for large area industrially relevant applications. The transparent electrodes prepared by dip-coating from the SWCNT-based inks are flexible and optimized that only one printing step is required to obtain sufficient characteristics of the electrode. An essential advantage of conducting transparent films based on SWCNT instead of MWCNT is that they are much smoother than the films made from MWCNT. The latter point is crucial for fabricating light-emitting devices.

A method to improve the film forming properties of conducting inks was found which is based on special combination of the solvents without using of any additives

which is an obvious technological advantage for the printed electronics industry. Graphene Oxide based ink was developed which exhibits a sheet resistance of 20 Ω/Sq and overcomes the “Coffee Stain (ring)” effect, which is of great technological importance since the Coffee stain effect cause problems in printing industry. This ink could be applicable for ink-jet of screen printing methods to print homogeneous conducing films or traces on flexible substrates.

It is noteworthy to mention that the inks can be used to fully print Organic Light-Emitting devices where the SWCNT-ink can serve as transparent anode and the GO-ink as cathode.

As outlook for the first part of the work, further investigations on the structure of confined water using STM could provide more insight to the electronic structure of graphene confining water layers. It is also of interest to find a method to manipulate the structure of confined water and probe *in-situ* electronic properties of graphene. The EFM-Method has been shown to be a promising tool for studying of electronic properties of graphene at the nanoscale and it could be extended to the other classes of molecules, which can be confined by graphene. It would be interesting to get insight of surface potential modulation of graphene covering dendronized polymers using the EFM. Raman spectroscopy of graphene covering dendronized polymers could provide insight the doping of graphene by dendronized polmyers or quantify strain. The Conductive AFM could provide means to probe electrical current of graphene which structure is modified by the denpols.

It is envisioned to fabricate fully printed Organic Light Emitting Devices (OLED) or Organic Solar Cells (OCS) from the inks that were invented in this work. Up to today there is a number of light-emitting polymers or small molecules that can be solution processed and therefore incorporated into the electronic devices. The next step would be the design of fully printed flexible OLED based display.

7. Bibliography

1. Dean, C.R., et al., *Boron nitride substrates for high-quality graphene electronics.* Nat Nano, 2010. **5**(10): p. 722-726.
2. Liu, Z., A.A. Bol, and W. Haensch, *Large-Scale Graphene Transistors with Enhanced Performance and Reliability Based on Interface Engineering by Phenylsilane Self-Assembled Monolayers.* Nano Letters, 2010. **11**(2): p. 523-528.
3. Bolotin, K.I., et al., *Ultrahigh electron mobility in suspended graphene.* Solid State Communications, 2008. **146**(9–10): p. 351-355.
4. Goncher, S.J., et al., *Substrate Level Control of the Local Doping in Graphene.* Nano Letters, 2013. **13**(4): p. 1386-1392.
5. Ponomarenko, L.A., et al., *Effect of a High-κ Environment on Charge Carrier Mobility in Graphene.* Physical Review Letters, 2009. **102**(20): p. 206603.
6. Shim, J., et al., *Water-Gated Charge Doping of Graphene Induced by Mica Substrates.* Nano Letters, 2012. **12**(2): p. 648-654.
7. Lin, S.S., et al., *Unintentional doping induced splitting of G peak in bilayer graphene.* Applied Physics Letters, 2011. **99**(23): p. 233110.
8. Aitken, Z.H. and R. Huang, *Effects of mismatch strain and substrate surface corrugation on morphology of supported monolayer graphene.* Journal of Applied Physics, 2010. **107**(12): p. 123531.
9. Neek-Amal, M. and F.M. Peeters, *Strain-engineered graphene through a nanostructured substrate. I. Deformations.* Physical Review B, 2012. **85**(19): p. 195445.
10. Berger, C., et al., *Electronic Confinement and Coherence in Patterned Epitaxial Graphene.* Science, 2006. **312**(5777): p. 1191-1196.
11. Marchini, S., S. Günther, and J. Wintterlin, *Scanning tunneling microscopy of graphene on Ru(0001).* Physical Review B, 2007. **76**(7): p. 075429.
12. Sutter, P.W., J.-I. Flege, and E.A. Sutter, *Epitaxial graphene on ruthenium.* Nat Mater, 2008. **7**(5): p. 406-411.
13. Vázquez de Parga, A.L., et al., *Periodically Rippled Graphene: Growth and Spatially Resolved Electronic Structure.* Physical Review Letters, 2008. **100**(5): p. 056807.
14. Coraux, J., et al., *Structural Coherency of Graphene on Ir(111).* Nano Letters, 2008. **8**(2): p. 565-570.
15. Ishigami, M., et al., *Atomic Structure of Graphene on SiO2.* Nano Letters, 2007. **7**(6): p. 1643-1648.
16. Stolyarova, E., et al., *High-resolution scanning tunneling microscopy imaging of mesoscopic graphene sheets on an insulating surface.* Proceedings of the National Academy of Sciences, 2007. **104**(22): p. 9209-9212.
17. Geringer, V., et al., *Intrinsic and extrinsic corrugation of monolayer graphene deposited on SiO_2.* Physical Review Letters, 2009. **102**(7): p. 076102.

18. Ghosh, D.S., *Ultrathin Metal Transparent Electrodes for the Optoelectronics Industry*. 2013: Springer.

19. Jo, J.W., et al., *Fabrication of Highly Conductive and Transparent Thin Films from Single-Walled Carbon Nanotubes Using a New Non-ionic Surfactant via Spin Coating.* Acs Nano, 2010. **4**(9): p. 5382-5388.

20. Vilcakova, J., et al., *Effect of Surfactants and Manufacturing Methods on the Electrical and Thermal Conductivity of Carbon Nanotube/Silicone Composites.* Molecules, 2012. **17**(11): p. 13157-13174.

21. Wang, J.P., et al., *Removal of the Residual Surfactants in Transparent and Conductive Single-Walled Carbon Nanotube Films.* Journal of Physical Chemistry C, 2009. **113**(41): p. 17685-17690.

22. Hernandez, Y., et al., *High-yield production of graphene by liquid-phase exfoliation of graphite.* Nature Nanotechnology, 2008. **3**(9): p. 563-568.

23. AG, B.M., *Dispersions containing carbon nanotubes and graphene platelets*, 2013.

24. Faircloth, T.J., J.G. Innocenzo, and C.D. Lang, *43.3: Slot Die Coating for OLED Displays.* SID Symposium Digest of Technical Papers, 2008. **39**(1): p. 645-647.

25. Yang, C., C.P. Wong, and M.M.F. Yuen, *Printed electrically conductive composites: conductive filler designs and surface engineering.* Journal of Materials Chemistry C, 2013. **1**(26): p. 4052-4069.

26. Huang, L., et al., *Graphene-based conducting inks for direct inkjet printing of flexible conductive patterns and their applications in electric circuits and chemical sensors.* Nano Research, 2011. **4**(7): p. 675-684.

27. Hast, J., et al., *18.1: Invited Paper: Roll-to-Roll Manufacturing of Printed OLEDs.* SID Symposium Digest of Technical Papers, 2013. **44**(1): p. 192-195.

28. Castro Neto, A.H., et al., *The electronic properties of graphene.* Reviews of Modern Physics, 2009. **81**(1): p. 109-162.

29. Andrei, E.Y., G. Li, and X. Du, *Electronic properties of graphene: a perspective from scanning tunneling microscopy and magnetotransport.* Reports on Progress in Physics, 2012. **75**(5).

30. Wallace, P.R., *The Band Theory of Graphite.* Physical Review, 1947. **71**(9): p. 622-634.

31. Zeitler, U., J. Giesbers, and J.-K. Maan, *Quanten-Hall-Effekt in Graphen. Ein- und doppellagiges Graphen im Magnetfeld.* Physik in unserer Zeit, 2009. **40**(3): p. 124-131.

32. Saito, R., G. Dresselhaus, and M.S. Dresselhaus, *Physical Properties of Carbon Nanotube*. 1998: Imperial College Press.

33. Mak, K.F., et al., *Optical spectroscopy of graphene: From the far infrared to the ultraviolet.* Solid State Communications, 2012. **152**(15): p. 1341-1349.

34. Novoselov, K.S., et al., *Two-dimensional gas of massless Dirac fermions in graphene.* Nature, 2005. **438**(7065): p. 197-200.

35. Moreira, L.M., *Raman spectroscopy of graphene: probing phonons, electrons and electron-phonon interactions*, 2009, Universidade Federal de Minas Gerais.

36. Hasegawa, M. and K. Nishidate, *Transfer doping of a metallic carbon nanotube and graphene on metal surfaces.* Physical Review B, 2011. **83**(15): p. 155435.

37. Bhattacharya, P., S. Mahajan, and H. Kamimura, *Comprehensive Semiconductor Science and Technology: Online version*. 2011: Elsevier Science.

38. *Polymer Interface and Adhesion*. 1982: Taylor & Francis.

39. Gusynin, V.P., S.G. Sharapov, and J.P. Carbotte, *Unusual Microwave Response of Dirac Quasiparticles in Graphene.* Physical Review Letters, 2006. **96**(25): p. 256802.

40. Mak, K.F., et al., *Measurement of the Optical Conductivity of Graphene.* Physical Review Letters, 2008. **101**(19): p. 196405.

41. Dorn, M., et al., *High contrast optical detection of single graphenes on optically transparent substrates.* Journal of Applied Physics, 2010. **108**(10): p. -.

42. Rezania, B., et al., *Influence of graphene exfoliation on the properties of water-containing adlayers visualized by graphenes and scanning force microscopy.* Journal of Colloid and Interface Science, 2013. **407**(0): p. 500-504.

43. Jiang, D.E., *Graphene Chemistry: Theoretical Perspectives*. 2013: John Wiley & Sons.

44. Chen, W., et al., *Surface transfer doping of semiconductors.* Progress in Surface Science, 2009. **84**(9–10): p. 279-321.

45. Ristein, J., *Surface Transfer Doping of Semiconductors.* Science, 2006. **313**(5790): p. 1057-1058.

46. Strobel, P., et al., *Surface transfer doping of diamond.* Nature, 2004. **430**(6998): p. 439-441.

47. Yan, J., et al., *Electric Field Effect Tuning of Electron-Phonon Coupling in Graphene.* Physical Review Letters, 2007. **98**(16): p. 166802.

48. Wang, R., et al., *Control of Carrier Type and Density in Exfoliated Graphene by Interface Engineering.* Acs Nano, 2011. **5**(1): p. 408-412.

49. Shi, Y.M., et al., *Effective doping of single-layer graphene from underlying SiO(2) substrates.* Physical Review B, 2009. **79**(11).

50. Pisana, S., et al., *Breakdown of the adiabatic Born-Oppenheimer approximation in graphene.* Nat Mater, 2007. **6**(3): p. 198-201.

51. Casiraghi, C., et al., *Raman fingerprint of charged impurities in graphene.* Applied Physics Letters, 2007. **91**(23).

52. Popov, V.N. and P. Lambin, *Dynamic and charge doping effects on the phonon dispersion of graphene.* Physical Review B, 2010. **82**(4): p. 045406.

53. Israelachvili, J.N., *Intermolecular and Surface Forces*. 2010: Elsevier Science.

54. Wang, S. and L. Jiang, *Definition of Superhydrophobic States.* Advanced Materials, 2007. **19**(21): p. 3423-3424.

55. Jung, H., et al., *A scalable fabrication of highly transparent and conductive thin films using fluorosurfactant-assisted single-walled carbon nanotube dispersions.* Carbon, 2013. **52**(0): p. 259-266.

56. Dan, B., G.C. Irvin, and M. Pasquali, *Continuous and Scalable Fabrication of Transparent Conducting Carbon Nanotube Films.* Acs Nano, 2009. **3**(4): p. 835-843.

57. Vazquez, G., E. Alvarez, and J.M. Navaza, *Surface Tension of Alcohol Water + Water from 20 to 50 .degree.C.* Journal of Chemical & Engineering Data, 1995. **40**(3): p. 611-614.

58. Tadros, T.F., *Rheology of Dispersions: Principles and Applications*. 2011: Wiley.

59. Rosen, M.J., *Surfactants and Interfacial Phenomena*. 2004: Wiley.

60. Shvartzman-Cohen, R., et al., *Selective Dispersion of Single-Walled Carbon Nanotubes in the Presence of Polymers: the Role of Molecular and Colloidal Length Scales.* Journal of the American Chemical Society, 2004. **126**(45): p. 14850-14857.

61. Sakka, S., *Handbook of sol-gel science and technology. 1. Sol-gel processing*. 2005: Kluwer Academic Publishers.

62. Lee, H., R. Pober, and P. Calvert, *Dispersion of powders in solutions of a block copolymer.* Journal of Colloid and Interface Science, 1986. **110**(1): p. 144-148.

63. Palla, B.J., *Mixed surfactant systems to control dispersion stability in severe environments for enhancing chemical mechanical polishing (CMP) of metal surfaces*, 2000, UNIVERSITY OF FLORIDA.

64. Skotheim, T.A., *Handbook of Conducting Polymers, Second Edition*. 1997: Taylor & Francis.

65. Napper, D.H., *Steric stabilization and the Hofmeister series.* Journal of Colloid and Interface Science, 1970. **33**(3): p. 384-392.

66. Smitham, J.B. and D.H. Napper, *Steric stabilization in worse thanθ-solvents.* Colloid and Polymer Science, 1979. **257**(7): p. 748-756.

67. Grosberg, A.I.U. and A.R. Khokhlov, *Statistical*. 1994: Springer-Verlag GmbH.

68. Flory, P.J., *Principles of Polymer Chemistry*. 1953: Cornell University Press.

69. Russel, W.B., D.A. Saville, and W.R. Schowalter, *Colloidal Dispersions*. 1992: Cambridge University Press.

70. Rudenko, A.N., et al., *Graphene adhesion on mica: Role of surface morphology.* Physical Review B, 2011. **83**(4): p. 045409.

71. Fleet, E., *Rock-forming Minerals: Micas. Volume 3A*. 2003: Geological Society.

72. Lui, C.H., et al., *Ultraflat graphene.* Nature, 2009. **462**(7271): p. 339-341.

73. Severin, N., et al., *Reversible Dewetting of a Molecularly Thin Fluid Water Film in a Soft Graphene–Mica Slit Pore.* Nano Letters, 2012. **12**(2): p. 774-779.

74. Popov, V.N., *Carbon nanotubes: properties and application.* Materials Science and Engineering: R: Reports, 2004. **43**(3): p. 61-102.

75. Kayatin, M., *RHEOLOGY, STRUCTURE, AND STABILITY OF CARBON NANOTUBE – UNSATURATED POLYESTER RESIN DISPERSIONS*, 2008, Auburn University.

76. Iijima, S., *Carbon nanotubes: past, present, and future.* Physica B: Condensed Matter, 2002. **323**(1–4): p. 1-5.

77. Kim, J., et al., *Graphene Oxide Sheets at Interfaces.* Journal of the American Chemical Society, 2010. **132**(23): p. 8180-8186.

78. Hummers, W.S. and R.E. Offeman, *Preparation of Graphitic Oxide.* Journal of the American Chemical Society, 1958. **80**(6): p. 1339-1339.

79. Lerf, A., et al., *Structure of Graphite Oxide Revisited‖.* The Journal of Physical Chemistry B, 1998. **102**(23): p. 4477-4482.

80. Li, D. and R.B. Kaner, *Graphene-Based Materials.* Science, 2008. **320**(5880): p. 1170-1171.

81. Li, D., et al., *Processable aqueous dispersions of graphene nanosheets.* Nat Nano, 2008. **3**(2): p. 101-105.

82. Park, S. and R.S. Ruoff, *Chemical methods for the production of graphenes.* Nat Nano, 2009. **4**(4): p. 217-224.

83. Nakajima, T. and Y. Matsuo, *Formation process and structure of graphite oxide.* Carbon, 1994. **32**(3): p. 469-475.

84. Gómez-Navarro, C., et al., *Electronic Transport Properties of Individual Chemically Reduced Graphene Oxide Sheets.* Nano Letters, 2007. **7**(11): p. 3499-3503.

85. Stankovich, S., et al., *Stable aqueous dispersions of graphitic nanoplatelets via the reduction of exfoliated graphite oxide in the presence of poly(sodium 4-styrenesulfonate).* Journal of Materials Chemistry, 2006. **16**(2): p. 155-158.

86. Stankovich, S., et al., *Synthesis of graphene-based nanosheets via chemical reduction of exfoliated graphite oxide.* Carbon, 2007. **45**(7): p. 1558-1565.

87. Salzmann, I., *Structural and energetic properties of pentacene derivatives and heterostructures*, 2009, Mathematisch-Naturwissenschaftliche Fakultät I.

88. Koch, N., A. Vollmer, and A. Elschner, *Influence of water on the work function of conducting poly(3,4-ethylenedioxythiophene)/poly(styrenesulfonate).* Applied Physics Letters, 2007. **90**(4): p. -.

89. Kirchmeyer, S. and K. Reuter, *Scientific importance, properties and growing applications of poly(3,4-ethylenedioxythiophene).* Journal of Materials Chemistry, 2005. **15**(21): p. 2077-2088.

90. Meyer, E., H.J. Hug, and R. Bennewitz, *Scanning Probe Microscopy: The Lab on a Tip*. 2004: Springer.

91. Wiesendanger, R., *Scanning Probe Microscopy and Spectroscopy: Methods and Applications*. 1994: Cambridge University Press.

92. Zhong, Q., et al., *Fractured polymer/silica fiber surface studied by tapping mode atomic force microscopy.* Surface Science, 1993. **290**(1–2): p. L688-L692.

93. García, R. and R. Pérez, *Dynamic atomic force microscopy methods.* Surface Science Reports, 2002. **47**(6–8): p. 197-301.

94. Ziegler, D., et al., *Variations in the work function of doped single- and few-layer graphene assessed by Kelvin probe force microscopy and density functional theory.* Physical Review B, 2011. **83**(23): p. 235434.

95. Yu, Y.-J., et al., *Tuning the Graphene Work Function by Electric Field Effect.* Nano Letters, 2009. **9**(10): p. 3430-3434.

96. Datta, S.S., et al., *Surface Potentials and Layer Charge Distributions in Few-Layer Graphene Films.* Nano Letters, 2009. **9**(1): p. 7-11.

97. Panchal, V., et al., *Standardization of surface potential measurements of graphene domains.* Sci. Rep., 2013. **3**.

98. Burnett, T., R. Yakimova, and O. Kazakova, *Mapping of Local Electrical Properties in Epitaxial Graphene Using Electrostatic Force Microscopy.* Nano Letters, 2011. **11**(6): p. 2324-2328.

99. Staii, C., A.T. Johnson, and N.J. Pinto, *Quantitative analysis of scanning conductance microscopy.* Nano Letters, 2004. **4**(5): p. 859-862.

100. Bockrath, M., et al., *Scanned conductance microscopy of carbon nanotubes and lambda-DNA.* Nano Letters, 2002. **2**(3): p. 187-190.

101. Ellison, D.J., et al., *Surface Potential Mapping of SAM-Functionalized Organic Semiconductors by Kelvin Probe Force Microscopy.* Advanced Materials, 2011. **23**(4): p. 502-507.

102. Braun, S., W.R. Salaneck, and M. Fahlman, *Energy-Level Alignment at Organic/Metal and Organic/Organic Interfaces.* Advanced Materials, 2009. **21**(14-15): p. 1450-1472.

103. Smoluchowski, R., *Anisotropy of the Electronic Work Function of Metals.* Physical Review, 1941. **60**(9): p. 661-674.

104. Bagus, P.S., et al., *Work Function Changes Induced by Charged Adsorbates: Origin of the Polarity Asymmetry.* Physical Review Letters, 2008. **100**(12): p. 126101.

105. Schumm, M., *ZnO-based Semiconductors Studied by Raman Spectroscopy: Semimagnetic Alloying, Doping, and Nanostructures*. 2009.

106. Ado Jorio, M.S.D., Riichiro Saito, Gene Dresselhaus *Raman Spectroscopy in Graphene Related Systems*. 2011.

107. Atkins, P., J. de Paula, and R. Friedman, *Physical Chemistry: Quanta, Matter, and Change*. 2013: OUP Oxford.

108. Wu, Y.H., T. Yu, and Z.X. Shen, *Two-dimensional carbon nanostructures: Fundamental properties, synthesis, characterization, and potential applications.* Journal of Applied Physics, 2010. **108**(7): p. -.

109. Wang, Q.H., et al., *Understanding and controlling the substrate effect on graphene electron-transfer chemistry via reactivity imprint lithography.* Nat Chem, 2012. **4**(9): p. 724-732.

110. Yunker, P.J., et al., *Suppression of the coffee-ring effect by shape-dependent capillary interactions.* Nature, 2011. **476**(7360): p. 308-311.

111. Schwierz, F., *Graphene transistors.* Nat Nano, 2010. **5**(7): p. 487-496.

112. Balandin, A.A., *Low-frequency 1/f noise in graphene devices.* Nat Nano, 2013. **8**(8): p. 549-555.

113. Stampfer, C., et al., *Raman imaging of doping domains in graphene on SiO(2).* Applied Physics Letters, 2007. **91**(24).

114. Castellanos-Gomez, A., et al., *Spatially resolved electronic inhomogeneities of graphene due to subsurface charges.* Carbon, 2012. **50**(3): p. 932-938.

115. Jones, G.J., et al., *Surface Potential Variations in Graphene Induced by Nanostructured Crystalline Ionic Substrates.* Applied Physics Express, 2012. **5**(4).

116. Shim, J., et al., *Water-Gated Charge Doping of Graphene Induced by Mica Substrates.* Nano Letters, 2012. **12**(2): p. 648-654.

117. Komurasaki, H., et al., *Layered Structures of Interfacial Water and Their Effects on Raman Spectra in Graphene-on-Sapphire Systems.* The Journal of Physical Chemistry C, 2012. **116**(18): p. 10084-10089.

118. Ohta, T., et al., *Interlayer Interaction and Electronic Screening in Multilayer Graphene Investigated with Angle-Resolved Photoemission Spectroscopy.* Physical Review Letters, 2007. **98**(20): p. 206802.

119. Vandewal, K., et al., *Efficient charge generation by relaxed charge-transfer states at organic interfaces.* Nat Mater, 2014. **13**(1): p. 63-68.

120. Koch, N., N. Ueno, and A.T.S. Wee, *The Molecule-Metal Interface*. 2013: Wiley.

121. Leenaerts, O., B. Partoens, and F.M. Peeters, *Water on graphene: Hydrophobicity and dipole moment using density functional theory.* Physical Review B, 2009. **79**(23): p. 235440.

122. Freitas, R.R.Q., et al., *DFT Studies of the Interactions of a Graphene Layer with Small Water Aggregates.* The Journal of Physical Chemistry A, 2011. **115**(44): p. 12348-12356.

123. Schedin, F., et al., Nat.Mater., 2007. **6**: p. 652.

124. Kimmel, G.A., et al., *No Confinement Needed: Observation of a Metastable Hydrophobic Wetting Two-Layer Ice on Graphene.* Journal of the American Chemical Society, 2009. **131**(35): p. 12838-12844.

125. Lee, J.E., et al., *Optical separation of mechanical strain from charge doping in graphene.* Nat Commun, 2012. **3**: p. 1024.

126. Li, X., et al., *Influence of water on the electronic structure of metal-supported graphene: Insights from van der Waals density functional theory.* Physical Review B, 2012. **85**(8): p. 085425.

127. Wehling, T.O., M.I. Katsnelson, and A.I. Lichtenstein, Chem.Phys.Lett., 2009. **476**: p. 125.

128. Xu, K., P. Cao, and J.R. Heath, *Graphene Visualizes the First Water Adlayers on Mica at Ambient Conditions.* Science, 2010. **329**(5996): p. 1188-1191.

129. Severin, N., et al., *Replication of Single Macromolecules with Graphene.* Nano Letters, 2011. **11**(6): p. 2436-2439.

130. Zhang, B., et al., *The Largest Synthetic Structure with Molecular Precision: Towards a Molecular Object.* Angewandte Chemie International Edition, 2011. **50**(3): p. 737-740.

131. Zhang, B., et al., *Height and Width of Adsorbed Dendronized Polymers: Electron and Atomic Force Microscopy of Homologous Series.* Macromolecules, 2011. **44**(17): p. 6785-6792.

132. Zhang, D.B., E. Akatyeva, and T. Dumitrică, *Bending Ultrathin Graphene at the Margins of Continuum Mechanics.* Physical Review Letters, 2011. **106**(25): p. 255503.

133. Lauer, M.E. and J.-H. Fuhrhop, *Porphyrinphosphonate Fibers on Mica and Molecular Rows on Graphite.* Langmuir, 2004. **20**(19): p. 8321-8328.

134. Stifter, T., O. Marti, and B. Bhushan, *Theoretical investigation of the distance dependence of capillary and van der Waals forces in scanning force microscopy.* Physical Review B, 2000. **62**(20): p. 13667-13673.

135. Zhuang, W., et al., *SFM Characterization of Poly(isocyanodipeptide) Single Polymer Chains in Controlled Environments: Effect of Tip Adhesion and Chain Swelling.* Macromolecules, 2004. **38**(2): p. 473-480.

136. Odian, G. and B.S. Bernstein, *Memory effects in irradiated polyethylene.* Journal of Applied Polymer Science, 1964. **8**(4): p. 1853-1867.

137. Lee, J.-U., D. Yoon, and H. Cheong, *Estimation of Young's Modulus of Graphene by Raman Spectroscopy.* Nano Letters, 2012. **12**(9): p. 4444-4448.

138. Kniprath, R., *Layer-by-layer self-assembled active electrodes for hybrid photovoltaic cells*, 2008, Mathematisch-Naturwissenschaftliche Fakultät I.

139. Park, B., et al., *High-performance organic thin-film transistors with polymer-blended small-molecular semiconductor films, fabricated using a pre-metered coating process.* Journal of Materials Chemistry, 2012. **22**(12): p. 5641-5646.

140. Davis, V.A., et al., *True solutions of single-walled carbon nanotubes for assembly into macroscopic materials.* Nature Nanotechnology, 2009. **4**(12): p. 830-834.

141. Wang, C., et al., *Wafer-Scale Fabrication of Separated Carbon Nanotube Thin-Film Transistors for Display Applications.* Nano Letters, 2009. **9**(12): p. 4285-4291.

142. Glatkowski, P.J., et al., *Modifikatoren der flüchtigen viskosität und stabilität für kohlenstoffnanoröhren-zusammensetzungen*, 2007, Google Patents.

143. Weidner, D.E., L.W. Schwartz, and R.R. Eley, *Role of Surface Tension Gradients in Correcting Coating Defects in Corners.* Journal of Colloid and Interface Science, 1996. **179**(1): p. 66-75.

144. Moon, I.K., et al., *2D Graphene Oxide Nanosheets as an Adhesive Over-Coating Layer for Flexible Transparent Conductive Electrodes.* Scientific Reports, 2013. **3**.

145. Huang, Z.D., et al., *Effects of reduction process and carbon nanotube content on the supercapacitive performance of flexible graphene oxide papers.* Carbon, 2012. **50**(11): p. 4239-4251.

146. Huang, Z.D., et al., *Self-assembled reduced graphene oxide/carbon nanotube thin films as electrodes for supercapacitors.* Journal of Materials Chemistry, 2012. **22**(8): p. 3591-3599.

147. Behabtu, N., et al., *Strong, Light, Multifunctional Fibers of Carbon Nanotubes with Ultrahigh Conductivity.* Science, 2013. **339**(6116): p. 182-186.

148. Pu, J.B., et al., *Controlled water adhesion and electrowetting of conducting hydrophobic graphene/carbon nanotubes composite films on engineering materials.* Journal of Materials Chemistry A, 2013. **1**(4): p. 1254-1260.

149. Ouyang, J., et al., *On the mechanism of conductivity enhancement in poly(3,4-ethylenedioxythiophene):poly(styrene sulfonate) film through solvent treatment.* Polymer, 2004. **45**(25): p. 8443-8450.

150. Al-Khatib, O., *Structure and optical properties of complex aggregate-structures of amphiphilic dye-systems*, 2012, Mathematisch-Naturwissenschaftliche Fakultät I.

151. Hu, L., D.S. Hecht, and G. Grüner, *Percolation in Transparent and Conducting Carbon Nanotube Networks.* Nano Letters, 2004. **4**(12): p. 2513-2517.

152. Baudot, C., et al., *Carbon nanotube-conductive polymer composites, methods of making and articles made therefrom*, 2012, Google Patents.

153. Ham, H.T., et al., *PEDOT-PSS/singlewall carbon nanotubes composites.* Polymer Engineering & Science, 2008. **48**(1): p. 1-10.

154. Hoback, J.T. and J.J. Reilly, *Conductive coatings for EMI shielding.* Journal of elastomers and plastics, 1988. **20**(1): p. 54-69.

155. Parikh, K., et al., *Flexible vapour sensors using single walled carbon nanotubes.* Sensors and Actuators B: Chemical, 2006. **113**(1): p. 55-63.

156. Daeha, J., et al., *High yield fabrication of chemically reduced graphene oxide field effect transistors by dielectrophoresis.* Nanotechnology, 2010. **21**(16): p. 165202.

157. Mustonen, T., et al., *Inkjet printing of transparent and conductive patterns of single-walled carbon nanotubes and PEDOT-PSS composites.* Physica Status Solidi B-Basic Solid State Physics, 2007. **244**(11): p. 4336-4340.

158. Najeeb, C., et al., *The effect of surface modifications of carbon nanotubes on the electrical properties of inkjet-printed SWNT/PEDOT-PSS composite line patterns.* Nanotechnology, 2010. **21**(38).

159. Balandin, A.A., *Thermal properties of graphene and nanostructured carbon materials.* Nat Mater, 2011. **10**(8): p. 569-581.

160. Qiu, L., et al., *Dispersing Carbon Nanotubes with Graphene Oxide in Water and Synergistic Effects between Graphene Derivatives.* Chemistry-A European Journal, 2010. **16**(35): p. 10653-10658.

161. Loudet, J.C., A.G. Yodh, and B. Pouligny, *Wetting and Contact Lines of Micrometer-Sized Ellipsoids.* Physical Review Letters, 2006. **97**(1): p. 018304.

162. Loudet, J.C., et al., *Capillary Interactions Between Anisotropic Colloidal Particles.* Physical Review Letters, 2005. **94**(1): p. 018301.

163. Bowden, N., et al., *Self-Assembly of Microscale Objects at a Liquid/Liquid Interface through Lateral Capillary Forces.* Langmuir, 2001. **17**(5): p. 1757-1765.

164. Brown, A.B.D., C.G. Smith, and A.R. Rennie, *Fabricating colloidal particles with photolithography and their interactions at an air-water interface.* Physical Review E, 2000. **62**(1): p. 951-960.

165. Lehle, H., E. Noruzifar, and M. Oettel, *Ellipsoidal particles at fluid interfaces.* European Physical Journal E, 2008. **26**(1-2): p. 151-160.

166. Lewandowski, E.P., et al., *Oriented assembly of anisotropic particles by capillary interactions.* Soft Matter, 2009. **5**(4): p. 886-890.

167. Danov, K.D. and P.A. Kralchevsky, *Capillary forces between particles at a liquid interface: General theoretical approach and interactions between capillary multipoles.* Advances in Colloid and Interface Science, 2010. **154**(1–2): p. 91-103.

168. Pengzhan, S., et al., *Suppression of the coffee-ring effect by self-assembling graphene oxide and monolayer titania.* Nanotechnology, 2013. **24**(7): p. 075601.

8. Acknowledgements

This thesis would not have been possible without the help of many people. In the following, I would like to thank several people for their kind and inspiring support.

Prof. Dr. Jürgen P. Rabe was the supervisor of this work and shared his rich knowledge in physics, chemistry and technology with me. Foremost, was always open-minded for new ideas. He provided the opportunity to make applied research and was a supervisor for a spin-off project “Druckbare Displays”, in which I was involved. I gained a lot of experiences in organizing of a spin-off company and in technological research which results in product developement. This wouldn’t be possible without the support of Prof. Dr. Jürgen. P. Rabe.

Dr. Nikolai Severin the most creative scientist I’ve ever met. He was my main cooperation partner. He opened my mind for several experimental details and acted as a critical reader of manuscripts and patents. He is a talented and vital partner for fruitful discussions and he has extensive scientific background accompanied with amazing technological intuition.

M. Fardin Gholami shared a chemical lab with me and acted as a partner for fruitful discussions and helped with the work on functional inks. His technological and chemical intuition inspired me greatly for the work with functional inks.

Evi Poblenz kept an outstanding chemistry lab running and perfectly in shape and was always helpful and forgiving.

Lothar Geyer patiently dealt with all computers.

Philipp Lange shared the office with me and helped doing Raman Spectroscopy. We had also a lot of discussions, which motivated me for further work.

Omar Al-Khatib shared the office and interests with me.

Egon Steeg has performed the TEM-imaging and helped me in TEM-data analysis and UV-Vis measurements.

Dr. Alexej Kalachev, Dr. Alexej Antipov and Dr. Yuri Fedutik (Plasmachem) shared their extensive background in chemistry with me. They opened my mind for details and shared their experience in organizing a spin-off company.

Patrick Barkowski (Fraunhofer IAP), Alexandra Mikityuk (T-Systems) and Marcin Ratajczak invited me to join the project “Druckbare Displays”. This project was supported by the Humboldt University and Fraunhofer IAP in Golm with the aim to create a Spin-off company.

Dr. Alexander Lange (Fraunhofer IAP) for being a guide of the labs in FIAP and fruitful technical discussions. He was a very loyal and nice person with excellent knowledge in solution processing of organic solar cells and transparent electrodes.

Bert Fischer (Fraunhofer IAP) for his technical background in the technology of OLEDs that gave me additional motivation to work on transparent electrodes.

Carl-Otto Danz (Fraunhofer IAP) the printing engineer. He introduced me into the printing technique Slot-Die Coating and gave input for the formulation of the inks.

Dr. Christine Boeffel (Fraunhofer IAP) for excellent scientific background in the state of the art of solution processing of OLEDs and solution processed materials. She gave a lot of input concerning the architecture of prototypical OLED-devices. She excellently coordinated the communication within the Fraunhofer IAP.

Dr. Armin Wedel (Fraunfoher IAP) for being a supervisor from Fraunhofer IAP in the spin-off project “Druckbare Displays” and gave me the opportunity to use the labs of Fraunhofer IAP.

Prof. Dr. Norbert Koch for being a supervisor in the spin-off project “Druckbare Displays”. He shared his rich knowledge in organic electronics which gave a lot of input for design of prototypical OLED-Display.

Dr. Georg Heimel opened my mind for the electrostatics at the interfaces and surfaces through fruitful discussions and his great scientific publications

Acknowledgements

Simone Zahn motivated me to work on new patents and coordinated common patents with the Fraunhofer IAP.

All the members of PMM provided nice working atmosphere and shared their reach knowledge with me.

9. Declaration (Eidesstattliche Erklärung)

I declare that this thesis is a presentation of my original research work. Wherever contributions of others are involved, every effort is made to indicate this clearly, with due reference to the literature, and acknowledgement of collaborative research and discussions.